Chapter 1

Introduction

The present work concerns direct numerical simulations of time-varying, three-dimensional, turbulent flow over a long circular cylinder. The statistics and structural characteristics of the flow field are examined for flows in which the free-stream is aligned, or nearly aligned, with the cylinder axis.

A prime example of this type of flow occurs on towed sonar arrays, which belong to the family of devices known as sound navigation and ranging systems, or sonar. Towed sonar arrays are commonly used for maritime surveillance and geophysical exploration. A typical towed sonar array is a long circular cylinder that is designed to be towed underwater behind a ship or submarine. The cylinder houses a linear array of acoustic pressure sensors whose outputs can be processed to estimate the location of remote acoustic sources. The cylinder is usually designed to have an overall density similar to that of the surrounding water, so that buoyancy forces on the cylinder are typically small in relation to the towing force. This ensures that the flow of water over the cylinder is aligned, or nearly aligned, with the cylinder axis. The length of a towed sonar array is typically thousands of times greater than the cylinder diameter, so that a thick, turbulent boundary layer evolves on the cylinder surface. In the design of a towed sonar array, it is important to consider the pressure fluctuations generated on the cylinder surface by the turbulent flow, to ensure that the sonar is capable of detecting weak acoustic signals. It is also important to endow the towed sonar array with sufficient tensile strength to withstand the skin friction exerted on the cylinder wall by the flow.

Axial and near-axial flow over cylinders can be considered special cases of flow over surfaces with convex, transverse curvature. Flows of this kind, such as those on aircraft fuselages and ship hulls, occur frequently in engineering practice. The properties of axial and near-axial flow over cylinders are therefore relevant to a wide variety of engineering applications.

1.1 Axisymmetric Flow Regimes

Compared with the boundary layers developed on flat plates or in cross-flow over cylinders, boundary layers developed in axial flow over cylinders have received relatively little attention in the research literature. A recent review of work concerning cylinders in axial flow is given by Piquet and Patel [1999].

The available data for cylinders are typically analysed using planar boundary layers as a point of reference. For boundary layers on plane surfaces, two length-scales are commonly used to describe the flow. The first of these is the boundary layer thickness δ, measured from the wall to the location where the mean-flow velocity is equal to 99% of the free-stream velocity. The second length-scale is the viscous length ν/u_τ, where ν is the kinematic viscosity of the fluid, $u_\tau = \sqrt{\tau_w/\rho}$ is the friction velocity, τ_w is the wall-shear-stress, and ρ is the fluid density. The ratio of these two length-scales gives the Reynolds number $\delta^+ = \delta/(\nu/u_\tau)$. In the absence of a streamwise pressure-gradient, any two planar boundary layers in incompressible Newtonian fluid have dynamic similitude if they share a given value of δ^+.

For the boundary layer on a cylinder in axial flow, the mean-flow and turbulence statistics are independent of azimuthal position around the cylinder, so that the boundary layer is described as axisymmetric. In such a flow, the cylinder radius a constitutes a third length-scale in addition to δ and ν/u_τ. These length-scales may be combined to give the three non-dimensional parameters δ/a, $a^+ = a/(\nu/u_\tau)$ and $\delta^+ = \delta/(\nu/u_\tau)$. Based on these parameters, research has led to the identification of three flow regimes. They are described by Piquet and Patel [1999] and, with limiting values as suggested by Afzal and Narasimha [1985], are as follows:

(i) Small δ/a ($\lesssim 1$), large a^+ ($\gtrsim 250$). The flow is little affected by transverse curvature, and is effectively planar flow.

(ii) Large δ/a ($\gg 1$), small a^+ ($\lesssim 250$). Strong effects of transverse curvature are observed throughout the boundary layer, on both the inner and outer regions of the layer. Some of the available data for this regime are for rather low values of δ^+ ($= a^+\delta/a$), where the effects of curvature are combined with the transitional effects associated with low Reynolds numbers.

(iii) Large δ/a ($\gg 1$), large a^+ ($\gtrsim 250$). This regime is most relevant to applications such as towed sonar arrays. In flows of this kind, the effects of transverse curvature are mainly evident in the outer flow, which is similar to an axisymmetric wake.

The rather limited data for the third regime have recently been extended by the measurements of wall-shear-stress and momentum thickness reported by Cipolla and Keith [2003a,b] ($a^+ \lesssim 300$, $\delta/a \lesssim 300$). The measurements by Berera [2004] ($a^+ \approx 170$, $\delta/a < 12$) supplement the available data near the boundary between the second and third flow regimes.

Researchers in fluid dynamics are frequently interested in the development of scaling relations that allow the results of flow measurements to be extrapolated to other situations. However, despite decades of research on the subject, there is still uncertainty over many of the fundamental scaling relations for turbulent, axisymmetric boundary layers. For example, competing scaling relations for the mean-velocity profile near the cylinder wall have been proposed by Rao [1967], Afzal and Narasimha [1976], Denli and Landweber [1979] and Lueptow, Leehey, and Stellinger [1985], amongst others.

The development of scaling relations for axisymmetric boundary layers is complicated by the lack of available data for independent, systematic variations of δ/a, a^+ and, at low Reynolds numbers, δ^+. A further obstacle to the establishment of scaling relations is the need to consider measurements from numerous experimental facilities, which has the potential to introduce a wide variety of systematic errors into the available data. Still more difficulties are caused by the need to obtain reliable values of the wall-shear-stress τ_w and the boundary layer thickness δ, which feature in many of the proposed scaling relations but are frequently difficult to measure accurately.

1.2 Numerical Simulation

The performance of modern supercomputers is such that investigation of turbulence is possible, at low to moderate Reynolds numbers, by a process known as direct numerical simulation or DNS. The process obtains the time-varying, three-dimensional flow fields by numerical solution of the Navier-Stokes equations with resolution sufficient to capture all essential scales of turbulence. DNS offers several advantages over experiments. Once a simulation procedure has been validated, the systematic variation of parameters is, in principle, straight-forward. Accurate values of the friction velocity and other scaling parameters may be computed directly from the simulated flow fields. The ability of DNS to resolve both temporal and spatial details of a flow is currently unmatched by experimental techniques. The main disadvantages of DNS are the technical challenges involved in the development of a high-performance simulation program and the vast computational resources required to execute the

program. Present-day computers limit DNS to Reynolds numbers that are somewhat less than those commonly found in engineering applications, although many experimental facilities have similar limitations.

The available DNS results for turbulent, axisymmetric boundary layers cover a quite limited range of parameters. Neves [1992], Neves, Moin, and Moser [1994] and Neves and Moin [1994] present results for $a^+ = 22$ and 43 with nominal values, respectively, of $\delta/a = 11$ and 5 and $\delta^+ = 239$ and 214. More recently, a brief summary of axisymmetric flow calculations is given by Tutty, Parsons, and Price [2004], however turbulence statistics and the ranges of a^+, δ/a and δ^+ are not included.

The present investigation extends the available DNS data for axisymmetric boundary layers to wider ranges of δ/a, a^+ and δ^+ than have previously been reported. The parameter ranges explored in the simulations are $\delta/a = 0.15$–27.5, $a^+ = 21$–1100 and $\delta^+ = 160$–800. These ranges correspond to only the first and second flow regimes listed previously in section 1.1. Nevertheless, the systematic variation of parameters allows trends and scaling relations to be identified that are likely to persist into the third flow regime.

The simulation procedure used for the present investigation is similar to the pseudo-spectral method employed by Neves [1992], but here rather different boundary conditions are imposed at the outer radial limit of the cylindrical computational domain. According to Neves [1992, p. 12], the outer boundary conditions used in his simulations restrict the radial motion of fluid and thereby exclude the possibility of large-scale cross-flow events of the kind observed experimentally by Lueptow and Haritonidis [1987]. Earlier measurements of velocity fluctuations reported by Luxton, Bull, and Rajagopalan [1984] suggest that the turbulence generation mechanisms in thick, axisymmetric boundary layers are enhanced, compared with planar flow, by the motion of large-scale turbulence structures across the cylinder. To ensure that the present simulations capture possible large-scale cross-flow motions, the outer boundary conditions are imposed on the vorticity field rather than the velocity field. While the vorticity field is confined to the computational domain, the velocity field converges smoothly to the free-stream velocity at large distances from the cylinder.

1.3 Near-Axial Flow

A few researchers have directed their interest to near-axial flow, where the cylinder axis is inclined slightly, generally by only a few degrees, relative to the free-stream

velocity vector. Following early work by Willmarth, Sharma, and Inglis [1977], turbulence on cylinders in near-axial flow appears to have attracted little attention until the more recent contributions of Bull and Dekkers [1993b,c], Bücker and Lueptow [1998], Heenan and Morrison [2002a,b], Snarski [2004] and Berera [2004]. Perhaps the most striking effect of yaw is the substantial asymmetry of the mean velocity field that occurs even at very small yaw angles. Significant deviations from axisymmetry are also observed in the statistics of velocity and wall-pressure fluctuations. Investigations by Bull and Dekkers [1993a] reveal that for a sufficiently large yaw angle or small Reynolds number, attached turbulent boundary layer flow gives way to a form of vortex-shedding.

As part of the present work, simulations of near-axial flow over cylinders are considered. No previous flow simulations of this kind appear to have been reported in the literature. The simulation procedure and boundary conditions used for near-axial flow are the same as those used for axial flow, which is simply the special case of a yaw angle equal to zero. Results are examined for turbulent flows with Reynolds numbers Re_a, based on cylinder radius and free-stream velocity, of 311 and 674 and yaw angles of 0.25 and 0.5 degrees. In addition, attention is given to vortex-shedding flow with $Re_a = 311$ and a yaw angle of 3 degrees. Although the range of flow parameters considered is rather limited, the present results are mainly intended to verify that the computational procedure is suitable for use in a more comprehensive investigation of near-axial flow.

1.4 Scope of the Present Work

The present thesis is mainly concerned with simulations of turbulent boundary layers on cylinders in axial flow. A detailed description of the simulation procedure is given in chapter 2. The computational issues associated with simulations of axisymmetric boundary layers are discussed in chapter 3. Velocity and pressure statistics arising from the simulations are presented in chapters 4 and 5. Particular attention is given to the assessment of similarity scaling relations for the mean velocity profile, velocity fluctuation statistics and temporal wall-pressure spectra. Structural features of axisymmetric turbulence are examined in chapter 6 by inspection of instantaneous flow fields, correlation functions and conditionally-averaged flow structures. Discussion of near-axial flow is deferred until chapter 7, where the effects of yaw on flow statistics and instantaneous structures are explored. Finally, the main findings of the investigation are discussed in chapter 8.

Chapter 2

Simulation Methodology

The primary aim of the present study is to obtain a valid quantitative description of the turbulent boundary layer generated by the flow of an incompressible fluid over a long circular cylinder whose axis is aligned with the free-stream. A secondary aim is to investigate the effects on the flow caused by small angles of yaw between the cylinder and the free-stream.

A pseudo-spectral method is adopted to produce a direct numerical simulation (DNS) of the flow in a cylindrical domain fixed to the cylinder. The flow fields are determined by solution of the Navier-Stokes equation expressed in the form of the vorticity transport equation. The usual condition of no-slip is imposed at the cylinder surface. At the outer radial limit of the domain, boundary conditions are imposed on the vorticity field so that there is potential flow outside the domain. The velocity field is required to be continuous throughout space and to converge to the free-stream at an infinite distance from the cylinder.

2.1 Computational Model

The geometry considered by the present study suggests the use of a cylindrical coordinate system fixed to the solid cylinder, where the radial, circumferential and axial directions are denoted respectively by r, θ and z.

To ensure that the flow can be given a numerical representation of a practical size, the flow is assumed to be periodic in the z-direction. An equivalent simplification has been used successfully in past simulations of planar boundary layers [see, for example, Kim, Moin, and Moser, 1987] and other turbulent flows. However, streamwise boundary layer growth and its effects on turbulence development cannot be captured with periodic boundary conditions, unless additional techniques are employed. For example, Spalart [1988] makes allowance for development of the mean

flow by use of a coordinate transformation to map diverging streamlines to a periodic domain. Lund, Wu, and Squires [1998] use a simulation procedure with turbulent inlet conditions generated by a modified form of Spalart's method and with convective outflow conditions imposed at the downstream boundary. The complexity of these methods is not considered to be justified for the current study, because the calculations are restricted to flows for which the mean-flow and turbulence statistics change slowly with increasing axial displacement. The assumption of periodicity does, however, imply that it is not possible to define an absolute axial position for the calculations, although an effective position can be determined by comparison of calculated results with experimental data.

While axial boundary layer development cannot be represented by the periodic boundary conditions, viscous and turbulence shear-stresses promote growth of the boundary layer as time advances. The temporal growth continues until it is eventually limited by the radial extent of the computational domain. After a sufficient time has elapsed, the turbulent flow reaches a statistically-steady state that is dependent on the shape of the boundary and the imposed boundary conditions. The accumulation of time-averaged flow statistics is most convenient once the statistically-steady state has been achieved. For free-stream flow that is aligned with the cylinder axis, the mean-flow and turbulence statistics are axisymmetric, so a cylindrical computational domain can be expected to produce meaningful data for the statistically-steady state. In contrast, slightly yawed free-stream flow has been observed experimentally to produce large deviations from axisymmetry in the boundary layer [see, for example, Willmarth et al., 1977, Bücker and Lueptow, 1998]. The optimal shape of the computational domain for yawed flow cannot be determined in advance, so collection of flow data at a statistically-steady state may not be practical. An alternative approach, described in detail in chapter 7, involves the collection of data from a yawed flow before it reaches statistical steadiness but after a suitable development time.

The computational model adopted for the current study is shown schematically in figure 2.1. The computational domain extends from the surface of the cylinder, whose radius is a, to a finite outer radius b. The flow is inherently periodic in the azimuthal direction, and periodic boundary conditions are imposed on a finite domain length L_z in the axial direction. Flow variables are represented by Fourier series in the azimuthal and axial directions and by Chebyshev series mapped non-uniformly

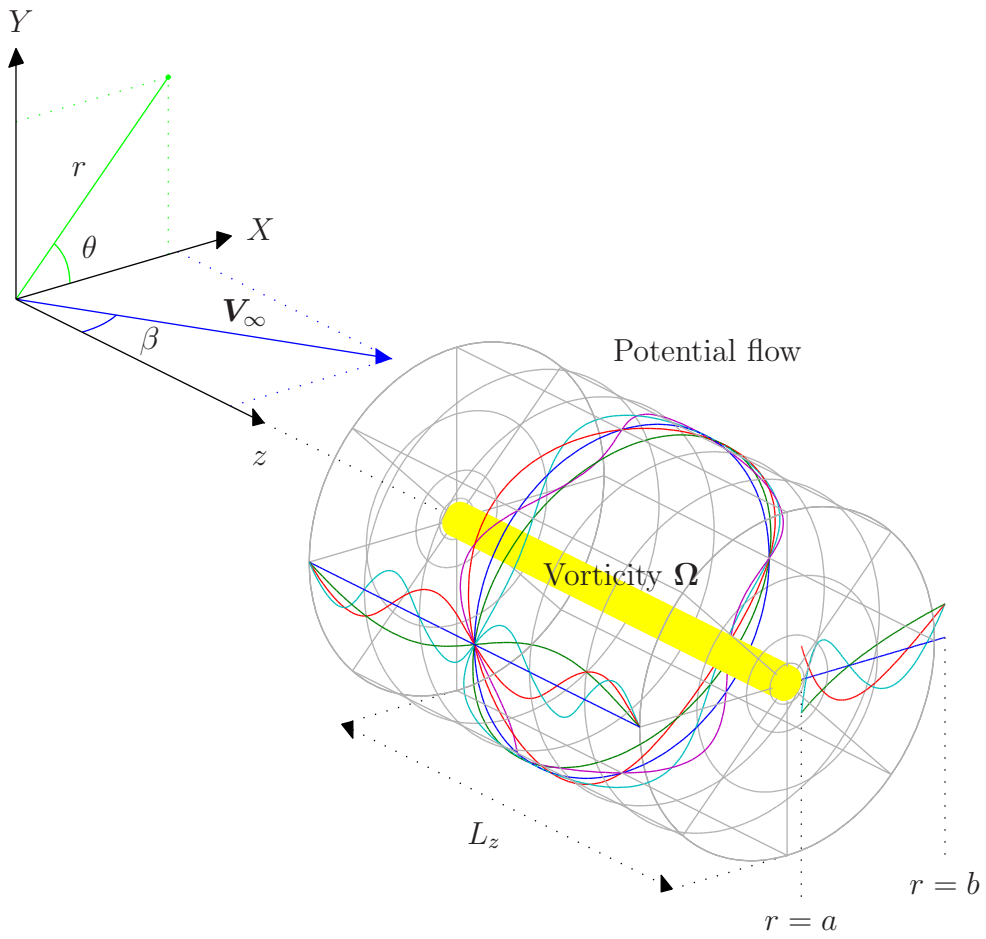

Figure 2.1: Schematic diagram of the computational model.

to the radial direction. At the cylinder surface, no-slip boundary conditions are imposed on the total (fluctuating) velocity field, so that

$$\boldsymbol{U}[a] = 0. \tag{2.1}$$

The computational model is thus similar in some respects to that used by Neves [1992]. The major difference is the choice of boundary conditions at radius b. Neves imposes conditions on velocity so that the shear-stress is zero at the outer edge of the domain:

$$U_r[b] = 0, \quad \frac{\partial}{\partial r}\left(\frac{U_\theta}{r}\right)[b] = 0, \quad \frac{\partial U_z}{\partial r}[b] = 0. \tag{2.2}$$

The boundary condition on the radial velocity component cannot be expected to provide an accurate representation of any large-scale ejection and cross-flow events, such as those observed experimentally by Luxton et al. [1984] and Lueptow and Haritonidis [1987]. In order to make possible the inclusion of such large-scale

motions, the velocity boundary conditions for the current study are imposed at infinity:

$$\boldsymbol{U}[\infty] = \boldsymbol{V}_\infty, \tag{2.3}$$

where $\boldsymbol{V}_\infty$ is the free-stream velocity. The boundary condition at radius b is imposed on vorticity such that

$$\Omega_r[b] = 0, \quad \Omega_\theta[b] \approx 0, \quad \Omega_z[b] \approx 0, \tag{2.4}$$

where the azimuthal and axial components are determined so that the magnitude of the resultant vorticity vector $\boldsymbol{\Omega}[b]$ is minimised. Vorticity becomes the primary simulation variable, and it is defined on the domain $a \leq r \leq b$, denoted by R_1. The velocity field is defined both within R_1 and in the external region $r > b$, denoted by R_2. The velocity is calculated from the vorticity field subject to the boundary conditions and the requirement that flow be continuous throughout space and across the interface at radius b. The velocity field in R_2, which is a potential flow by definition, can be expressed in analytical form with variable coefficients. The invariant parts of the analytical expression may be pre-calculated, and the coefficients are determined at each simulation time-step.

Corral and Jiménez [1995] describe a computational model, for planar flow, that is similar in concept to the model adopted in the present work. The two approaches differ mainly in the Chebyshev expansions used for the wall-normal direction. In the current model, the Chebyshev grid points accumulate near the inner and outer boundaries of the computational domain. Despite the use of a non-uniform mapping function, the grid resolution near the outer boundary is generally found to be excessive, so that computational effort and storage requirements are greater than is strictly necessary. Corral and Jiménez use Chebyshev series with either even or odd polynomials, so that grid resolution is at a minimum near the outer boundary. Such a grid is ideal for variables that decay rapidly away from the wall. However, for a turbulent flow in a statistically-steady state, turbulent eddies approach the outer boundary frequently, producing significant gradients of vorticity and velocity where the grid can resolve them least accurately. On the other hand, the domain truncation caused by the outer boundary is also a source of error, so greater grid accuracy near the boundary may not provide any real benefit. A comparison of the results obtained with the two models for the same flow could well be the basis for future calculations.

2.2 Governing Equations

2.2.1 Definition of Vorticity

The vorticity $\boldsymbol{\Omega}$ of a fluid is defined as

$$\boldsymbol{\Omega} = \nabla \times \boldsymbol{U}, \tag{2.5}$$

where $\boldsymbol{U}$ is the fluid velocity. The instantaneous angular velocity at a point in the fluid is equal to half the vorticity.

The cylindrical components of vorticity are [see, for example, Batchelor, 1967]

$$\begin{aligned} \Omega_r &= \frac{1}{r}\frac{\partial U_z}{\partial \theta} - \frac{\partial U_\theta}{\partial z} \\ \Omega_\theta &= \frac{\partial U_r}{\partial z} - \frac{\partial U_z}{\partial r} \\ \Omega_z &= \frac{1}{r}\left(\frac{\partial \left(rU_\theta\right)}{\partial r} - \frac{\partial U_r}{\partial \theta}\right). \end{aligned} \tag{2.6}$$

2.2.2 Divergence Specifications

Vorticity is defined to be the curl of velocity (equation 2.5). The divergence of a curl is zero by vector identity, therefore the vorticity field is divergence-free:

$$\nabla \cdot \boldsymbol{\Omega} = 0. \tag{2.7}$$

A notional line that is everywhere tangential to the local vorticity vector (a vortex line) cannot begin or end at a point in space but must instead form a closed loop. The no-slip condition implies that a vortex line cannot intersect a solid surface. For the current study, the fluid outside radius b is assumed to be irrotational, and since vortex lines cannot terminate at b, the radial component of vorticity must be zero at b.

The continuity equation for an incompressible fluid is

$$\nabla \cdot \boldsymbol{U} = 0, \tag{2.8}$$

which states that the velocity field is divergence-free. A notional line that is everywhere tangential to the local velocity vector (a streamline) cannot begin or end at a point in space by a similar consideration to that used for a vortex line. The streamline cannot intersect a solid surface for the simple reason that no flow through the surface is possible.

Equation 2.8 is expressed in cylindrical coordinates as

$$\frac{1}{r}\frac{\partial\big(rU_r\big)}{\partial r}+\frac{1}{r}\frac{\partial U_\theta}{\partial\theta}+\frac{\partial U_z}{\partial z}=0. \tag{2.9}$$

Equation 2.7 may be written in a similar form.

2.2.3 Vorticity Transport Equation

The incompressible Navier-Stokes equation is

$$\frac{\partial \boldsymbol{U}}{\partial t}+\boldsymbol{U}\cdot\nabla\boldsymbol{U}=-\frac{\nabla P}{\rho}+\nu\nabla^2\boldsymbol{U}, \tag{2.10}$$

where t is time, P is pressure, ρ is density, and ν is the kinematic viscosity. In cylindrical coordinates, the components of the equation are [Batchelor, 1967]

$$\frac{\partial U_r}{\partial t}+\left(U_r\frac{\partial U_r}{\partial r}+\frac{U_\theta}{r}\frac{\partial U_r}{\partial\theta}+U_z\frac{\partial U_r}{\partial z}-\frac{U_\theta^2}{r}\right)= -\frac{1}{\rho}\frac{\partial P}{\partial r}+\nu\left(\nabla^2U_r-\frac{U_r}{r^2}-\frac{2}{r^2}\frac{\partial U_\theta}{\partial\theta}\right), \tag{2.11a}$$

$$\frac{\partial U_\theta}{\partial t}+\left(U_r\frac{\partial U_\theta}{\partial r}+\frac{U_\theta}{r}\frac{\partial U_\theta}{\partial\theta}+U_z\frac{\partial U_\theta}{\partial z}+\frac{U_rU_\theta}{r}\right)= -\frac{1}{\rho r}\frac{\partial P}{\partial\theta}+\nu\left(\nabla^2U_\theta-\frac{U_\theta}{r^2}+\frac{2}{r^2}\frac{\partial U_r}{\partial\theta}\right), \tag{2.11b}$$

$$\frac{\partial U_z}{\partial t}+\left(U_r\frac{\partial U_z}{\partial r}+\frac{U_\theta}{r}\frac{\partial U_z}{\partial\theta}+U_z\frac{\partial U_z}{\partial z}\right)=-\frac{1}{\rho}\frac{\partial P}{\partial z}+\nu\nabla^2U_z, \tag{2.11c}$$

where ∇^2 is the Laplacian operator:

$$\nabla^2=\frac{\partial^2}{\partial r^2}+\frac{1}{r}\frac{\partial}{\partial r}+\frac{1}{r^2}\frac{\partial^2}{\partial\theta^2}+\frac{\partial^2}{\partial z^2}. \tag{2.12}$$

Equation 2.10 may be rewritten as

$$\frac{\partial \boldsymbol{U}}{\partial t}-\boldsymbol{U}\times\boldsymbol{\Omega}=-\frac{\nabla P_T}{\rho}+\nu\nabla^2\boldsymbol{U} \tag{2.13}$$

by use of the vector identity

$$\boldsymbol{U}\cdot\nabla\boldsymbol{U}=\frac{1}{2}\nabla\big(\|\boldsymbol{U}\|^2\big)-\boldsymbol{U}\times\boldsymbol{\Omega} \tag{2.14}$$

and the definition of total pressure

$$P_T = P + \frac{1}{2}\rho\|\boldsymbol{U}\|^2. \tag{2.15}$$

The curl of equation 2.13 is

$$\frac{\partial \boldsymbol{\Omega}}{\partial t} = \nabla \times \big(\boldsymbol{U} \times \boldsymbol{\Omega}\big) + \nu\nabla^2\boldsymbol{\Omega}, \tag{2.16}$$

because the curl of the conservative field ∇P_T is identically zero. Equation 2.16 is known as the vorticity transport equation.

This equation (cast in matrix form) is the equation to be solved for the time-varying, three-dimensional vorticity field $\boldsymbol{\Omega}$ by the simulation procedure.

Use of the vector identity

$$\nabla \times \big(\boldsymbol{U} \times \boldsymbol{\Omega}\big) = \boldsymbol{U}\big(\nabla \cdot \boldsymbol{\Omega}\big) - \boldsymbol{\Omega}\big(\nabla \cdot \boldsymbol{U}\big) - \big(\boldsymbol{U} \cdot \nabla\big)\boldsymbol{\Omega} + \big(\boldsymbol{\Omega} \cdot \nabla\big)\boldsymbol{U} \tag{2.17}$$

together with $\nabla \cdot \boldsymbol{\Omega} = 0$ (equation 2.7) and $\nabla \cdot \boldsymbol{U} = 0$ (equation 2.8) allows the vorticity transport equation to be written in the alternative form

$$\frac{\partial \boldsymbol{\Omega}}{\partial t} = -\big(\boldsymbol{U} \cdot \nabla\big)\boldsymbol{\Omega} + \big(\boldsymbol{\Omega} \cdot \nabla\big)\boldsymbol{U} + \nu\nabla^2\boldsymbol{\Omega}. \tag{2.18}$$

The equation is a statement that the time rate of change of vorticity includes contributions from convection, stretching and diffusion of vorticity.

The equations solved as part of the flow simulation are expressed in dimensionless form. For example, normalisation of equation 2.16 with respect to the free-stream velocity magnitude V_∞ and the cylinder radius a yields

$$\frac{\partial \breve{\boldsymbol{\Omega}}}{\partial \breve{t}} = \breve{\nabla} \times \big(\breve{\boldsymbol{U}} \times \breve{\boldsymbol{\Omega}}\big) + \frac{1}{Re_a}\breve{\nabla}^2\breve{\boldsymbol{\Omega}}, \tag{2.19}$$

where

$$\breve{\boldsymbol{\Omega}} = \frac{a\boldsymbol{\Omega}}{V_\infty},\ \breve{t} = \frac{tV_\infty}{a},\ \breve{\nabla} = a\nabla,\ \breve{\boldsymbol{U}} = \frac{\boldsymbol{U}}{V_\infty},\ \text{and}\ Re_a = \frac{aV_\infty}{\nu}. \tag{2.20}$$

However, for clarity, all variables and equations used in this thesis are dimensional unless explicitly defined otherwise.

2.2.4 Potential Flow

Outside the cylindrical computational domain, that is for radial positions $r > b$, the vorticity is required to be zero. The corresponding velocity field is therefore a potential flow.

A velocity field $\boldsymbol{V}$ is a potential flow if it satisfies the equation

$$\boldsymbol{V} = \nabla\Phi, \tag{2.21}$$

where the potential Φ is a solution of the Laplace equation

$$\nabla^2\Phi = 0. \tag{2.22}$$

In cylindrical coordinates, equation 2.21 becomes

$$V_r = \frac{\partial\Phi}{\partial r}, \quad V_\theta = \frac{1}{r}\frac{\partial\Phi}{\partial\theta}, \quad V_z = \frac{\partial\Phi}{\partial z}, \tag{2.23}$$

and equation 2.22 is expressed as

$$\frac{\partial^2\Phi}{\partial r^2} + \frac{1}{r}\frac{\partial\Phi}{\partial r} + \frac{1}{r^2}\frac{\partial^2\Phi}{\partial\theta^2} + \frac{\partial^2\Phi}{\partial z^2} = 0. \tag{2.24}$$

Details of the procedure used to solve the governing equations will now be considered.

2.3 Spectral Formulation

2.3.1 Fourier Series

The use of Fourier series to represent flow variables allows the three-dimensional governing equations to be reduced to a set of one-dimensional equations. These equations are solved for the Fourier coefficients of the flow variables. The bulk of the calculations involved in the solution procedure can be performed independently for each Fourier mode-number. Work may therefore be distributed between processors on a parallel computer without the need for excessive communication between processors.

The truncated Fourier series expansion for velocity is

$$\boldsymbol{U}[r,\theta,z,t] \approx \sum_{m=-N_\theta/2}^{N_\theta/2-1} \sum_{k=-N_z/2}^{N_z/2-1} \hat{\boldsymbol{U}}_{m,k}[r,t]\exp[ik_\theta r\theta]\exp[ik_z z], \tag{2.25}$$

where the complex Fourier coefficients $\hat{\boldsymbol{U}}$ are functions of radius and time. The constant i is the unit imaginary number $\sqrt{-1}$. The azimuthal wave-number is

$$k_\theta = m\frac{2\pi}{2\pi r} = \frac{m}{r}, \tag{2.26}$$

where m is the azimuthal Fourier mode-number. The axial wave-number over the assumed periodic length L_z is

$$k_z = k\frac{2\pi}{L_z}, \tag{2.27}$$

where k is the axial Fourier mode-number. Similar expansions are used for other flow fields such as the vorticity and pressure fields.

Consider an equispaced azimuthal-axial grid consisting of the points (θ_j, z_l) given by

$$\begin{aligned} \theta_j &= j2\pi/N_\theta, \quad j = -N_\theta/2, \ldots, N_\theta/2 - 1, \\ z_l &= lL_z/N_z, \quad l = -N_z/2, \ldots, N_z/2 - 1, \end{aligned} \tag{2.28}$$

where N_θ and N_z denote the total number of grid points in each direction. At these grid points, Fourier coefficients can be calculated so that equation 2.25 is satisfied exactly, because the equation takes the form of a two-dimensional inverse discrete Fourier transform:

$$\boldsymbol{U}[r, \theta_j, z_l, t] = \sum_{m=-N_\theta/2}^{N_\theta/2-1} \sum_{k=-N_z/2}^{N_z/2-1} \hat{\boldsymbol{U}}_{m,k}[r, t] \exp[i2\pi jm/N_\theta] \exp[i2\pi lk/N_z]. \tag{2.29}$$

The corresponding Fourier coefficients are given by

$$\hat{\boldsymbol{U}}_{m,k}[r, t] = \sum_{j=-N_\theta/2}^{N_\theta/2-1} \sum_{l=-N_z/2}^{N_z/2-1} \boldsymbol{U}[r, \theta_j, z_l, t] \exp[-i2\pi jm/N_\theta] \exp[-i2\pi lk/N_z]. \tag{2.30}$$

Efficient transformation between Fourier coefficients and values on the spatial grid of equation 2.28 is made possible by the family of algorithms known as the Fast Fourier Transform (FFT).

For a real-valued field F, it can be shown, using the symmetry properties of Fourier series, that

$$\hat{F}_{m,k} = \hat{F}^*_{-m,-k}, \tag{2.31}$$

where $*$ denotes the complex conjugate. It follows that

$$\hat{F}_{-m,k} = \hat{F}^*_{m,-k}. \tag{2.32}$$

The implication is that half of the Fourier modes are redundant, since it is a trivial task to obtain the modes corresponding to $k < 0$, for example, from the modes having $k \geq 0$. Computational effort and storage requirements may be reduced significantly by exploitation of this property.

2.3.2 Chebyshev Series

The Fourier coefficients of flow variables, as defined in the previous section, are continuous functions of radial position. A finite, but approximate, representation of the radial variation is provided by use of Chebyshev series.

The Chebyshev series expansion for velocity is

$$\hat{\boldsymbol{U}}_{m,k}\big[r[\xi],t\big] \approx \sum_{n=0}^{N-1} \tilde{\boldsymbol{U}}_{n,m,k}[t]T_n[\xi], \tag{2.33}$$

where $\tilde{\boldsymbol{U}}_{n,m,k}$ are the Chebyshev-Fourier coefficients, T_n is the Chebyshev polynomial of degree n, and N is the number of terms in the series. The Chebyshev polynomials are defined on the domain $-1 \leq \xi \leq 1$.

The transformation used to map the Chebyshev abscissa ξ to the radial interval $a \leq r \leq b$ is that used by Neves [1992]:

$$r[\xi] = \begin{cases} a + \frac{1}{2}(b-a)(\eta-1)(1+\xi)/(\eta-\xi) & 1 < \eta < \infty \\ \frac{1}{2}(b-a)\xi + \frac{1}{2}(b+a) & \eta = \infty. \end{cases} \tag{2.34}$$

The mapping is uniform when $\eta = \infty$. As the parameter η decreases from infinity towards unity, grid resolution near the cylinder surface increases at the expense of resolution near the outer computational boundary.

The Chebyshev polynomial of degree n is defined by the formula

$$T_n[\xi] = \cos[n\zeta], \tag{2.35}$$

where ξ and ζ are related by

$$\xi = \cos[\zeta], \quad \zeta \in [0, \pi]. \tag{2.36}$$

Despite the appearance of trigonometric expressions in the definition, T_n can be expressed as a regular polynomial in ξ by use of the recurrence relation

$$\begin{aligned} T_0[\xi] &= 1 \\ T_1[\xi] &= \xi \\ T_n[\xi] &= 2\xi T_{n-1}[\xi] - T_{n-2}[\xi], \quad n \geq 2. \end{aligned} \tag{2.37}$$

Chebyshev polynomials form a complete set, meaning that any smooth function can be represented to arbitrary accuracy by a Chebyshev series approximation simply by including a large enough number of terms. In addition, Chebyshev polynomials are orthogonal with respect to the weighting function $(1-\xi^2)^{-1/2}$:

$$\int_{-1}^{1} \frac{T_n[\xi]T_m[\xi]}{\sqrt{1-\xi^2}}\, d\xi = \int_0^{\pi} \cos[n\zeta]\cos[m\zeta]\, d\zeta = \begin{cases} 0 & n \neq m \\ \pi/2 & n = m \neq 0 \\ \pi & n = m = 0. \end{cases} \tag{2.38}$$

The Galerkin method, introduced later in section 2.7.1, depends on these properties.

Consider the approximation of a function f by the Chebyshev series

$$f[\xi] \approx \sum_{n=0}^{N-1} \tilde{f}_n T_n[\xi]. \tag{2.39}$$

The approximation can be made exact at the points

$$\xi_j = \cos\left[\frac{\pi\left(j+\frac{1}{2}\right)}{N}\right], \quad j = 0, 1, \ldots, (N-1), \tag{2.40}$$

which are the N zeros of T_N. The corresponding coefficients $\tilde{f}$, obtained with the aid of the discrete identity

$$\sum_{j=0}^{N-1} T_n[\xi_j]T_m[\xi_j] = \begin{cases} 0 & n \neq m \\ N/2 & n = m \neq 0 \\ N & n = m = 0, \end{cases} \tag{2.41}$$

are given by

$$\tilde{f}_n = \frac{c_n}{N} \sum_{j=0}^{N-1} f[\xi_j]T_n[\xi_j], \text{ where } c_n = \begin{cases} 1 & n = 0 \\ 2 & n > 0. \end{cases} \tag{2.42}$$

The coefficients $\tilde{f}$ can also be expressed in the form

$$\tilde{f}_n = \frac{c_n}{N} \sum_{j=0}^{N-1} f[\xi_j] \cos\left[\frac{n\pi\left(j+\frac{1}{2}\right)}{N}\right]. \tag{2.43}$$

If evaluation of f is restricted to the points ξ_j of equation 2.40, the Chebyshev series can be written in the form

$$f[\xi_j] = \sum_{n=0}^{N-1} \tilde{f}_n \cos\left[\frac{n\pi\left(j+\frac{1}{2}\right)}{N}\right]. \tag{2.44}$$

Both of the above formulae are variations of the discrete Fourier cosine transform, which may be calculated efficiently by use of the FFT.

The fact that it is possible to transform rapidly from functional values to Chebyshev coefficients and vice-versa at the points given by equation 2.40 suggests that these points should be used as grid points. Chebyshev series may be evaluated at other points either by direct evaluation, or somewhat more efficiently by use of the Clenshaw recurrence relation [see, for example, Press et al., 2001, §5.8]:

$$\begin{aligned} d_{N+1} &= d_N = 0, \\ d_n &= 2\xi d_{n+1} - d_{n+2} + \tilde{f}_n, \quad n = (N-1), \ldots, 2, 1, \\ f[\xi] &= \xi d_1 - d_2 + \tilde{f}_0. \end{aligned} \tag{2.45}$$

2.4 Time Advancement

2.4.1 Uncoupling the Viscous Operators

The evolution of the vorticity field $\boldsymbol{\Omega}$ is governed by the vorticity transport equation (2.16). The cylindrical components of the vorticity transport equation are

$$\frac{\partial \Omega_r}{\partial t} = X_r + \nu\left(\nabla^2\Omega_r - \frac{\Omega_r}{r^2} - \frac{2}{r^2}\frac{\partial \Omega_\theta}{\partial \theta}\right), \tag{2.46a}$$

$$\frac{\partial \Omega_\theta}{\partial t} = X_\theta + \nu\left(\nabla^2\Omega_\theta - \frac{\Omega_\theta}{r^2} + \frac{2}{r^2}\frac{\partial \Omega_r}{\partial \theta}\right), \tag{2.46b}$$

$$\frac{\partial \Omega_z}{\partial t} = X_z + \nu\nabla^2\Omega_z, \tag{2.46c}$$

where the Laplacian operator ∇^2 is defined by equation 2.12 and where the $X_{r,\theta,z}$ denote the cylindrical components of the non-linear term

$$\boldsymbol{X} = \nabla \times \left(\boldsymbol{U} \times \boldsymbol{\Omega}\right). \tag{2.47}$$

The time-stepping scheme described in the next section (2.4.2) requires that the three components of the viscous term can be treated separately. However, in cylindrical coordinates, the radial and azimuthal components of the viscous term are coupled (see the terms inside brackets in equations 2.46a and 2.46b). The scheme used to decouple the components of the viscous term is described here and is based on the scheme developed by Neves [1992, §2.2].

Fourier series similar to equation 2.25 may be written for the vorticity field and other flow fields. The use of Fourier series allows the vorticity transport equation to be expressed as a set of equations, where each equation involves the Fourier coefficients for a single mode-number as functions of radial position. The Fourier coefficients are marked here with a "hat" symbol (ˆ), for example $\hat{\mathbf{\Omega}}$.

The three components of vorticity are related by equation 2.7, which is expressed for cylindrical coordinates and Fourier coefficients as

$$\frac{1}{r}\frac{\partial\left(r\hat{\Omega}_r\right)}{\partial r} + \frac{im}{r}\hat{\Omega}_\theta + ik_z\hat{\Omega}_z = 0. \tag{2.48}$$

In principle, given any two of the vorticity components, the third can be calculated. Rather than choosing a single component as the dependent variable, which would be problematic when either $m = 0$ or $k_z = 0$, the azimuthal and axial components of vorticity are combined in the quantity

$$\hat{\Omega}_p = ik_z\hat{\Omega}_\theta - im\hat{\Omega}_z. \tag{2.49}$$

Given the two components $\hat{\Omega}_p$ and $\hat{\Omega}_r$, the azimuthal and axial vorticity components which satisfy equation 2.48 are

$$\begin{aligned}
\hat{\Omega}_\theta &= \frac{i}{m^2 + rk_z^2}\left[m\left(\hat{\Omega}_r + r\frac{\partial\hat{\Omega}_r}{\partial r}\right) - k_z r\hat{\Omega}_p\right], \\
\hat{\Omega}_z &= \frac{i}{m^2 + rk_z^2}\left[k_z\left(\hat{\Omega}_r + r\frac{\partial\hat{\Omega}_r}{\partial r}\right) + m\hat{\Omega}_p\right].
\end{aligned} \tag{2.50}$$

The uncoupling of the viscous terms is achieved by recasting the vorticity transport equation (2.46) in the form

$$\begin{aligned}
\frac{\partial\hat{\Omega}_r}{\partial t} &= \nu\hat{\nabla}^2\hat{\Omega}_r + \hat{H}_r \\
\frac{\partial\hat{\Omega}_p}{\partial t} &= \nu\hat{\nabla}^2\hat{\Omega}_p + \hat{H}_p,
\end{aligned} \tag{2.51}$$

where the Laplacian operator is defined by

$$\hat{\nabla}^2 = \frac{1}{r}\frac{\partial}{\partial r}\left(r\frac{\partial}{\partial r}\right) - \frac{m^2}{r^2} - k_z^2, \tag{2.52}$$

which excludes the coupled terms. The coupled viscous and inviscid terms are packaged in the expressions

$$\begin{aligned} \hat{H}_r &= \nu\left(-\frac{1}{r^2}\hat{\Omega}_r - \frac{i2m}{r^2}\hat{\Omega}_\theta\right) + \hat{X}_r \\ \hat{H}_p &= ik_z\nu\left(\frac{i2m}{r^2}\hat{\Omega}_r - \frac{1}{r^2}\hat{\Omega}_\theta\right) + ik_z\hat{X}_\theta - im\hat{X}_z. \end{aligned} \tag{2.53}$$

The procedure used to solve equation 2.51 is described in the following sections.

2.4.2 Time-Stepping Scheme

To determine the evolution of the flow field, the vorticity transport equation is integrated forward in time. Recall from section 2.1 that region R_1 ($a \leq r \leq b$) contains all of the vorticity in the flow. Consequently, the evolution of vorticity need not be considered on region R_2 ($r > b$).

High-order time accuracy can be achieved with minimal overhead by use of a multi-step method. Karniadakis, Israeli, and Orszag [1991] demonstrate that stiffly-stable schemes offer superior accuracy and stability compared with other multi-step methods when applied to the Navier-Stokes equations. The Laplacian term is treated implicitly (in terms of future values) for stability, while the coupled terms are treated explicitly (without future values) for computational efficiency. The stiffly-stable scheme for equation 2.51 is

$$\frac{1}{\Delta t}\left(\gamma_0\hat{\boldsymbol{\Omega}}_{l+1} - \sum_{j=0}^{J-1}\alpha_j\hat{\boldsymbol{\Omega}}_{l-j}\right) = \nu\hat{\nabla}^2\hat{\boldsymbol{\Omega}}_{l+1} + \sum_{j=0}^{J-1}\beta_j\hat{\boldsymbol{H}}_{l-j}, \tag{2.54}$$

where Δt is the time-step size and l is the current time-step number. J is the number of time-steps of flow history that are taken into account by the scheme; accuracy is generally improved by increasing J. The coefficients α_j, β_j and γ_0 are shown for schemes up to third order in table 2.1, which is reproduced from the cited work. The stiffly stable scheme may be rearranged into the form of a Helmholtz equation,

$$\Delta t\,\nu\hat{\nabla}^2\hat{\boldsymbol{\Omega}}_{l+1} - \gamma_0\hat{\boldsymbol{\Omega}}_{l+1} = -\sum_{j=0}^{J-1}\alpha_j\hat{\boldsymbol{\Omega}}_{l-j} - \Delta t\sum_{j=0}^{J-1}\beta_j\hat{\boldsymbol{H}}_{l-j}, \tag{2.55}$$

Coefficient	1st Order	2nd Order	3rd Order
γ_0	1	3/2	11/6
α_0	1	2	3
α_1	0	-1/2	-3/2
α_2	0	0	1/3
β_0	1	2	3
β_1	0	-1	-3
β_2	0	0	1

Table 2.1: Coefficients for stiffly-stable integration schemes up to third order.

which is solved for $\hat{\boldsymbol{\Omega}}$ at the next time-step $(l+1)$.

Validation tests of the present simulation procedure reported by Woods and Bull [2003] suggest that the time-stepping scheme is unstable for a stiffly-stable method of third order. However, the apparent instability was subsequently found to be the result of a programming error. In fact, a third-order scheme is used for the simulations reported in the present work.

To avoid the high computational cost of repeated inversion of the Galerkin matrices corresponding to equation 2.55 (see section 2.7.1), a fixed time-step size is used so that the LU factorisations may be pre-calculated and stored. The maximum time-step size is set so that the Courant-Friedrich-Lewy (CFL) number everywhere satisfies

$$\mathrm{CFL} = \pi \Delta t \left(\frac{|U_r|}{\Delta r} + \frac{|U_\theta|}{r \Delta \theta} + \frac{|U_z|}{\Delta z} \right) \leq 0.6, \tag{2.56}$$

where Δr, $\Delta \theta$ and Δz denote the local distance, in each direction, between the mesh points used for the spatial representation of vorticity (as discussed in section 2.3). The maximum CFL number of 0.6 is chosen for consistency with Neves [1992]. It has been found in the present study that a time-step size corresponding to a CFL number greater than unity generally leads to instability.

2.4.3 Evaluation of Non-Linear Term

The Fourier representation for flow variables allows the majority of calculations discussed above to be performed independently for each Fourier mode-number. The exception is calculation of the non-linear term, specifically the cross-product $\boldsymbol{\Pi} = \boldsymbol{U} \times \boldsymbol{\Omega}$, which is most efficiently performed in the space domain [see Canuto et al., 1988, §3.2]. The Fourier (or Chebyshev-Fourier) series for the velocity and

vorticity fields are evaluated on a spatial grid, where the cross-product is expressed in cylindrical components as

$$\begin{aligned} \Pi_r &= U_\theta \Omega_z - U_z \Omega_\theta \\ \Pi_\theta &= U_z \Omega_r - U_r \Omega_z \\ \Pi_z &= U_r \Omega_\theta - U_\theta \Omega_r. \end{aligned} \tag{2.57}$$

The grid values of $\mathbf{\Pi}$ are then transformed to Fourier (or Chebyshev-Fourier) coefficients for solution of equation 2.55.

The number of Chebyshev-Fourier coefficients required to represent $\mathbf{\Pi}$ without truncation is greater than the number used for either $\boldsymbol{U}$ or $\mathbf{\Omega}$. The above procedure may generate so-called aliasing errors in $\mathbf{\Pi}$, where the lower-order coefficients differ from their proper values. Aliasing errors may be reduced or eliminated from $\mathbf{\Pi}$ by use of a finer spatial mesh, and therefore additional Chebyshev-Fourier coefficients, for the calculation of $\mathbf{\Pi}$. Any additional higher-order coefficients used for de-aliasing of $\mathbf{\Pi}$ may be discarded, because they are of little use in further calculations.

The non-linear term of the vorticity transport equation is the curl of $\mathbf{\Pi}$, which is expressed in cylindrical components and Fourier coefficients as

$$\begin{aligned} \hat{X}_r &= \frac{im}{r}\hat{\Pi}_z - ik_z\hat{\Pi}_\theta \\ \hat{X}_\theta &= ik_z\hat{\Pi}_r - \frac{\partial \hat{\Pi}_z}{\partial r} \\ \hat{X}_z &= \frac{1}{r}\frac{\partial\left(r\hat{\Pi}_\theta\right)}{\partial r} - \frac{im}{r}\hat{\Pi}_r. \end{aligned} \tag{2.58}$$

2.4.4 Vorticity Boundary Conditions

To solve equation 2.55, specification of the vorticity boundary conditions is required. The radial component of vorticity is obtained with the fixed boundary conditions

$$\hat{\Omega}_r[a] = 0 \tag{2.59a}$$

$$\hat{\Omega}_r[b] = 0, \tag{2.59b}$$

which are necessary to allow the no-slip condition to be satisfied at the cylinder surface and the velocity field to be continuous across the outer boundary. The outer boundary conditions for the axial and azimuthal components of vorticity would ideally be set to zero to obtain a smooth transition to potential flow outside radius b. However, the two components are related by equation 2.50 and cannot be set

independently to zero. The minimum vector magnitude of each Fourier coefficient of vorticity at the outer boundary is given by the condition

$$\hat{\Omega}_p[b] = \frac{mk_z b(b-1)}{m^2 + k_z^2 b^2} \frac{\partial \hat{\Omega}_r}{\partial r}[b]. \tag{2.59c}$$

The remaining boundary condition is

$$\hat{\Omega}_p[a] = c_{m,k}[t], \tag{2.59d}$$

where c is specified such that the fluid at the cylinder surface satisfies the no-slip condition. The value of c is determined at each time-step and for each Fourier mode-number by use of the procedure described below.

As a pre-processing step, equation 2.55 is solved with the right-hand-side set to zero. The boundary conditions imposed are those given above with $\hat{\Omega}_p[a]$ set to the inhomogeneous value $c = 1$. The vorticity solution is denoted by $\hat{\boldsymbol{\Omega}}_i$ and the corresponding velocity field is denoted by $\hat{\boldsymbol{U}}_i$. The pre-processed solutions are retained for use during the simulation. Only the non-zero components need to be stored, and additional memory may be saved by use of the fact that the solutions for Fourier modes (m, k) and $(-m, k)$ are identical once sign changes are taken into consideration.

For each step of the flow simulation, equation 2.55 is solved with the right-hand-side calculated from the simulated flow fields. The boundary conditions imposed are those given by equations 2.59a–d with $\hat{\Omega}_p[a]$ set to the homogeneous value $c = 0$. The vorticity solution and the corresponding velocity field are denoted respectively by $\hat{\boldsymbol{\Omega}}_h$ and $\hat{\boldsymbol{U}}_h$.

The linearity of equation 2.55 allows the solution at each time-step, with the boundary conditions given by equations 2.59a–d, to be expressed as

$$\hat{\boldsymbol{\Omega}} = \hat{\boldsymbol{\Omega}}_h + c_{m,k}\, \hat{\boldsymbol{\Omega}}_i \tag{2.60a}$$

and the corresponding velocity as

$$\hat{\boldsymbol{U}} = \hat{\boldsymbol{U}}_h + c_{m,k}\, \hat{\boldsymbol{U}}_i. \tag{2.60b}$$

The coefficient c is determined so that the no-slip condition is satisfied for a single velocity component, $\hat{U}_\theta$ for example. The boundary condition for $\hat{\Omega}_r$ implies that $\hat{U}_z$ also vanishes at the cylinder surface. Special treatment is required in the case of

mode $m = 0$, for which $\hat{\Omega}_r$ is independent of $\hat{U}_z$. Rearrangement of equation 2.60b gives the required values of c:

$$c_{m,k} = \begin{cases} -\hat{U}_{h\theta}[a]/\hat{U}_{i\theta}[a] & m \neq 0 \\ -\hat{U}_{hz}[a]/\hat{U}_{iz}[a] & m = 0. \end{cases} \tag{2.61}$$

2.4.5 Azimuthal-Axial-Mean Vorticity

For the mean flow, which corresponds to Fourier mode-numbers $m = 0$ and $k = 0$, the formulation of the vorticity transport equation given by equation 2.51 is not useful because equation 2.50 is singular. However, the components of the viscous term are not coupled, and solution of the vorticity transport equation is straightforward.

The divergence-free vorticity field satisfies equation 2.7, which reduces to

$$\frac{1}{r}\frac{\partial\left(r\hat{\Omega}_{r_{0,0}}\right)}{\partial r} = 0. \tag{2.62}$$

The only solution that satisfies homogeneous boundary conditions is

$$\hat{\Omega}_{r_{0,0}} = 0. \tag{2.63}$$

The remaining vorticity components are advanced in time by solution of equation 2.55 with

$$\begin{aligned} \hat{H}_{\theta_{0,0}} &= \nu\left(-\frac{1}{r^2}\hat{\Omega}_\theta\right) + \hat{X}_\theta \\ \hat{H}_{z_{0,0}} &= \hat{X}_z. \end{aligned} \tag{2.64}$$

The boundary conditions have the form

$$\frac{\partial\hat{\Omega}_{z_{0,0}}}{\partial r}[a] = 0 \tag{2.65a}$$

$$\hat{\Omega}_{z_{0,0}}[b] = 0 \tag{2.65b}$$

$$\hat{\Omega}_{\theta_{0,0}}[a] = c_{0,0}[t] \tag{2.65c}$$

$$\hat{\Omega}_{\theta_{0,0}}[b] = 0. \tag{2.65d}$$

The inner boundary condition for $\hat{\Omega}_z$ (equation 2.65a) is derived from the mean azimuthal component of the Navier-Stokes equation (2.10) at the cylinder surface:

$$\begin{aligned} \nu\nabla^2\hat{U}_{\theta_{0,0}}[a] &= 0 \\ \therefore \frac{\partial}{\partial r}\left(\frac{1}{r}\frac{\partial(r\hat{U}_{\theta_{0,0}})}{\partial r}\right)[a] &= 0 \\ \therefore \frac{\partial}{\partial r}\left(\hat{\Omega}_{z_{0,0}}\right)[a] &= 0. \end{aligned} \tag{2.66}$$

The value of the inner boundary condition for $\hat{\Omega}_\theta$ (equation 2.65c) that eliminates the slip velocity is

$$c_{0,0} = -\frac{\hat{U}_{hz}[a]}{\hat{U}_{iz}[a]}, \tag{2.67}$$

where $\hat{\boldsymbol{U}}_h$ and $\hat{\boldsymbol{U}}_i$ are determined in a similar fashion to that described in section 2.4.4.

2.5 Velocity Calculation

2.5.1 Background

While vorticity is the primary variable of the flow simulation, the velocity field is used at each time-step to compute the non-linear term and the boundary condition for vorticity. The present section concerns the method used to calculate the velocity field from a given vorticity field.

In principle, the velocity field may be calculated from the vorticity by means of the Biot-Savart law [see, for example, Cottet and Koumoutsakos, 2000]. The integrand is singular, and the singularity requires careful treatment if accurate results are to be expected from a numerical integration scheme. Possible approaches include the desingularisation method of Hou, Lowengrub, and Shelley [1993] or the use of an adaptive quadrature rule. Direct evaluation of the integral requires $O(N^2)$ operations for N grid points. In comparison, the method presented here, which involves numerical solution of differential equations for each Fourier mode, requires $O(N)$ operations. Hierarchical methods allow the Biot-Savart integral to be computed in $O(N)$ operations [see, for example, Anderson, 1992], but accuracy is compromised for increased speed.

The Biot-Savart integral gives the velocity field for flow without solid boundaries. Surface boundary conditions are imposed by use of vortex sheets. The present method takes a comparable two-stage approach, in which an initial velocity field

is computed with arbitrary boundary conditions which are corrected in a separate operation.

2.5.2 Velocity Decomposition

As explained in section 2.1, the present flow is considered to consist of two regions. Region R_1 contains a vorticity field $\boldsymbol{\Omega}$, while region R_2 is free of vorticity.

For the calculation of velocity, the velocity fields in the two flow regions are further decomposed into the forms

$$\begin{aligned} \boldsymbol{U}_1 &= \boldsymbol{V}_\infty + \boldsymbol{V}_1 + \boldsymbol{W} \\ \boldsymbol{U}_2 &= \boldsymbol{V}_\infty + \boldsymbol{V}_2, \end{aligned} \tag{2.68}$$

where $\boldsymbol{V}_1$ and $\boldsymbol{V}_2$ are potential flows and $\boldsymbol{V}_\infty$ is the free-stream velocity. The field $\boldsymbol{W}$ satisfies the relationship

$$\nabla \times \boldsymbol{W} = \boldsymbol{\Omega} \tag{2.69}$$

and arbitrary boundary conditions.

Once a solution for $\boldsymbol{W}$ is known, the potential flows $\boldsymbol{V}$ may be determined so that the total velocity fields $\boldsymbol{U}$ satisfy physically meaningful boundary conditions. The procedures used to determine the fields $\boldsymbol{W}$ and $\boldsymbol{V}$ are developed in the following discussion.

2.5.3 Boundary Conditions

The conditions that should be satisfied at the boundaries of each flow region by the total velocity $\boldsymbol{U}$ defined by equation 2.68 are described below.

1. The radial component of velocity at radius a is zero, since flow through the cylinder surface is not possible:

$$V_{\infty r} + V_{1r}[a] + W_r[a] = 0. \tag{2.70a}$$

2. All components of velocity should be continuous across the boundary at radius b between regions R_1 and R_2:

$$V_{1r}[b] + W_r[b] = V_{2r}[b], \tag{2.70b}$$

$$V_{1\theta}[b] + W_\theta[b] = V_{2\theta}[b], \tag{2.70c}$$

$$V_{1z}[b] + W_z[b] = V_{2z}[b]. \tag{2.70d}$$

3. All components of velocity should approach the free-stream velocity $\boldsymbol{V}_\infty$ as distance from the cylinder approaches infinity:

$$\lim_{r\to\infty} V_{2r}[r] = 0, \tag{2.70e}$$

$$\lim_{r\to\infty} V_{2\theta}[r] = 0, \tag{2.70f}$$

$$\lim_{r\to\infty} V_{2z}[r] = 0. \tag{2.70g}$$

The no-slip condition, which requires that the tangential velocity components are zero at the cylinder surface, has been omitted from the above list. In general, it is not possible to set both the normal and tangential components of surface velocity to zero unless appropriate constraints are imposed on the vorticity field. In the present work, the boundary conditions for vorticity are chosen at each time-step so that the no-slip condition is satisfied explicitly. It is therefore unnecessary to impose the no-slip condition as part of the velocity calculation except where the listed conditions are insufficient to produce a unique solution.

2.5.4 Free-Stream Velocity

The free-stream velocity vector $\boldsymbol{V}_\infty$ is oriented as shown in figure 2.1. The Cartesian components of the free-stream velocity are

$$\begin{aligned} V_{\infty X} &= V_\infty \sin\beta \\ V_{\infty Y} &= 0 \\ V_{\infty z} &= V_\infty \cos\beta, \end{aligned} \tag{2.71}$$

where V_∞ is the free-stream velocity magnitude and β is the yaw angle between the free-stream velocity vector and the cylinder axis. The corresponding cylindrical components are

$$\begin{aligned} V_{\infty r} = V_{\infty X}\cos\theta &= \frac{V_{\infty X}}{2}(\exp[i\theta] + \exp[-i\theta]) \\ V_{\infty\theta} = -V_{\infty X}\sin\theta &= \frac{iV_{\infty X}}{2}(\exp[i\theta] - \exp[-i\theta]) \\ V_{\infty z} &= V_\infty \cos\beta. \end{aligned} \tag{2.72}$$

Therefore, all Fourier coefficients of the free-stream velocity are zero except for

$$\begin{aligned} \hat{V}_{\infty r_{\pm 1,0}} &= \frac{V_\infty \sin\beta}{2} \\ \hat{V}_{\infty \theta_{\pm 1,0}} &= \pm\frac{iV_\infty \sin\beta}{2} \\ \hat{V}_{\infty z_{0,0}} &= V_\infty \cos\beta. \end{aligned} \tag{2.73}$$

2.5.5 Vortical Velocity

The definition of vorticity (equation 2.5) and the continuity equation (2.8) may be manipulated to obtain a velocity field $\boldsymbol{W}$ that corresponds to a given vorticity field $\boldsymbol{\Omega}$. The boundary conditions imposed on $\boldsymbol{W}$ are arbitrary and may be specified in any convenient manner.

The Fourier coefficients of the vorticity components in cylindrical coordinates, derived from equations 2.6 and 2.25, are given by

$$\hat{\Omega}_r = \frac{im}{r}\hat{W}_z - ik_z\hat{W}_\theta \tag{2.74a}$$

$$\hat{\Omega}_\theta = ik_z\hat{W}_r - \frac{\partial \hat{W}_z}{\partial r} \tag{2.74b}$$

$$\hat{\Omega}_z = \frac{1}{r}\frac{\partial\left(r\hat{W}_\theta\right)}{\partial r} - \frac{im}{r}\hat{W}_r. \tag{2.74c}$$

The continuity equation in cylindrical components (equation 2.9) is expressed for each Fourier mode-number by

$$\frac{1}{r}\frac{\partial\left(r\hat{W}_r\right)}{\partial r} + \frac{im}{r}\hat{W}_\theta + ik_z\hat{W}_z = 0. \tag{2.75}$$

The details of the solution procedure for $\hat{\boldsymbol{W}}$ depend on the Fourier mode-number, as described below.

Azimuthal-Axial-Mean Mode

For Fourier mode-numbers $m = 0$ and $k = 0$, equation 2.74b may be rearranged and integrated with respect to r to produce

$$\hat{W}_{z_{0,0}} = -\int \hat{\Omega}_\theta \, dr. \tag{2.76}$$

The integration constant is arbitrary, and has been set to zero for convenience. Similarly, equations 2.74c and 2.75 may be manipulated to isolate

$$\hat{W}_{\theta_{0,0}} = \frac{1}{r}\int r\hat{\Omega}_z \, dr \tag{2.77}$$

and

$$\hat{W}_{r_{0,0}} = 0. \tag{2.78}$$

Azimuthal-Mean Modes

In the case of Fourier mode-numbers $m = 0$ and $k \neq 0$, differentiation of equation 2.75 with respect to r and substitution from equation 2.74b gives

$$r^2\frac{\partial^2\hat{W}_{r_{0,k}}}{\partial r^2} + r\frac{\partial\hat{W}_{r_{0,k}}}{\partial r} - \hat{W}_{r_{0,k}} - k_z^2 r^2\hat{W}_{r_{0,k}} = ik_z r^2\hat{\Omega}_\theta, \tag{2.79}$$

which may be solved for $\hat{W}_r$. The remaining components of velocity follow by rearrangement of equations 2.74a and 2.75:

$$\hat{W}_{\theta_{0,k}} = \frac{i}{k_z}\hat{\Omega}_r \tag{2.80}$$

$$\hat{W}_{z_{0,k}} = \frac{i}{k_z}\left(\frac{\hat{W}_r}{r} + \frac{\partial\hat{W}_r}{\partial r}\right). \tag{2.81}$$

Higher-Order Azimuthal Modes

When the azimuthal Fourier mode-number m is non-zero, equations 2.74a and 2.74c may be rearranged to isolate $\hat{W}_r$ and $\hat{W}_z$:

$$\hat{W}_r = \frac{i}{m}\left(r\hat{\Omega}_z - \hat{W}_\theta - r\frac{\partial\hat{W}_\theta}{\partial r}\right) \tag{2.82}$$

$$\hat{W}_z = \frac{1}{m}\left(k_z r\hat{W}_\theta - ir\hat{\Omega}_r\right). \tag{2.83}$$

Substitution into equation 2.75 yields

$$r^2\frac{\partial^2\hat{W}_\theta}{\partial r^2} + 3r\frac{\partial\hat{W}_\theta}{\partial r} + (1-m^2)\hat{W}_\theta - k_z^2 r^2\hat{W}_\theta = 2r\hat{\Omega}_z + r^2\frac{\partial\hat{\Omega}_z}{\partial r} - ik_z r^2\hat{\Omega}_r. \tag{2.84}$$

The solution $\hat{W}_\theta$ may be used to calculate the remaining components via equations 2.82 and 2.83.

2.5.6 General Solutions for Potential Flow

For a velocity field $\boldsymbol{V}$ expressed as a Fourier series in cylindrical coordinates (equation 2.25), the relation $\boldsymbol{V} = \nabla\Phi$ in the form of equation 2.23 implies that the velocity potential Φ has the form

$$\Phi[r,\theta,z,t] = \sum_m \sum_{k_z} \hat{\Phi}[r,t] \exp[im\theta] \exp[ik_z z] + c_\theta \theta + c_z z + c_0, \tag{2.85}$$

where the terms $c_\theta\theta$ and $c_z z$ allow for mean flow in the azimuthal and axial directions. The corresponding Fourier coefficients of the velocity components are

$$\begin{aligned} \hat{V}_r &= \frac{\partial\hat{\Phi}}{\partial r} \\ \hat{V}_\theta &= \begin{cases} c_\theta/r & m = k = 0 \\ im\hat{\Phi}/r & \text{otherwise} \end{cases} \\ \hat{V}_z &= \begin{cases} c_z & m = k = 0 \\ ik_z\hat{\Phi} & \text{otherwise.} \end{cases} \end{aligned} \tag{2.86}$$

The velocity potential satisfies the Laplace equation in cylindrical coordinates (equation 2.24), which is expressed for each Fourier mode-number as

$$\frac{\partial^2\hat{\Phi}}{\partial r^2} + \frac{1}{r}\frac{\partial\hat{\Phi}}{\partial r} - \frac{m^2}{r^2}\hat{\Phi} - k_z^2\hat{\Phi} = 0. \tag{2.87}$$

General solutions for the Fourier coefficients $\hat{\Phi}$ are derived here. These forms are used later, in section 2.5.7, to derive expressions for the potential flow fields $\boldsymbol{V}_1$ and $\boldsymbol{V}_2$ of equation 2.68 such that the overall velocity field is consistent with the vorticity field and the boundary conditions of section 2.5.3.

Azimuthal-Axial-Mean Mode

For Fourier mode-numbers $m = 0$ and $k = 0$, the Laplace equation (2.87) reduces to

$$\frac{\partial}{\partial r}\left(r\frac{\partial\hat{\Phi}_{0,0}}{\partial r}\right) = 0. \tag{2.88}$$

Double integration with respect to r gives

$$\hat{\Phi}_{0,0} = c_r \ln r. \tag{2.89}$$

Axial-Mean Modes

For Fourier mode-numbers $m \neq 0$ and $k = 0$, the Laplace equation (2.87) becomes an Euler-Cauchy equation,

$$r^2 \frac{\partial^2}{\partial r^2} \hat{\Phi}_{m,0} + r \frac{\partial}{\partial r} \hat{\Phi}_{m,0} - m^2 \hat{\Phi}_{m,0} = 0. \tag{2.90}$$

The corresponding solution has the form

$$\hat{\Phi}_{m,0} = c_1 r^{-|m|} + c_2 r^{|m|}. \tag{2.91}$$

Higher-Order Axial Modes

For the remaining Fourier mode-numbers with $k \neq 0$, introduction of the variable $s = |k_z| r$ into the Laplace equation (2.87) yields the modified Bessel equation,

$$s^2 \frac{\partial^2}{\partial s^2} \hat{\Phi} + s \frac{\partial}{\partial s} \hat{\Phi} - \left(m^2 + s^2\right) \hat{\Phi} = 0. \tag{2.92}$$

Two linearly independent solutions are $I_{|m|}[s]$ and $K_{|m|}[s]$, which are respectively the modified Bessel functions of the first and second kind, both of integer order $|m|$. The general solution is given by the linear combination

$$\hat{\Phi} = c_1 K_{|m|}\big[|k_z| r\big] + c_2 I_{|m|}\big[|k_z| r\big]. \tag{2.93}$$

The behaviour of the modified Bessel functions is illustrated in figure 2.2.

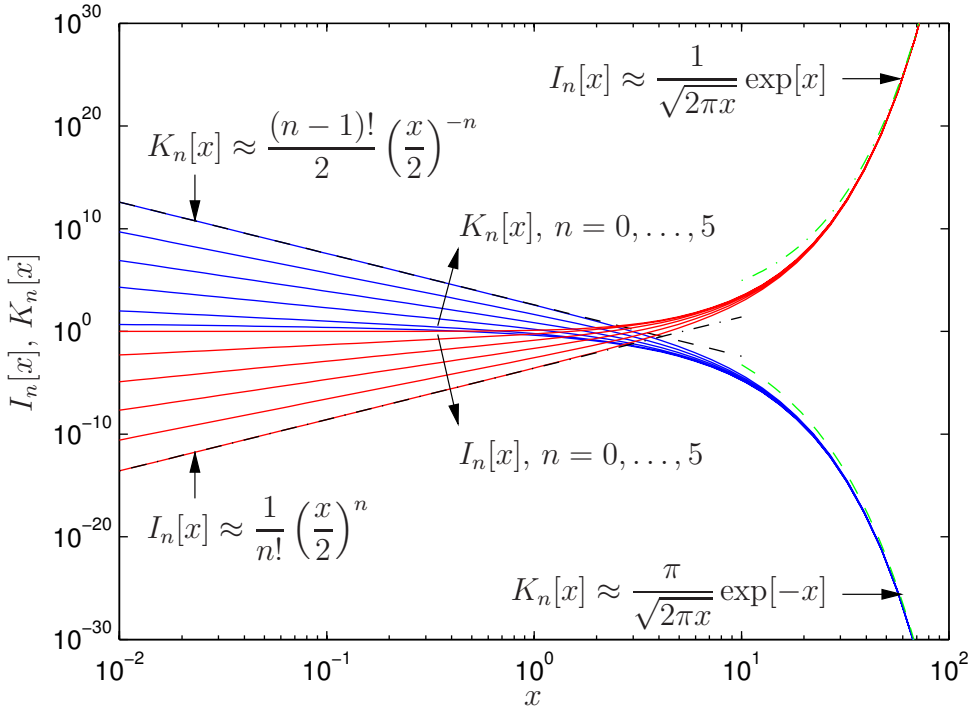

Figure 2.2: Modified Bessel functions $I_n[x]$ (red curves) and $K_n[x]$ (blue curves) for positive x and integer n. Black curves show asymptotic behaviour for small x and $n = 5$. Green curves show asymptotic behaviour for large x.

2.5.7 Particular Solutions for Potential Flow

The general solutions derived in the previous section involve unknown coefficients. The values of the coefficients are determined here by imposition of the boundary conditions described in section 2.5.3.

Azimuthal-Axial-Mean Mode

For Fourier mode-numbers $m = 0$ and $k = 0$, the potential flow velocity given by equations 2.86 and 2.89 has the form

$$\begin{aligned} \hat{V}_{1r_{0,0}} &= c_{1r}/r, \quad \hat{V}_{1\theta_{0,0}} = c_{1\theta}/r, \quad \hat{V}_{1z_{0,0}} = c_{1z}, \\ \hat{V}_{2r_{0,0}} &= c_{2r}/r, \quad \hat{V}_{2\theta_{0,0}} = c_{2\theta}/r, \quad \hat{V}_{2z_{0,0}} = c_{2z}, \end{aligned} \tag{2.94}$$

where the coefficients c may take different values on the two regions R_1 and R_2.

Equations 2.73, 2.78 and 2.94 reduce the boundary conditions of equation 2.70 to the following:

$$c_{1r} = 0, \tag{2.95a}$$
$$c_{1r} = c_{2r}, \tag{2.95b}$$
$$c_{1\theta}/b + \hat{W}_{\theta_{0,0}}[b] = c_{2\theta}/b, \tag{2.95c}$$
$$c_{1z} + \hat{W}_{z_{0,0}}[b] = c_{2z}, \tag{2.95d}$$
$$\lim_{r\to\infty} c_{2r}/r = 0, \tag{2.95e}$$
$$\lim_{r\to\infty} c_{2\theta}/r = 0, \tag{2.95f}$$
$$c_{2z} = 0. \tag{2.95g}$$

The left-hand-sides of equations 2.95e–f approach zero, therefore these equations are redundant. The remaining five equations involve six unknowns, so the no-slip condition is invoked to give the additional equation

$$c_{1\theta}/a + \hat{W}_{\theta_{0,0}}[a] = 0. \tag{2.95h}$$

The coefficients obtained by solution of the above equations correspond to the potential flow velocity given by

$$\begin{aligned}
\hat{V}_{1r_{0,0}} &= 0, \\
\hat{V}_{1\theta_{0,0}} &= -a\hat{W}_{\theta}[a]/r, \\
\hat{V}_{1z_{0,0}} &= -\hat{W}_{z}[b], \\
\hat{V}_{2r_{0,0}} &= 0, \\
\hat{V}_{2\theta_{0,0}} &= b\hat{W}_{\theta}[b]/r - a\hat{W}_{\theta}[a]/r, \\
\hat{V}_{2z_{0,0}} &= 0.
\end{aligned} \tag{2.96}$$

Axial-Mean Modes

The unknown velocity potentials on regions R_1 and R_2 for Fourier mode-numbers $m \neq 0$ and $k = 0$ are

$$\begin{aligned}
\hat{\Phi}_{1_{m,0}} &= c_{11}r^{-|m|} + c_{12}r^{|m|} \\
\hat{\Phi}_{2_{m,0}} &= c_{21}r^{-|m|} + c_{22}r^{|m|}.
\end{aligned} \tag{2.97}$$

Equations 2.73, 2.83, 2.86 and 2.97 allow the boundary conditions of equation 2.70 to be expressed as

$$-|m|a^{-|m|-1}c_{11} + |m|a^{|m|-1}c_{12} + \hat{W}_{r_{m,0}}[a] = -\hat{V}_{\infty r_{m,0}}, \tag{2.98a}$$

$$-|m|b^{-|m|-1}c_{11} + |m|b^{|m|-1}c_{12} + \hat{W}_{r_{m,0}}[b] = -|m|b^{-|m|-1}c_{21} + |m|b^{|m|-1}c_{22}, \tag{2.98b}$$

$$imb^{-|m|-1}c_{11} + imb^{|m|-1}c_{12} + \hat{W}_{\theta_{m,0}}[b] = imb^{-|m|-1}c_{21} + imb^{|m|-1}c_{22}, \tag{2.98c}$$

$$\hat{\Omega}_{r_{m,0}}[b] = 0, \tag{2.98d}$$

$$\lim_{r\to\infty} r^{|m|-1}c_{22} = 0, \tag{2.98e}$$

$$\lim_{r\to\infty} r^{|m|-1}c_{22} = 0, \tag{2.98f}$$

$$0 = 0. \tag{2.98g}$$

The left-hand-side of equation 2.98d reduces to zero, due to the boundary conditions imposed on the vorticity field (equation 2.59b). Equations 2.98e–f can only be satisfied by $c_{22} = 0$. Equations 2.98d–g are therefore redundant, so the boundary conditions reduce to three equations in the three unknown coefficients c_{11}, c_{12} and c_{21}. The velocity potentials corresponding to the solutions for these coefficients are

$$\begin{aligned}\hat{\Phi}_{1_{m,0}}[r] = \left(\hat{W}_r[a] + \hat{V}_{\infty r}\right)\left\{\frac{a}{|m|}\left(\frac{a}{r}\right)^{|m|}\right\} + \\ \hat{W}_r[b]\left\{-\frac{b}{2|m|}\left(\left(\frac{a^2}{br}\right)^{|m|} + \left(\frac{r}{b}\right)^{|m|}\right)\right\} + \\ \left(i\,\mathrm{sgn}[m]\,\hat{W}_\theta[b]\right)\left\{\frac{b}{2|m|}\left(\left(\frac{a^2}{br}\right)^{|m|} + \left(\frac{r}{b}\right)^{|m|}\right)\right\}\end{aligned} \tag{2.99}$$

and

$$\begin{aligned}\hat{\Phi}_{2_{m,0}}[r] = \left(\hat{W}_r[a] + \hat{V}_{\infty r}\right)\left\{\frac{a}{|m|}\left(\frac{a}{r}\right)^{|m|}\right\} + \\ \hat{W}_r[b]\left\{-\frac{b}{2|m|}\left(\left(\frac{a^2}{br}\right)^{|m|} + \left(\frac{b}{r}\right)^{|m|}\right)\right\} + \\ \left(i\,\mathrm{sgn}[m]\,\hat{W}_\theta[b]\right)\left\{\frac{b}{2|m|}\left(\left(\frac{a^2}{br}\right)^{|m|} - \left(\frac{b}{r}\right)^{|m|}\right)\right\},\end{aligned} \tag{2.100}$$

where

$$\mathrm{sgn}[x] = \begin{cases} 1 & x > 0 \\ 0 & x = 0 \\ -1 & x < 0. \end{cases} \tag{2.101}$$

The velocity field $\hat{\boldsymbol{V}}_1$ is evaluated, by use of $\boldsymbol{V} = \nabla\Phi$ in the form of equation 2.86, throughout region R_1 at each time-step of the simulation. To minimise the computational workload, the quantities inside braces in the expression for $\hat{\Phi}_1$ may be evaluated during a pre-processing step at radial grid points and the corresponding Chebyshev coefficients retained for use during the simulation. A considerable saving in the storage requirements can be made by noting that all of the pre-processed data are real and independent of the signs of mode-numbers m and k.

Higher-Order Axial Modes

The unknown velocity potentials on regions R_1 and R_2 for Fourier mode-numbers $k \neq 0$ are

$$\begin{aligned} \hat{\Phi}_{1_{m,k}} &= c_{11}\mathcal{K}[r] + c_{12}\mathcal{I}[r] \\ \hat{\Phi}_{2_{m,k}} &= c_{21}\mathcal{K}[r] + c_{22}\mathcal{I}[r], \end{aligned} \tag{2.102}$$

where use has been made of the abbreviations

$$\begin{aligned} \mathcal{K}[r] &= K_{|m|}\big[|k_z|r\big] \\ \mathcal{I}[r] &= I_{|m|}\big[|k_z|r\big]. \end{aligned} \tag{2.103}$$

The derivatives of the modified Bessel functions may be expressed as

$$\begin{aligned} \mathcal{K}'[r] &= \frac{\partial\mathcal{K}[r]}{\partial r} = |k_z|K'_{|m|}\big[|k_z|r\big] \\ \mathcal{I}'[r] &= \frac{\partial\mathcal{I}[r]}{\partial r} = |k_z|I'_{|m|}\big[|k_z|r\big], \end{aligned} \tag{2.104}$$

where

$$\begin{aligned} K'_n[x] &= \frac{dK_n[x]}{dx} = -\frac{1}{2}\left(K_{n-1}[x] + K_{n+1}[x]\right) \\ I'_n[x] &= \frac{dI_n[x]}{dx} = \frac{1}{2}\left(I_{n-1}[x] + I_{n+1}[x]\right). \end{aligned} \tag{2.105}$$

Equations 2.73, 2.86, 2.102 and 2.104 allow the boundary conditions of equation 2.70 to be expressed as

$$\mathcal{K}'[a]c_{11} + \mathcal{I}'[a]c_{12} + \hat{W}_r[a] = 0, \tag{2.106a}$$

$$\mathcal{K}'[b]c_{11} + \mathcal{I}'[b]c_{12} + \hat{W}_r[b] = \mathcal{K}'[b]c_{21} + \mathcal{I}'[b]c_{22}, \tag{2.106b}$$

$$(im/b)\left(\mathcal{K}[b]c_{11} + \mathcal{I}[b]c_{12}\right) + \hat{W}_\theta[b] = (im/b)\left(\mathcal{K}[b]c_{21} + \mathcal{I}[b]c_{22}\right), \tag{2.106c}$$

$$ik_z\left(\mathcal{K}[b]c_{11} + \mathcal{I}[b]c_{12}\right) + \hat{W}_z[b] = ik_z\left(\mathcal{K}[b]c_{21} + \mathcal{I}[b]c_{22}\right), \tag{2.106d}$$

$$\lim_{r\to\infty} \mathcal{I}'[r]c_{22} = 0, \tag{2.106e}$$

$$\lim_{r\to\infty} \mathcal{I}[r]c_{22} = 0, \tag{2.106f}$$

$$\lim_{r\to\infty} \mathcal{I}[r]c_{22} = 0. \tag{2.106g}$$

If the azimuthal Fourier mode-number is $m = 0$, equation 2.106c reduces to $0 = 0$, because $\hat{W}_\theta[b] = (i/k_z)\hat{\Omega}_r[b]$ (equation 2.80) and the vorticity boundary conditions ensure that $\hat{\Omega}_r[b] = 0$ (equation 2.59b). For mode-numbers $m \neq 0$, multiplication of equation 2.106c by $k_z b/m$ yields equation 2.106d, because equations 2.83 and 2.59b give $(k_z b/m)\hat{W}_\theta[b] = \hat{W}_z[b]$. Equation 2.106c is therefore redundant. Equations 2.106e–g can only be satisfied by $c_{22} = 0$, so these equations are also redundant. The boundary conditions therefore reduce to the three equations 2.106a, 2.106b and 2.106d, which may be solved for the three coefficients c_{11}, c_{12} and c_{21}. These coefficients correspond to the velocity potentials given by

$$\hat{\Phi}_1[r] = \hat{W}_r[a]\left\{-\frac{\mathcal{K}[r]}{\mathcal{K}'[a]}\right\} + \left(b\,\hat{W}_r[b]\right)\left\{\frac{\mathcal{K}[b]}{\mathcal{K}'[a]}\mathcal{I}'[a]\mathcal{K}[r] - \mathcal{K}[b]\mathcal{I}[r]\right\} + \left(i\,\mathrm{sgn}[k_z]\,b\,\hat{W}_z[b]\right)\left\{\frac{\mathcal{K}'[b]}{\mathcal{K}'[a]}\frac{\mathcal{I}'[a]\mathcal{K}[r]}{|k_z|} - \frac{\mathcal{K}'[b]\mathcal{I}[r]}{|k_z|}\right\} \tag{2.107}$$

and

$$\hat{\Phi}_2[r] = \hat{W}_r[a]\left\{-\frac{\mathcal{K}[r]}{\mathcal{K}'[a]}\right\} + \left(b\,\hat{W}_r[b]\right)\left\{\frac{\mathcal{K}[b]}{\mathcal{K}'[a]}\mathcal{I}'[a]\mathcal{K}[r] - \mathcal{I}[b]\mathcal{K}[r]\right\} + \left(i\,\mathrm{sgn}[k_z]\,b\,\hat{W}_z[b]\right)\left\{\frac{\mathcal{K}'[b]}{\mathcal{K}'[a]}\frac{\mathcal{I}'[a]\mathcal{K}[r]}{|k_z|} - \frac{\mathcal{I}'[b]\mathcal{K}[r]}{|k_z|}\right\}. \tag{2.108}$$

The potential flow velocity is evaluated throughout region R_1 at each time-step of the simulation. The computational considerations discussed earlier in relation to the axial-mean modes also apply here.

A summary of the velocity calculation procedure is given, as part of an overall summary of the simulation procedure, at the end of the chapter.

2.6 Pressure Calculation

Because the vorticity transport equation involves only the velocity and vorticity fields, the pressure field is not an essential part of the solution. The pressure field may be calculated for arbitrary time-steps of the solution, either as part of the solution procedure or as a post-processing operation.

The Poisson equation for pressure is obtained from the divergence of the Navier-Stokes equation (2.10),

$$\frac{\nabla^2 P}{\rho} = -\nabla \cdot (\boldsymbol{U} \cdot \nabla \boldsymbol{U}) \,. \tag{2.109}$$

The Fourier series expansion for pressure, in a form analogous to equation 2.25, allows the above equation to be expressed separately for each Fourier mode-number. In cylindrical coordinates, the equation for the Fourier coefficients of pressure, denoted by $\hat{P}$, is

$$\frac{1}{\rho}\frac{\partial^2 \hat{P}}{\partial r^2} + \frac{1}{\rho r}\frac{\partial \hat{P}}{\partial r} - \frac{1}{\rho r^2}\left(m^2 + k_z^2 r^2\right)\hat{P} = \hat{\lambda}_p[r], \tag{2.110}$$

where $\hat{\lambda}_p$ denotes the Fourier coefficients of the pressure-source corresponding to the right-hand-side of equation 2.109. The pressure-source is expressed in cylindrical coordinates as

$$\begin{aligned}\lambda_p = -2\frac{\partial U_z}{\partial r}\frac{\partial U_r}{\partial z} - \left(\frac{\partial U_r}{\partial r}\right)^2 - \frac{2}{r}\frac{\partial U_\theta}{\partial r}\left(\frac{\partial U_r}{\partial \theta} - U_\theta\right) \\ - \frac{1}{r^2}\left(\frac{\partial U_\theta}{\partial \theta} + U_r\right)^2 - \frac{2}{r}\frac{\partial U_z}{\partial \theta}\frac{\partial U_\theta}{\partial z} - \left(\frac{\partial U_z}{\partial z}\right)^2 .\end{aligned} \tag{2.111}$$

Because of the non-linear relationship between λ_p and the velocity field, it is difficult to calculate the Fourier coefficients of λ_p directly from the Fourier coefficients of velocity. It is more efficient to evaluate λ_p on a spatial grid and then to determine the Fourier coefficients $\hat{\lambda}_p$ by use of the discrete Fourier transform (equation 2.30 with velocity replaced by pressure).

Boundary conditions for pressure are derived from the radial component of the Navier-Stokes equation. At the cylinder surface, all components of velocity vanish and the Navier-Stokes equation becomes

$$\frac{\nabla P}{\rho} = \nu \nabla^2 \boldsymbol{U}. \tag{2.112}$$

Further manipulation yields the inner boundary condition for pressure,

$$\frac{1}{\rho}\frac{\partial \hat{P}}{\partial r}[a] = \nu \frac{\partial^2 \hat{U}_r}{\partial r^2}[a]. \tag{2.113}$$

Outside the outer boundary of the computational domain, the assumption of potential flow reduces the Navier-Stokes equation in the form of equation 2.13 to

$$\frac{\nabla P_T}{\rho} = -\frac{\partial \boldsymbol{U}}{\partial t}. \tag{2.114}$$

The total pressure at the outer boundary is given by integration of the gradient from infinity:

$$\frac{1}{\rho}\left(\hat{P}_T[b] - \hat{P}_T[\infty]\right) = -\int_{\infty}^{b} \frac{\partial \hat{U}_r}{\partial t}[r]\, dr = -\frac{\partial \hat{\Phi}_2}{\partial t}[b]. \tag{2.115}$$

The corresponding boundary condition for static pressure is

$$\frac{1}{\rho}\left(\hat{P}[b] - \hat{P}[\infty]\right) = -\frac{\partial \hat{\Phi}_2}{\partial t}[b] - \frac{1}{\rho}\hat{Q}[b] + \frac{1}{\rho}\hat{Q}[\infty]. \tag{2.116}$$

The $\hat{Q}$ are Fourier coefficients of the dynamic pressure

$$Q = \frac{1}{2}\rho \|\boldsymbol{U}\|^2, \tag{2.117}$$

which is most efficiently evaluated in the space domain. The velocity potential $\hat{\Phi}_2$ is calculated via the formulae presented in section 2.5.7. The time derivative may be approximated by use of finite differences across simulation time-steps.

2.7 Numerical Methods

2.7.1 Galerkin Method

The Galerkin method [see, for example, Boyd, 1989] allows linear differential equations to be expressed in matrix form when the solution is expanded as a finite series. For the current study, the Galerkin method is used to solve the algebraic, differential

and integral equations that arise when the flow equations are expressed in terms of Chebyshev-Fourier modes.

Consider the one-dimensional equation

$$\mathcal{L}_1 u[x] = \mathcal{L}_2 f[x], \quad x \in [x_a, x_b], \tag{2.118}$$

where $\mathcal{L}_1$ and $\mathcal{L}_2$ are linear differential operators, x_a and x_b are the endpoints of the problem domain, and f is a known function. A series approximation for the unknown u is

$$u[x] \approx \sum_{n=0}^{N-1} \tilde{u}_n \psi_n[x], \tag{2.119}$$

where the ψ_n are differentiable basis functions defined over the interval $[x_a, x_b]$. A similar expansion can be written for function f.

The residual for equation 2.118 is defined as

$$e[x] = \mathcal{L}_1 u - \mathcal{L}_2 f, \tag{2.120}$$

which expresses the amount by which an approximate solution u is in error. The Galerkin method attempts to minimise the residual by enforcing the conditions

$$((e, \psi_m)) = 0, \quad m = 0, 1, \ldots, N-1. \tag{2.121}$$

The form on the left-hand-side, known as the inner product, is defined as

$$((u, v)) = \int_{x_a}^{x_b} uvw \, dx, \tag{2.122}$$

where w is a suitable weight function. If the basis functions are taken from a complete set, the residual may be expressed as

$$e[x] = \sum_{n=0}^{\infty} \tilde{e}_n \psi_n[x]. \tag{2.123}$$

Substitution of the above expression into equation 2.121 yields

$$\sum_{n=0}^{\infty} \tilde{e}_n \left((\psi_n, \psi_m)\right) = 0, \quad m = 0, 1, \ldots, N-1. \tag{2.124}$$

If the basis functions are orthogonal, then, by definition,

$$((\psi_n, \psi_m)) = \begin{cases} 0 & n \neq m \\ c_n & n = m, \end{cases} \tag{2.125}$$

where the value c_n may depend on n. Consequently equation 2.124 reduces to

$$\tilde{e}_n = 0, \quad n = 0, 1, \ldots, N-1. \tag{2.126}$$

Thus the Galerkin method — with basis functions that form a complete, orthogonal set — forces the first N series coefficients of the residual to zero. The larger the value N, the greater the accuracy of the solution.

The Galerkin method applied to equation 2.118 yields

$$((\mathcal{L}_1 u, \psi_m)) = ((\mathcal{L}_2 f, \psi_m)), \quad m = 0, 1, \ldots, N-1. \tag{2.127}$$

Substitution of the series for u and f gives the system of equations

$$\sum_{n=0}^{N-1} \tilde{u}_n ((\mathcal{L}_1 \psi_n, \psi_m)) = \sum_{n=0}^{N-1} \tilde{f}_n ((\mathcal{L}_2 \psi_n, \psi_m)), \quad m = 0, 1, \ldots, N-1. \tag{2.128}$$

The inner product terms may be precomputed and stored in matrix form, so that the series coefficients $\tilde{u}_n$ may be determined by use of standard matrix solution techniques.

When Chebyshev polynomials are chosen as the basis functions, the elements of the Galerkin matrices have the form

$$((\mathcal{L} T_n, T_m)) = \int_0^\pi \left\{ \mathcal{L} \cos[n\zeta] \right\} \cos[m\zeta] \, d\zeta, \tag{2.129}$$

where the inner product is given by equation 2.38. The integral may be calculated numerically with great precision by a variety of methods including rapid, frequency domain techniques that employ the FFT.

For the equations considered in the current study, all non-zero elements of the Galerkin matrices lie within a band centred on the main diagonal. The width of the band is independent of the number of polynomials N used for the Chebyshev series. This structure is significant because there exist algorithms for the efficient solution and storage of banded systems of equations. For example, solution of a system by back-substitution of LU factors (considered in the following section) requires $O(N^2)$

operations and memory locations for full matrices compared with $O(N)$ for banded matrices.

2.7.2 Faddeev-Faddeeva Factorisation

Boundary conditions may be imposed on a Galerkin matrix system by replacement of equations. For the example of equation 2.128, a single boundary condition replaces the equation for $m = (N-1)$, a second boundary condition replaces the equation for $m = (N-2)$, and so on. When the initial Galerkin matrix is banded, the imposition of boundary conditions disrupts the banded structure. However, factorisation and solution of the partially banded matrix system may be performed efficiently by use of the boundary bordering method of Faddeev and Faddeeva [1963]. A variation of the method that is compatible with standard LAPACK routines [see Anderson et al., 1999] is described below.

A partially banded matrix equation $\mathrm{Ax} = \mathrm{b}$, which is to be solved for x, may be partitioned as

$$\begin{pmatrix} \mathrm{A}_{11} & \mathrm{A}_{12} \\ \mathrm{A}_{21} & \mathrm{A}_{22} \end{pmatrix} \begin{pmatrix} \mathrm{x}_1 \\ \mathrm{x}_2 \end{pmatrix} = \begin{pmatrix} \mathrm{b}_1 \\ \mathrm{b}_2 \end{pmatrix}, \tag{2.130}$$

where submatrix A_{11} is banded and the other submatrices are full. If the overall dimension of the A matrix is $N \times N$ and the number of non-banded rows is s, the submatrix sizes are

$$\begin{aligned} \mathrm{A}_{11} &\equiv (N-s) \times (N-s) \\ \mathrm{A}_{12} &\equiv (N-s) \times s \\ \mathrm{A}_{21} &\equiv s \times (N-s) \\ \mathrm{A}_{22} &\equiv s \times s \\ \mathrm{x}_1, \mathrm{b}_1 &\equiv (N-s) \times 1 \\ \mathrm{x}_2, \mathrm{b}_2 &\equiv s \times 1. \end{aligned} \tag{2.131}$$

The Faddeev-Faddeeva factorisation expresses the LU decomposition of the partitioned matrix A as

$$\begin{pmatrix} \mathrm{L}_{11} & 0 \\ \mathrm{L}_{21} & \mathrm{L}_{22} \end{pmatrix} \begin{pmatrix} \mathrm{U}_{11} & \mathrm{U}_{12} \\ 0 & \mathrm{U}_{22} \end{pmatrix} = \begin{pmatrix} \mathrm{A}_{11} & \mathrm{A}_{12} \\ \mathrm{A}_{21} & \mathrm{A}_{22} \end{pmatrix}, \tag{2.132}$$

where like-numbered submatrices have the same size. Although it is possible to determine all of the submatrices in the factorisation, the following sequence of

operations is sufficient as a preparatory step in the solution of a matrix equation in the form of equation 2.130:

$$\mathrm{L}_{11}\mathrm{U}_{11} = \mathrm{A}_{11} \tag{2.133a}$$

$$\mathrm{L}_{11}\mathrm{U}_{11}\mathrm{B}_{12} = \mathrm{A}_{12} \tag{2.133b}$$

$$\mathrm{L}_{22}\mathrm{U}_{22} = \mathrm{A}_{22} - \mathrm{A}_{21}\mathrm{B}_{12}. \tag{2.133c}$$

The submatrices L_{11} and U_{11} are determined by LU decomposition of A_{11}. The auxiliary matrix $\mathrm{B}_{12} = \mathrm{U}_{11}^{-1}\mathrm{U}_{12}$ is obtained by solution of equation 2.133b. Lastly, submatrices L_{22} and U_{22} are given by LU decomposition of the right-hand-side of equation 2.133c.

Since A_{11} is banded, the factors L_{11} and U_{11} are also banded, and the LU decomposition can be computed using $O(N)$ operations and memory locations. The remaining submatrices are full, but the overall workload and storage required to compute them is also $O(N)$, assuming that s is independent of N. For the purposes of the current study, the LU factors can be determined as a pre-processing step, since the corresponding matrix equations do not change during the simulation.

The accuracy of the factorisation is compromised if the whole A matrix or the submatrices A_{11} or A_{22} are ill-conditioned. Row and column reordering of A can improve the condition number of a submatrix without affecting the condition number of the whole matrix. The condition number of the whole matrix can be improved by scaling rows or columns.

The solutions x_1 and x_2 of matrix equation 2.130 are obtained via the following operations:

$$\mathrm{L}_{11}\mathrm{U}_{11}\mathrm{y} = \mathrm{b}_1 \tag{2.134a}$$

$$\mathrm{L}_{22}\mathrm{U}_{22}\mathrm{x}_2 = \mathrm{b}_2 - \mathrm{A}_{21}\mathrm{y} \tag{2.134b}$$

$$\mathrm{x}_1 = \mathrm{y} - \mathrm{B}_{12}\mathrm{x}_2. \tag{2.134c}$$

The intermediate solution y of equation 2.134a is used to determine the right-hand-side of equation 2.134b, which is solved for x_2. Then x_1 follows from equation 2.134c.

The equations which involve the banded submatrices L_{11} and U_{11} can be solved by back-substitution using $O(N)$ operations and memory locations. The remaining submatrices of the LU factors are full, but the workload and storage required to perform the associated arithmetic is also $O(N)$.

2.7.3 Bessel Function Calculation

The rapid variation of the modified Bessel functions $K_n[x]$ and $I_n[x]$ with x and n is shown in figure 2.2. The limits of floating point arithmetic can be exceeded for moderate values of x and n. Direct evaluation of the modified Bessel functions in the velocity potentials given by equations 2.107 and 2.108 is found to be impractical when either the number of Fourier modes, or the size of the simulation domain relative to the cylinder radius, becomes large. An alternative is to evaluate terms of the form

$$r_{m,n}[x_m, x_n] = \frac{K_m[x_m]}{K_n[x_n]} \tag{2.135}$$

and

$$p_{m,n}[x_m, x_n] = I_m[x_m]K_n[x_n], \tag{2.136}$$

where the difference between orders m and n is small.

Calculation of the ratio term $r_{m,n}$ starts with evaluation of sequences $\rho_j[x_m]$ and $\rho_j[x_n]$, where

$$\rho_j[x] = \frac{K_j[x]}{K_{j-1}[x]}. \tag{2.137}$$

The sequences may be generated via the recurrence relation

$$\rho_{j+1}[x] = \frac{2j}{x} + \frac{1}{\rho_j[x]}, \tag{2.138}$$

where the starting value ρ_1 is determined by direct evaluation of the Bessel functions. The ratio term is found by use of the recurrence relation

$$r_{(m-i),(n-i)}[x_m, x_n] = r_{(m-i-1),(n-i-1)}[x_m, x_n] \times \rho_{m-i}[x_m]/\rho_{n-i}[x_n], \\ i = (k-1), \ldots, 0, \quad k = \min[m, n]. \tag{2.139}$$

Calculation of the product term $p_{m,n}$ involves evaluation of the sequences $\rho_j[x_n]$ and $\varrho_j[x_m]$, given respectively by equation 2.137 and

$$\varrho_j[x] = \frac{I_j[x]}{I_{j-1}[x]}. \tag{2.140}$$

The latter sequence is generated via the recurrence relation

$$\frac{1}{\varrho_{j-1}[x]} = \varrho_j[x] + \frac{2(j-1)}{x}, \tag{2.141}$$

which must be computed downward for stability. The starting value may be computed by use of the technique developed by Gautschi and Slavik [1978]. The product term is found by using the recurrence relation

$$p_{(m-i),(n-i)}[x_m, x_n] = p_{(m-i-1),(n-i-1)}[x_m, x_n] \times \varrho_{m-i}[x_m] \times \rho_{n-i}[x_n], \\ i = (k-1), \ldots, 0, \quad k = \min[m, n]. \quad (2.142)$$

In the recurrence relations for the ratio and product terms, the starting values $r_{(m-k),(n-k)}$ and $p_{(m-k),(n-k)}$ are obtained by direct evaluation of the modified Bessel functions. Negative integer order may be accommodated if necessary by use of the relationships

$$\begin{aligned} K_n[x] &= K_{-n}[x] \\ I_n[x] &= I_{-n}[x]. \end{aligned} \quad (2.143)$$

2.8 Summary

A simulation methodology has been developed for the present investigation of axial and near-axial flow along cylinders. The procedure employed for solution of the governing Navier-Stokes equations is similar to that used by Neves [1992], but here different boundary conditions are adopted. The computational domain extends from the surface of the cylinder to a finite outer radius. The flow is inherently periodic in the azimuthal direction, and periodic boundary conditions are imposed on a finite length in the axial direction. Flow variables are represented by Fourier series in the azimuthal and axial directions and by Chebyshev series mapped non-uniformly to the radial direction. At the cylinder surface, no-slip boundary conditions are imposed. In order to make possible the inclusion of large-scale ejection and cross-flow events such as those observed experimentally, the outer boundary condition is imposed on vorticity rather than requiring the radial velocity component to be zero. The radial component of vorticity is set to zero and the remaining vorticity components are determined so that the resultant vector magnitude is minimised. Vorticity, which is confined to the computational domain, becomes the primary simulation variable, whose evolution is governed by the vorticity transport equation. The velocity field is assumed to be continuous throughout space, with the external potential flow tending to the free-stream at infinity. The velocity field inside the computational domain is determined from the vorticity field at each time-step.

The sequence of major operations in the simulation procedure is as follows:

1. Specify simulation parameters, including radius Reynolds number and free-stream yaw angle, grid geometry and resolution (section 2.3), and time-step size (equation 2.56).

2. Pre-calculate frequently used matrices and formulae:

   (a) Generate Galerkin matrices for velocity calculation (section 2.5.5) and time integration (equation 2.55). Evaluate invariant parts of the expressions for velocity potential $\hat{\Phi}_1$ (equations 2.99 and 2.107).

   (b) If it is desired that the pressure field is to be calculated as part of the simulation, generate the Galerkin matrices for equation 2.110 and evaluate the invariant parts of equations 2.100 and 2.108 at radius b.

   (c) Calculate the vorticity field $\hat{\boldsymbol{\Omega}}_i$ and the corresponding velocity field $\hat{\boldsymbol{U}}_i$ used for enforcement of the no-slip condition at the cylinder surface (sections 2.4.4 and 2.4.5).

3. Initialise the vorticity field (denoted by $\hat{\boldsymbol{\Omega}}_h$ in the following steps), possibly with data from a previous simulation.

4. Calculate the velocity field $\hat{\boldsymbol{U}}_h$ on region R_1 ($a \leq r \leq b$):

   (a) Solve the equations in section 2.5.5 for a velocity field $\hat{\boldsymbol{W}}$ whose curl is the vorticity field $\hat{\boldsymbol{\Omega}}_h$; any convenient boundary conditions may be used.

   (b) Calculate the potential flow velocity $\hat{\boldsymbol{V}}_1$ by use of equations 2.86, 2.96, 2.99 and 2.107.

   (c) Determine the overall velocity field $\hat{\boldsymbol{U}}_h$ by addition of $\hat{\boldsymbol{W}}$, $\hat{\boldsymbol{V}}_1$ and $\hat{\boldsymbol{V}}_\infty$ (equation 2.68). This sets the wall-normal velocity to zero and the velocity at infinity to the free-stream velocity, while ensuring that the velocity is continuous across the outer boundary of the computational domain.

5. Enforce the no-slip condition at the cylinder surface:

   (a) Determine the factors $c_{m,k}$ given by equations 2.61 and 2.67.

   (b) Calculate the vorticity field $\hat{\boldsymbol{\Omega}}$ given by addition of $\hat{\boldsymbol{\Omega}}_h$ and $c_{m,k}\hat{\boldsymbol{\Omega}}_i$ (equation 2.60a).

   (c) The corresponding velocity field $\hat{\boldsymbol{U}}$ is given by addition of $\hat{\boldsymbol{U}}_h$ and $c_{m,k}\hat{\boldsymbol{U}}_i$ (equation 2.60b).

6. If required, calculate the pressure field (section 2.6).

7. If required, export flow fields to a data storage system.

8. Advance the vorticity field to the next time-step:

   (a) Calculate the Chebyshev-Fourier coefficients of the non-linear term (section 2.4.3). The cross-product of velocity and vorticity is evaluated on a grid in the space domain.

   (b) Solve equation 2.55 for the vorticity field $\hat{\boldsymbol{\Omega}}_h$, imposing the boundary conditions of equation 2.59 or 2.65 with $c_{m,k} = 0$.

9. Repeat from step 4 as often as required.

Practical issues associated with implementation of the simulation procedure are addressed in the next chapter.

Chapter 3

Computational Considerations

3.1 Code Development and Verification

The simulation procedure described in the previous chapter has been implemented using the Fortran 95 programming language, with support for parallel execution provided by use of the Message Passing Interface [Message Passing Interface Forum, 1995]. The LAPACK library [Anderson et al., 1999] is used for matrix operations, the FFTW library [Frigo and Johnson, 2005] is used for Fourier and cosine transforms, and the NetCDF library [Rew et al., 2005] is used for file operations. Modified Bessel functions are evaluated by means of recurrence relations (see section 2.7.3) which are initialised using routines from the SLATEC Common Mathematical Library [Fong et al., 1993]. The program has been executed on a variety of server clusters and a shared-memory supercomputer.

The computational resources necessary for direct numerical simulation (DNS) of turbulent flow are immense. Even though the present code has been designed and tuned for high-performance, the most ambitious simulation considered here, which involved $256 \times 384 \times 1280$ mesh points and a total of 1.8×10^5 time-steps, consumed approximately 85 gigabytes of memory and required a running time of 16 days on 96 parallel processors (1.3 GHz Intel® Itanium® 2) of an SGI® Altix® 3000 supercomputer. Such requirements suggest that DNS, which forgoes the use of turbulence models, is perhaps not yet suitable for routine use in engineering design, although as argued by Moin and Krishnan [1998], DNS is particularly effective when used as a tool for turbulence research.

Post-processing of the NetCDF datasets produced by the present simulations has been performed on an ordinary workstation. The post-processing routines have been written for MATLAB®, which provides access to a comprehensive set of numerical

and graphical operations and is available for a variety of operating systems and processors.

Extensive testing of the simulation code at the level of individual procedures and modules has been conducted using a set of test programs developed specifically for the task. For example, the results of the velocity calculation procedure can be checked to ensure that the curl of velocity corresponds to the vorticity and that the required boundary conditions are satisfied. Neves [1992] uses Taylor-Couette flow, for which experimental and computational data are readily available, as a test of his complete simulation code. However, a similar test of the present code would be of questionable value, because considerable program modifications are required to install the appropriate vorticity boundary conditions. The most relevant test cases are those for which the program is primarily designed — external flow over a cylinder.

The simulation code has been applied to an increasingly challenging series of flows and the results validated against the available reference data. The progressive development and validation of the simulation procedure is evident in a series of publications resulting from the present work [Woods and Bull, 2003, 2006, 2004], which are included in the appendix. In the main body of this thesis, the simulation results for cylinders in a variety of free-stream flow conditions are presented and discussed. Wherever practical, the results are assessed with respect to independent experimental and computational data.

3.2 Specification of Flow Parameters

The computational procedure used for the present study ensures that simulations of axial flow along a cylinder reach a statistically-steady state after a sufficient number of time-steps. The flow equations solved are expressed in non-dimensional form with respect to the free-stream velocity magnitude V_∞ and the cylinder radius a. The statistically-steady state is determined by two non-dimensional parameters, the radius ratio of the computational domain, b/a, and the radius Reynolds number, $Re_a = aV_\infty/\nu$, where ν is the kinematic viscosity of the fluid.

The statistically-steady state is independent of initial conditions. However, the initial state of a simulation affects the amount of computational effort required to reach statistical steadiness. Where possible, it is desirable to initialise a simulation with a flow field from a similar, previously completed simulation. In the few cases for which suitable simulated data were not available, the present calculations were

initialised using an assumed mean-flow profile and superimposed random disturbances.

The specified outer radius b of the computational domain affects the boundary layer thickness δ, which is generally defined as the wall-normal distance at which the mean velocity equals $0.99V_\infty$. For chosen values of Re_a and b/a, the time-varying velocity field produced by the calculation may be averaged to determine the wall-normal distribution of mean axial velocity $\overline{U_z}$. The mean velocity distribution yields a value for δ/a; it also leads to non-dimensional values of the wall-shear-stress $\tau_w = \rho\nu\, d\overline{U_z}/dr[a]$ and friction velocity $u_\tau = \sqrt{\tau_w/\rho}$, where ρ is the density of the fluid. The ratio ν/u_τ is a wall unit of length; the boundary layer thickness in wall units is denoted by δ^+ and is equal to $\delta u_\tau/\nu$. Similarly, the cylinder radius in wall units is $a^+ = au_\tau/\nu$.

The flow parameters selected for the present simulations are intended to allow the separate effects of a^+, δ^+ and their ratio δ/a to be identified. Consequently, there are several series of simulations where one of these parameters is held approximately constant while the others are varied. Over successive simulations, flow parameters have been advanced towards those of the cylinder experiments of Luxton et al. [1984] and Berera [2004] (see also Berera and Bull [2001]) and the plane-channel simulations of Kim et al. [1987] and Moser, Kim, and Mansour [1999]. The flows considered in direct numerical simulations by Neves [1992] (see also Neves et al. [1994], Neves and Moin [1994]) have also been simulated by the present procedure to allow detailed validation of the present results and to investigate the effects of the vorticity boundary conditions.

3.3 Geometrical and Temporal Parameters

Mesh geometry parameters for the axial-flow simulations are listed in table 3.1. The mesh resolution in wall units (ν/u_τ) for each simulation is given in table 3.2. The simulation procedure accepts length parameters that are non-dimensional with respect to the cylinder radius a, so the conversion to wall units is achieved by multiplication of the length parameters by the values of a^+ taken from table 4.1 in the next chapter.

The axial length L_z of the computational domain is required to contain the largest significant turbulence structures. These structures can be expected to become larger as the width $(b-a)$ of the computational domain increases. For the plane-channel simulations of Moser et al. [1999], domain lengths in the range 2π to 4π channel half-widths are found to be sufficient. The cylinder simulations of Neves [1992] employ

Re_a	b/a	N_r	N_Ω	N_θ	N_z	η	L_z/a	$L_z/(b-a)$
311	12	96	80	128	384	3.00	207	18.8
311	21	128	112	192	384	3.00	207	10.4
311	31	160	144	288	384	3.00	207	6.9
311	41	210	192	256	384	5.83	207	5.2
492	12	160	160	192	576	∞	207	18.8
674	6	96	80	128	320	3.00	94.2	18.8
674	12	160	144	256	768	3.00	94.2	18.8
1300	4	96	80	128	320	3.00	56.5	18.8
1300	6	168	168	256	840	∞	113.0	22.6
2600	2.5	96	80	256	320	3.00	28.3	18.9
2600	4	128	112	256	640	3.00	56.5	18.8
2600	6	180	164	256	1024	5.83	94.2	18.8
3300	7.3	256	240	384	1280	5.83	94.2	15.0
5200	1.75	96	80	512	320	3.00	14.1	18.8
10400	1.4	96	80	1024	320	3.00	7.54	18.9
20800	1.2	96	80	2048	320	3.00	3.77	18.9

Table 3.1: Grid geometry parameters

Re_a	b/a	a^+	Δr_i^+	$\Delta r_{\max}^+$	$\Delta r_o/\Delta r_i$	$a^+\Delta\theta$	$b^+\Delta\theta$	Δz^+
311	12	21.9	0.093	5.26	4.00	1.07	12.88	11.78
311	21	21.5	0.085	6.71	4.00	0.70	14.78	11.59
311	31	21.5	0.077	7.84	4.00	0.47	14.55	11.60
311	41	21.0	0.080	7.08	2.00	0.52	21.15	11.33
492	12	31.5	0.067	3.40	1.00	1.03	12.35	11.31
674	6	42.7	0.082	4.66	4.00	2.09	12.57	12.56
674	12	40.8	0.053	5.44	4.00	1.00	12.00	10.98
1300	4	76.0	0.088	4.98	4.00	3.73	14.91	13.41
1300	6	74.3	0.065	3.47	1.00	1.82	10.94	10.00
2600	2.5	146	0.085	4.79	4.00	3.59	8.97	12.93
2600	4	140	0.083	6.55	4.00	3.43	13.73	12.35
2600	6	131	0.085	6.48	2.00	3.23	19.35	12.09
3300	7.3	163	0.062	6.92	2.00	2.67	19.47	12.00
5200	1.75	287	0.083	4.71	4.00	3.52	6.17	12.65
10400	1.4	564	0.087	4.93	4.00	3.46	4.85	13.30
20800	1.2	1130	0.087	4.92	4.00	3.45	4.14	13.26

Table 3.2: Grid resolution in mean-flow wall units.

domain lengths of $4\pi(b-a)$ and $6\pi(b-a)$. The domain length used for the present simulations is intended to be set to approximately $6\pi(b-a)$, although some flow cases employ reduced values as dictated by the computational resources available at the appropriate times. The adequacy of the domain length is judged, in section 3.4, by analysis of the streamwise correlation functions of the calculated flows.

The number of grid points in the azimuthal and axial directions is denoted respectively by N_θ and N_z. The Chebyshev series representation for the radial distribution of vorticity uses N_Ω coefficients. The number N_r of Chebyshev coefficients used to represent quantities that are derived from the vorticity field, such as velocity and (in turn) pressure, is typically made larger than N_Ω to improve the accuracy with which the derived quantities are calculated. Initial values for N_Ω, N_r, N_θ and N_z are estimated by extrapolation from previous simulations, with the complication that any values chosen are required by the Fast Fourier Transform software to be expressible as products of small prime numbers. The grid resolution parameters are assessed by examination of spatial spectra of the calculated flow fields, as discussed in section 3.4.

The Chebyshev-Fourier decomposition of the flow uses the same number of coefficients as there are spatial grid points. Thus the number of spatial grid points is the minimum necessary to transform the flow fields between the Chebyshev-Fourier and space domains. The number of Chebyshev-Fourier coefficients required to represent the non-linear term of the vorticity transport equation without truncation is greater than the number used for either the velocity or vorticity fields (see section 2.4.3). However, in the present simulations, the non-linear term is evaluated using the same number of spatial grid points and Chebyshev-Fourier coefficients as are used for the velocity field. The coefficients of the non-linear term that are neglected at high mode-numbers cause so-called aliasing errors in the remaining coefficients at low mode-numbers. The high spatial resolutions used for the present study ensure that the absolute values of the neglected coefficients are small, therefore the significant computational effort that would be required to eliminate the aliasing errors from the non-linear term is not considered justified.

The shape parameter η controls the mapping of Chebyshev grid points to the radial direction (equation 2.34). To explain the effect of η on the radial grid, it is useful to consider the values of $\Delta r_{\max}$, Δr_i and Δr_o, which denote respectively the maximum, innermost and outermost radial spacing between adjacent grid points. When $\eta = \infty$, the radial spacing of the grid increases from minima at the innermost and outermost edges of the grid, with $\Delta r_i = \Delta r_o$, to a maximum $\Delta r_{\max}$ at the radial mid-point of the grid. As η is decreased from ∞ towards 1, a given value of

the innermost spacing Δr_i is maintained by simultaneously decreasing the number of grid points, which is N_Ω for the vorticity field. The reduction of both η and N_Ω increases the outermost spacing Δr_o, which typically increases the maximum stable value of the simulation time-step (see equation 2.56) and thereby reduces computational effort. The acceptable ranges of N_Ω and η are constrained by the need to limit the size of the maximum spacing $\Delta r_{\max}$. Values $\eta \approx \infty, 5.83, 3.00$ have been used for the present simulations; corresponding ratios of the outermost to the innermost radial grid spacing are $\Delta r_o / \Delta r_i \approx 1, 2, 4$. Values of N_Ω and η are assigned to the simulations so that the grid spacing in wall units has a typical minimum of $\Delta r_i^+ \approx 0.08$ and a typical maximum of $\Delta r_{\max}^+ \approx 7$.

The azimuthal grid spacing is proportional to radial position. Acceptable maximum values of the azimuthal grid spacing $\Delta\theta = 2\pi/N_\theta$ are found to be the lesser of $\Delta\theta \approx 4/a^+$ and $\Delta\theta \approx 20/b^+$. The axial grid spacing is uniform in the axial direction, with a typical value of $\Delta z^+ = a^+(L_z/a)/N_z \approx 12$. The size of the smallest turbulent eddies is of the order of the Kolmogorov length-scale, which is defined by

$$L_K = \left(\frac{\nu^3}{\epsilon} \right)^{1/4}, \tag{3.1}$$

where ϵ denotes the rate of energy dissipation by viscosity per unit volume of fluid evaluated from the simulation data (see section 4.4). For all of the present simulations, the grid spacing throughout the computational domain is found to be less than $3L_K$ in the azimuthal direction and less than $9L_K$ in the axial direction.

The simulation procedure accepts temporal parameters normalised by the time-scale a/V_∞. Other time-scales may be derived from combinations of the flow quantities a, δ, V_∞, u_τ and ν; the shortest time-scale is ν/u_τ^2 and the longest is δ/u_τ. The different time-scales may be obtained from a/V_∞ by use of the mean-flow parameters listed in table 4.1 in the next chapter.

Where appropriate, the simulation data reported in this thesis are averaged in the azimuthal and axial directions and also in time, with the temporal averaging parameters given in table 3.3. The number of temporal samples N_T spans a temporal record of duration L_T. For the majority of flow cases, L_T is several times greater than the time-scale δ/u_τ. In the small number of flow cases where $L_T < \delta/u_\tau$, the calculated statistics appear to be consistent with neighbouring flow cases; extension of these time records would reduce uncertainty in the corresponding statistics.

The temporal parameters used to obtain sampled time-series for a subset of the flow cases are listed in table 3.4. The sample period Δt_s is set so that the highest frequency represented without ambiguity (the Nyquist frequency $0.5/\Delta t_s$) is close

Re_a	b/a	N_T	$L_T V_\infty/a$	$L_T u_\tau/\delta$	$L_T u_\tau^2/\nu$
311	12	10	900	8.09	1383
311	21	7	600	2.96	892
311	31	15	1750	6.33	2606
311	41	7	525	1.29	746
492	12	20	95	0.77	191
674	6	11	313	5.30	846
674	12	10	675	5.27	1663
1300	4	4	112	2.81	497
1300	6	10	31	0.49	132
2600	2.5	3	40	1.91	329
2600	4	5	80	1.87	602
2600	6	3	25	0.32	166
3300	7.3	8	70	0.70	564
5200	1.75	3	15	1.44	238
10400	1.4	5	7	1.21	214
20800	1.2	5	4	1.38	243

Table 3.3: Temporal averaging intervals

Re_a	311	311	674	3300
b/a	12	31	12	7.3
N_t	320	768	640	1750
N_i	19	12	12	1
N_T	3200	4992	4160	1750
$\Delta t_s V_\infty/a$	0.3000	0.3750	0.1875	0.0400
$\Delta t_s u_\tau/\delta$	2.70×10^{-3}	1.36×10^{-3}	1.47×10^{-3}	4.02×10^{-4}
$\Delta t_s u_\tau^2/\nu$	0.461	0.558	0.462	0.322
$L_t V_\infty/a$	96	288	120	70
$L_t u_\tau/\delta$	0.863	1.044	0.939	0.703
$L_t u_\tau^2/\nu$	148	429	296	563
$L_T V_\infty/a$	960	1872	780	70
$L_T u_\tau/\delta$	8.63	6.79	6.10	0.70
$L_T u_\tau^2/\nu$	1475	2787	1922	563

Table 3.4: Temporal resolution of time-series

to $1/(\nu/u_\tau^2)$, therefore $\Delta t_s u_\tau^2/\nu \approx 0.5$. Power spectra and correlation functions are computed on temporal intervals of duration $L_t = N_t \Delta t_s$, where the number of samples N_t is required by the Fast Fourier Transform software to be expressible as a product of small prime numbers. The duration of the intervals is specified so that the lowest resolvable frequency $1/L_t$ is close to $1/(\delta/u_\tau)$, therefore $L_t u_\tau/\delta \approx 1$. Where practical, the calculated statistics are averaged across a number of temporal intervals that overlap one another by $0.5L_t$. The overlapping intervals correspond to a temporal record containing $N_T = N_t(N_i+1)/2$ unique samples, where N_i is the number of intervals. The duration of the temporal record is $L_T = N_T \Delta t_s$.

3.4 Mesh Validation

Mesh resolution is typically verified in computational studies by comparison of results calculated at different levels of mesh refinement. However, such an approach is not attractive for DNS because of the very large computational workload involved. For a pseudo-spectral method such as that employed here, examination of the Fourier coefficients gives a good indication of the adequacy of mesh resolution. In particular, the coefficients are required to decay to a small value at high spatial wave-numbers. In the case of turbulent flow, a smoothly decaying wave-number spectrum reflects the cascade of energy from large to small scales of turbulence. Deviation from smooth decay at high wave-numbers may possibly indicate that the grid resolution is insufficient.

Azimuthal and axial wave-numbers, denoted respectively by k_θ and k_z, are defined by equations 2.26 and 2.27. The azimuthal and axial spectra for the axial component of velocity U_z are defined respectively by

$$E_{u_z}[k_\theta] = c_\theta \overline{\left| \sum_{n=0}^{N_\theta - 1} U_z[n\Delta\theta] \, \exp\left[-ik_\theta r n \Delta\theta\right] \right|^2} \tag{3.2}$$

and

$$E_{u_z}[k_z] = c_z \overline{\left| \sum_{n=0}^{N_z - 1} U_z[n\Delta z] \, \exp\left[-ik_z n \Delta z\right] \right|^2}, \tag{3.3}$$

where $\Delta\theta$ and Δz denote the spatial grid spacing. The overbar denotes averaging in the azimuthal or axial direction and over the temporal record. The scale factors

c_θ and c_z are set so that when E_{u_z} is plotted against wave-number, the area under the single-sided spectrum equals the mean-square value of U_z, that is

$$\int_{k_\theta \geq 0} E_{u_z}[k_\theta]\, dk_\theta = \int_{k_z \geq 0} E_{u_z}[k_z]\, dk_z = \overline{U_z^2}. \tag{3.4}$$

Azimuthal spectra of the axial velocity component are shown in figure 3.1. Normalisation with respect to δ is achieved by use of the mean-flow parameters listed in table 4.1 in the next chapter. Results are shown for two different wall-normal positions: near the wall at the grid points closest to $y^+ = 10$, and near the outer edge of the boundary layer at the grid points closest to $y/\delta = 1$. The spectra decay by five or more orders of magnitude over the range of azimuthal wave-numbers in each simulation. The presence of upwardly curved "hooks" at the high wave-number ends of some of the spectra suggests that a slight increase in grid resolution may be necessary. However, the size of the hooks is greatly emphasised by the logarithmic scale, and it is considered that an increase in azimuthal resolution would not produce a worthwhile improvement in the quality of the simulation results.

Axial spectra of the axial velocity component near the inner and outer edges of the boundary layer are shown in figure 3.2. Near the high wave-number limits of the simulations, the spectra decay smoothly to levels that are five or more orders of magnitude smaller than the maxima. The axial grid resolution is therefore considered to be sufficient.

The axial length L_z of the computational domain is intended to be significantly larger than the largest turbulence structures. The two-point correlation function gives an indication of the typical length of turbulence structures in a given direction. For the axial velocity component, which is composed of fluctuations u_z relative to the mean $\overline{U_z}$, the two-point correlation as a function of axial separation Δz is defined by

$$R_{u_z}[\Delta z] = \overline{u_z[z]\, u_z[z + \Delta z]} \,/\, \overline{u_z^2}. \tag{3.5}$$

The overbar indicates the average value calculated over the azimuthal and axial directions and over the temporal record. Normalisation of the correlation function by the mean-square value of u_z ensures that the maximum value of R_{u_z} is unity when Δz is zero.

Axial correlations for the present simulations are shown in figure 3.3. Near the wall (figure 3.3a), the turbulence is essentially uncorrelated for separations larger than half of the domain length. Near the outer edge of the boundary layer (figure 3.3b), where larger turbulent eddies are found, the domain half-length of all flow cases is adequate to allow the correlation function to decay to less than 20% of

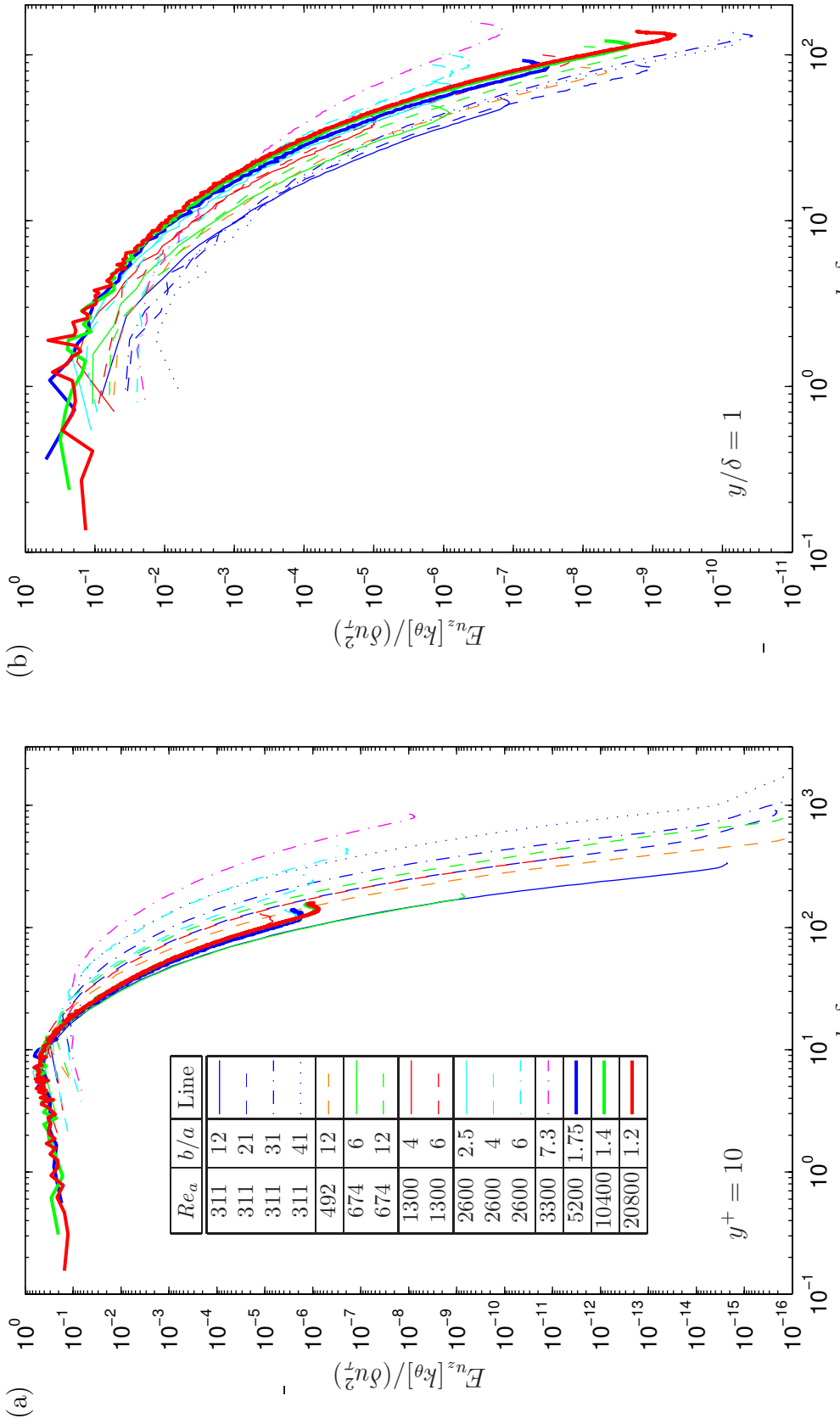

Figure 3.1: Azimuthal spectra of the axial velocity component at (a) $y^+ = 10$ and (b) $y/\delta = 1$.

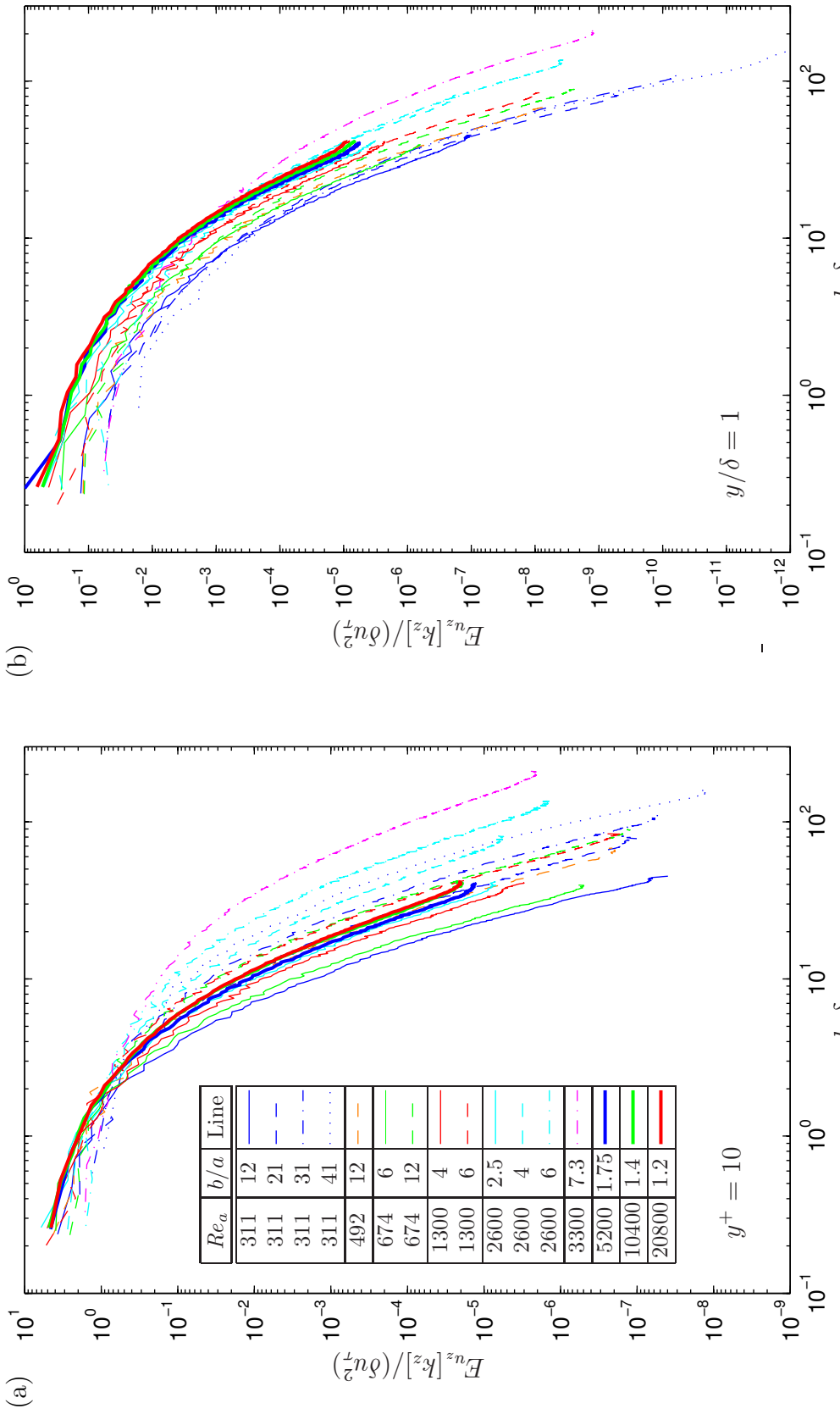

Figure 3.2: Axial spectra of the axial velocity component at (a) $y^+ = 10$ and (b) $y/\delta = 1$.

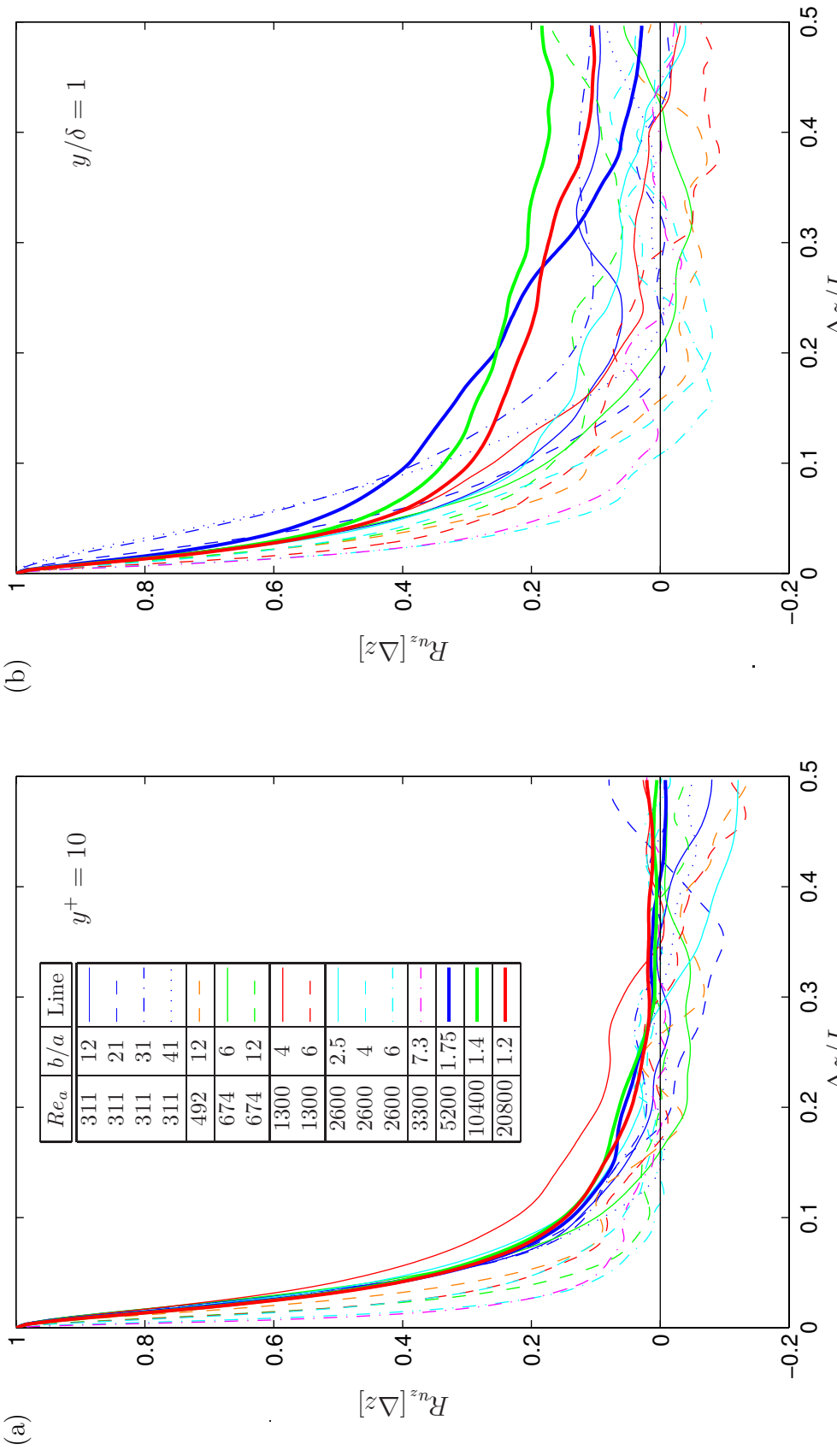

Figure 3.3: Axial two-point correlations of axial velocity fluctuations at (a) $y^+ = 10$ and (b) $y/\delta = 1$.

the maximum value. Use of data from a longer temporal record may possibly yield correlation functions for the outer flow that decay more completely without alteration of the axial domain lengths. However, the domain lengths used for the present simulations are considered sufficient to allow detailed comparison of the calculated results with those of previous DNS studies.

3.5 Statistical Steadiness

The velocity field $\boldsymbol{U}$ consists of turbulence fluctuations $\boldsymbol{u}$ superimposed on the spatial- and temporal-mean flow $\overline{\boldsymbol{U}}$. Mean and fluctuating contributions to other quantities are denoted similarly.

The present simulations of axial flow over a cylinder reach a statistically-steady state after a sufficient number of time-steps. At the statistically-steady state, there is no variation of the mean flow in time or in the azimuthal and axial directions. Under such conditions, the incompressible Navier-Stokes equation for the mean axial velocity component (the Reynolds-average of equation 2.11c) reduces to

$$\frac{1}{\rho}\frac{d\overline{P}}{dz} = \frac{1}{r}\frac{d}{dr}\left(\nu r\frac{d\overline{U_z}}{dr} - r\overline{u_r u_z}\right). \tag{3.6}$$

At the statistically-steady state, the radial variation of the combined Reynolds and viscous shear-stress is required to balance the axial component of the mean pressure-gradient.

Multiplication of equation 3.6 by r and integration with respect to r from a to a given radius R yields

$$\frac{1}{\rho}\frac{d\overline{P}}{dz}\left(\frac{R^2-a^2}{2}\right) = \nu\left(R\frac{d\overline{U_z}}{dr}[R] - a\frac{d\overline{U_z}}{dr}[a]\right) - \left(R\,\overline{u_r u_z}[R] - a\,\overline{u_r u_z}[a]\right), \tag{3.7}$$

where the axial component of the mean pressure-gradient is required to be independent of radius so that the radial component of the mean pressure-gradient is independent of axial position. Evaluation of equation 3.7 at $R = b$ and use of the velocity boundary conditions allows the pressure-gradient to be expressed as

$$\frac{1}{\rho}\frac{d\overline{P}}{dz} = -\left(\frac{2}{b^2-a^2}\right)\left\{a\nu\frac{d\overline{U_z}}{dr}[a] + b\,\overline{u_r u_z}[b]\right\}. \tag{3.8}$$

The first term inside braces involves $\nu\, d\overline{U_z}/dr[a]$, which is equal to the wall-shear-stress τ_w divided by the fluid density ρ. The second term involves the Reynolds shear-stress at the outer mesh boundary, which is not formally zero but is typically

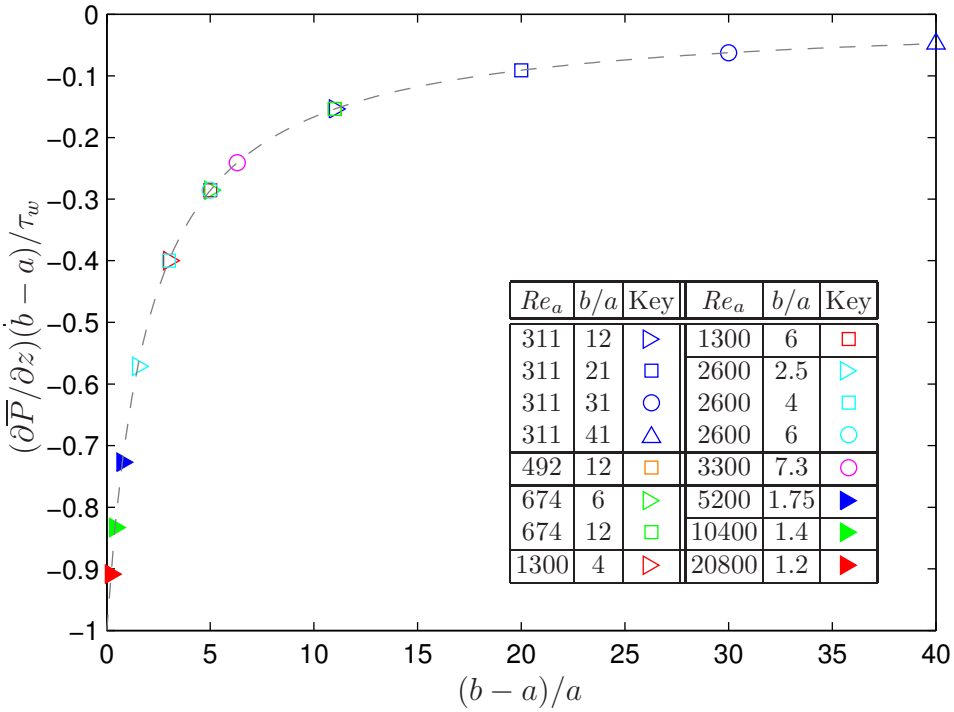

Re_a	b/a	Key	Re_a	b/a	Key
311	12	▷	1300	6	□
311	21	□	2600	2.5	▷
311	31	○	2600	4	□
311	41	△	2600	6	○
492	12	□	3300	7.3	○
674	6	▷	5200	1.75	▶
674	12	□	10400	1.4	▶
1300	4	▷	20800	1.2	▶

Figure 3.4: Axial pressure-gradient at the statistically-steady state. Symbols are for present simulations; – – $(d\overline{P}/dz)(b-a)/\tau_w = -2a/(b+a) = -2/(2+(b-a)/a)$.

very small compared with τ_w/ρ. The axial pressure-gradient corresponding to each simulation is shown in figure 3.4.

Replacement of the pressure-gradient in equation 3.7 leads to an expression for the total shear-stress $\overline{\tau}$:

$$\begin{aligned}\frac{\overline{\tau}[r]}{\rho} &= -\overline{u_r u_z}[r] + \nu\frac{d\overline{U_z}}{dr}[r] \\ &= \left(\frac{a}{r}\right)\left(\frac{b^2-r^2}{b^2-a^2}\right)\nu\frac{d\overline{U_z}}{dr}[a] - \left(\frac{b}{r}\right)\left(\frac{r^2-a^2}{b^2-a^2}\right)\overline{u_r u_z}[b].\end{aligned} \tag{3.9}$$

The radial distribution of total shear-stress is thus expressed analytically in terms of boundary values of the simulation statistics.

An interesting geometrical interpretation of the total shear-stress distribution emerges when equation 3.9, with $\overline{u_r u_z}[b]$ assumed negligible, is rearranged as follows:

$$\begin{aligned}\frac{\overline{\tau}}{\tau_w} &\approx \left(\frac{\pi(a+h)^2-\pi(a+y)^2}{2\pi(a+y)}\right)\Big/\left(\frac{\pi(a+h)^2-\pi(a+0)^2}{2\pi(a+0)}\right) \\ &= \frac{A_c[y,h]/L_c[y]}{A_c[0,h]/L_c[0]}.\end{aligned} \tag{3.10}$$

In the above expression, h is the radial width $(b-a)$ of the computational domain, y is a given wall-normal position, $L_c[y]$ is the circumference of a circle of radius $a+y$, and $A_c[y,h]$ is the area of the annular region between radial positions $a+y$ and $a+h$. Thus the total shear-stress at y is proportional to the ratio of the cross-sectional area of the boundary layer outside y to the total cross-sectional area of the boundary layer, with both areas normalised by their corresponding inner circumferential lengths.

A simulation is considered to have reached statistical steadiness when the calculated total shear-stress profile matches the analytical profile given by equation 3.9. The close agreement of calculated values of $\overline{\tau}$ with the analytically-derived profiles for the simulations listed in tables 3.1–3.4 is shown in figure 3.5. Further evidence that the present simulations have reached a statistically-steady state is provided by analysis of the turbulence kinetic energy budget, which is considered later in section 4.4.

3.6 Summary

The simulation procedure described in chapter 2 has been implemented as a computer program for parallel execution on multiple processors.

Simulations of the turbulent boundary layer on a cylinder in axial flow reach a statistically-steady state that depends on the radius Reynolds number, $Re_a = aV_\infty/\nu$, and the ratio of the outer grid radius to the cylinder radius, b/a. The temporal, azimuthal and axial average of the calculated velocity field yields values for the boundary layer thickness, in the form δ/a, and the friction velocity, in the form u_τ/V_∞.

Grid geometry and temporal parameters are given in section 3.3 for a series of axial-flow simulations that are intended to allow the separate effects of the mean-flow parameters $a^+ = au_\tau/\nu$, $\delta^+ = \delta u_\tau/\nu$ and δ/a to be identified. Suitable values of the grid geometry and temporal parameters are initially estimated by extrapolation from successful simulations. The spatial spectra and axial correlations of the calculated flow fields are examined in section 3.4 to verify that mesh resolution and domain length are adequate.

In the statistically-steady state, the effect of the applied boundary conditions is equivalent to that produced by a streamwise pressure-gradient; the streamwise and temporal development of the mean flow are suppressed. An analytical expression for the streamwise pressure-gradient is derived in section 3.5. The corresponding

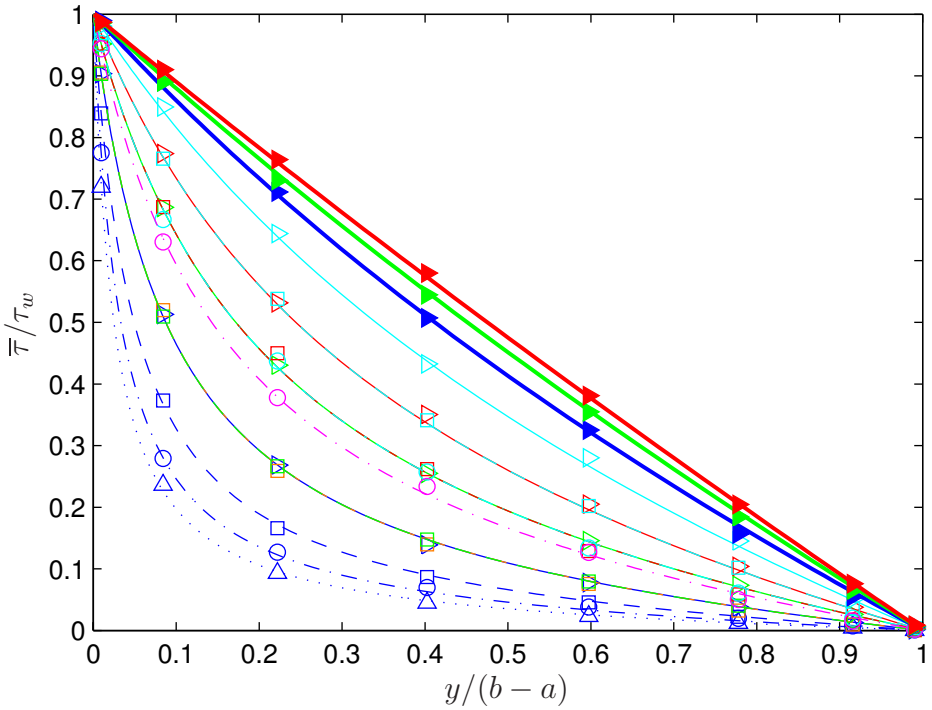

Figure 3.5: Total shear-stress normalised by wall-shear-stress. Lines are evaluated with equation 3.9, symbols are data points calculated directly from simulation data. Legend:

Re_a	b/a	Line & Symbol	Re_a	b/a	Line & Symbol	Re_a	b/a	Line & Symbol	Re_a	b/a	Line & Symbol
311	12		492	12		1300	6		3300	7.3	
311	21		674	6		2600	2.5		5200	1.75	
311	31		674	12		2600	4		10400	1.4	
311	41		1300	4		2600	6		20800	1.2	

expression for the total shear-stress is used to verify that the simulations achieve statistical steadiness.

Chapter 4

Velocity Statistics

Simulations of axial flow over cylinders have been advanced to the statistically-steady state using the method described in chapter 2. The grid geometry and resolution parameters used for the simulations are listed in tables 3.1 and 3.2. A temporal record of the turbulent flow fields at the statistically-steady state has been obtained for each of the simulations, in accordance with the temporal parameters listed in tables 3.3 and 3.4.

The recorded flow fields have been analysed to obtain a variety of velocity statistics. The statistics are presented here in conjunction with appropriate reference data for planar and axisymmetric boundary layers. The trends in the data are examined to determine the effects of transverse wall curvature on the velocity field. Attention is first given to the mean velocity profiles and the parameters derived from them. Attention is then focused on the turbulence statistics, including the Reynolds shear-stress, the intensity and higher-order moments of the velocity fluctuations, and the root-mean-square fluctuations of vorticity. The scaling relations applicable to the velocity statistics are of particular interest. The main findings are summarised at the end of the chapter.

4.1 Mean Velocity

The velocity fields calculated for a given flow by the present simulation procedure may be averaged in the azimuthal and axial directions and over the temporal record to obtain the mean velocity $\overline{U_z}$ as a function of the wall-normal position $y = r - a$. A number of parameters used for similarity scaling of boundary layer flow are derived from the mean velocity profile. Two fundamental parameters are the boundary layer

Re_a	b/a	δ/a	Re_δ	u_τ/V_∞	C_f	a^+	δ^+
311	12.00	7.82	2430	0.0703	9.88×10^{-3}	21.9	171
311	21.00	14.0	4360	0.0691	9.56×10^{-3}	21.5	302
311	31.00	19.1	5950	0.0692	9.58×10^{-3}	21.5	411
311	41.00	27.6	8570	0.0676	9.14×10^{-3}	21.0	580
492	12.00	7.85	3860	0.0639	8.18×10^{-3}	31.5	247
674	6.00	3.74	2520	0.0633	8.02×10^{-3}	42.7	159
674	12.00	7.74	5220	0.0605	7.31×10^{-3}	40.8	315
1300	4.00	2.33	3030	0.0584	6.83×10^{-3}	76.0	177
1300	6.00	3.63	4720	0.0572	6.53×10^{-3}	74.3	270
2600	2.50	1.18	3070	0.0562	6.32×10^{-3}	146	173
2600	4.00	2.30	5970	0.0538	5.79×10^{-3}	140	321
2600	6.00	4.01	10400	0.0505	5.11×10^{-3}	131	527
3300	7.30	4.92	16200	0.0494	4.88×10^{-3}	163	802
5200	1.75	0.574	2990	0.0552	6.10×10^{-3}	287	165
10400	1.40	0.313	3260	0.0543	5.89×10^{-3}	564	177
20800	1.20	0.157	3270	0.0541	5.85×10^{-3}	1130	177

Table 4.1: Mean-flow parameters for present simulations.

thickness δ, defined as the wall-normal distance at which the mean velocity equals $0.99V_\infty$, and the wall-shear-stress τ_w, defined by

$$\frac{\tau_w}{\rho} = \nu \frac{d\overline{U_z}}{dy}[y = 0]. \tag{4.1}$$

Another important parameter is the friction velocity u_τ, which is related to the wall-shear-stress by

$$\rho u_\tau^2 = \tau_w. \tag{4.2}$$

The mean-flow parameters given by the present simulations are listed in table 4.1. The simulations are identified by the radius Reynolds number,

$$Re_a = aV_\infty/\nu, \tag{4.3}$$

and the ratio b/a, where b denotes the outer radial limit of the computational domain and a is the cylinder radius. The calculated values of boundary layer thickness and friction velocity are listed in the non-dimensional forms δ/a and u_τ/V_∞. The remaining quantities in the table follow from Re_a, δ/a and u_τ/V_∞. The Reynolds number Re_δ is given by

$$Re_\delta = \frac{\delta V_\infty}{\nu} = Re_a \frac{\delta}{a}, \tag{4.4}$$

and the skin friction coefficient C_f is given by

$$C_f = \frac{\tau_w}{\frac{1}{2}\rho V_\infty^2} = 2\left(\frac{u_\tau}{V_\infty}\right)^2. \tag{4.5}$$

The superscript '+' in the quantities a^+ and δ^+ denotes scaling with respect to parameters that are associated with the near-wall flow. To produce a length-scale, the parameters u_τ and ν are combined to give the wall unit ν/u_τ. The cylinder radius and boundary layer thickness in wall units are given by

$$a^+ = \frac{a u_\tau}{\nu} = Re_a \frac{u_\tau}{V_\infty}, \tag{4.6}$$

$$\delta^+ = \frac{\delta u_\tau}{\nu} = Re_\delta \frac{u_\tau}{V_\infty}. \tag{4.7}$$

The boundary layer thickness in wall units (δ^+) has the form of a Reynolds number, and it is denoted by some authors as Re_τ.

Mean-flow parameters from various sources, for comparison with the present data, are listed in table 4.2. Data for cylinders are taken from the experiments of Berera [2004], Luxton et al. [1984], Snarski and Lueptow [1995] and Willmarth et al. [1976] as well as the simulations of Neves [1992]. Flat-plate data are those from the experiments of Farabee and Casarella [1991] and Schewe [1983] and the plane-channel simulations of Kim et al. [1987] and Moser et al. [1999]. For the numerical investigations, the symbol h is used to denote the plane-channel half-width or the radial width $(b-a)$ of the computational domain. The simulation parameters listed in the table have been adjusted for consistency with the present definition of δ, values of which have been estimated from published mean velocity profiles.

Numerical values of the mean-flow parameters for the present simulations are in good agreement with those of comparable reference data. The simulations of Neves [1992] for $Re_a = 311,674$ and $b/a = 12,6$ give, respectively, $u_\tau/V_\infty = 0.0699, 0.0635$; the present simulation procedure yields $u_\tau/V_\infty = 0.0703, 0.0633$ for the same flow cases. The experiment of Luxton et al. [1984] for $Re_a = 325$ and $\delta/a = 39.1$ corresponds to $u_\tau/V_\infty = 0.0742$; the present simulation with $Re_a = 311$ and $\delta/a = 27.6$ produces $u_\tau/V_\infty = 0.0676$. The experiment of Berera [2004] at $Re_a = 3160$ with $\delta/a = 4.8$ gives $u_\tau/V_\infty = 0.0505$; in an independent experiment, Snarski and Lueptow [1995] obtain the values $Re_a = 3642$, $\delta/a = 5.04$ and $u_\tau/V_\infty = 0.0486$; the corresponding results from the present work are $Re_a = 3300$, $\delta/a = 4.92$ and $u_\tau/V_\infty = 0.0494$.

Reference	Re_a	δ/a	δ/h	Re_δ	u_τ/V_∞	C_f	a^+	δ^+
Berera [2004]	3280	3.2	-	10500	0.0534	5.70×10^{-3}	175	560
	3160	4.8		15200	0.0505	5.10×10^{-3}	160	767
	3460	6.6		22800	0.0490	4.80×10^{-3}	169	1120
	3310	9.4		31100	0.0485	4.70×10^{-3}	160	1510
	3260	11.5		37500	0.0485	4.70×10^{-3}	158	1820
Farabee and	∞	0	-	29000	0.0403	3.25×10^{-3}	∞	1170
Casarella [1991]				53000	0.0379	2.87×10^{-3}		2010
Kim et al. [1987]	∞	0	0.82	2710	0.0545	5.95×10^{-3}	∞	148
Luxton et al.	140	41.6	-	5820	0.0922	1.70×10^{-2}	12.9	536
[1984]	325	39.1		12700	0.0742	1.10×10^{-2}	24.1	943
	455	26.9		12200	0.0707	1.00×10^{-2}	32.2	865
	620	26.7		16600	0.0645	8.32×10^{-3}	40.0	1070
	785	26.0		20400	0.0604	7.30×10^{-3}	47.4	1230
Moser et al.	∞	0	0.84	2730	0.0546	5.97×10^{-3}	∞	149
[1999]			0.83	6560	0.0497	4.93×10^{-3}		326
			0.84	10500	0.0470	4.42×10^{-3}		495
Neves [1992]	311	9.23	0.84	2870	0.0699	9.78×10^{-3}	21.7	201
	674	4.20	0.84	2830	0.0635	8.07×10^{-3}	42.8	180
Schewe [1983]	∞	0	-	12500	0.0444	3.94×10^{-3}	∞	556
Snarski and	3642	5.04	-	18400	0.0486	4.72×10^{-3}	177	892
Lueptow [1995]								
Willmarth et al.	736	37.5	-	27600	0.0626	7.83×10^{-3}	46.1	1730
[1976]	1439	27.0		38900	0.0579	6.71×10^{-3}	83.4	2250
	4330	16.0		69300	0.0458	4.19×10^{-3}	198	3170
	9494	9.45		89700	0.0409	3.35×10^{-3}	389	3670
	23100	4.64		107000	0.0386	2.98×10^{-3}	891	4130
	74260	1.76		131000	0.0365	2.66×10^{-3}	2710	4770

Table 4.2: Mean-flow parameters for reference data.

Experimental results for boundary layers are presented by some authors in non-dimensional form with respect to the displacement thickness δ^* or the momentum thickness θ^*. These integral thickness parameters are often less difficult to obtain from measurements of the mean velocity profile than the parameters δ and τ_w. The integral thickness parameters for axisymmetric boundary layers are defined by

$$(\delta^* + a)^2 - a^2 = 2\int_a^{a+\delta} \left(1 - \frac{\overline{U_z}}{V_\infty}\right) r\, dr, \tag{4.8}$$

$$(\theta^* + a)^2 - a^2 = 2\int_a^{a+\delta} \frac{\overline{U_z}}{V_\infty}\left(1 - \frac{\overline{U_z}}{V_\infty}\right) r\, dr. \tag{4.9}$$

These definitions reduce to those for a flat plate in the limit as δ/a approaches zero.

Re_a	δ/a	Re_δ	δ^*/δ	θ^*/δ	δ^*/θ^*
311	7.82	2430	0.190	0.159	1.19
311	14.0	4360	0.184	0.167	1.10
311	19.1	5950	0.179	0.166	1.08
311	27.6	8570	0.182	0.172	1.06
492	7.85	3860	0.182	0.158	1.16
674	3.74	2520	0.189	0.147	1.29
674	7.74	5220	0.176	0.154	1.14
1300	2.33	3030	0.180	0.135	1.34
1300	3.63	4720	0.178	0.145	1.23
2600	1.18	3070	0.175	0.123	1.43
2600	2.30	5970	0.168	0.133	1.26
2600	4.01	10400	0.180	0.153	1.18
3300	4.92	16200	0.172	0.151	1.14
5200	0.574	2990	0.174	0.116	1.51
10400	0.313	3260	0.167	0.110	1.53
20800	0.157	3270	0.168	0.109	1.55

Table 4.3: Integral thickness parameters for present simulations.

Boundary layer integral thickness parameters for the present simulations and reference data are given in tables 4.3 and 4.4. The shape factors δ^*/θ^* for the present simulations are in quantitative agreement with those of the corresponding reference data. The simulations of Neves [1992] for $Re_a = 311, 674$ and $b/a = 12, 6$ give, respectively, $\delta^*/\theta^* = 1.15, 1.25$; the present simulation procedure yields $\delta^*/\theta^* = 1.19, 1.29$ for the same flow cases. The experiment of Luxton et al. [1984] at $Re_a = 325$ with $\delta/a = 39.1$ corresponds to $\delta^*/\theta^* = 1.10$; the present simulation at $Re_a = 311$ with $\delta/a = 27.6$ produces $\delta^*/\theta^* = 1.06$. The experiment of Berera [2004] at $Re_a = 3160$ with $\delta/a = 4.8$ gives $\delta^*/\theta^* = 1.19$; the experiment of Snarski and Lueptow [1995] at $Re_a = 3642$ with $\delta/a = 5.04$ yields $\delta^*/\theta^* = 1.14$; the corresponding result from the present simulation at $Re_a = 3300$ with $\delta/a = 4.92$ is $\delta^*/\theta^* = 1.14$.

Profiles of the mean velocity for boundary layers on flat plates have well-established functional forms in three distinct regions of the flow. In the innermost region, known as the viscous sublayer due to the predominant effects of viscosity, the mean velocity profile is given by the law of the wall,

$$\overline{U_z^+} = y^+, \quad y^+ \lesssim 5, \tag{4.10}$$

Reference	Re_a	δ/a	Re_δ	δ^*/δ	θ^*/δ	δ^*/θ^*
Berera [2004]	3280	3.2	10500	0.136	0.110	1.23
	3160	4.8	15200	0.140	0.118	1.19
	3460	6.6	22800	0.144	0.126	1.14
	3310	9.4	31100	0.146	0.132	1.11
	3260	11.5	37500	0.146	0.135	1.08
Farabee and Casarella [1991]	∞	0	29000	0.161	0.117	1.38
			53000	0.154	0.113	1.36
Kim et al. [1987]	∞	0	2710	0.171	0.106	1.62
Luxton et al. [1984]	140	41.6	5820	0.187	0.182	1.03
	325	39.1	12700	0.188	0.170	1.10
	455	26.9	12200	0.186	0.182	1.02
	620	26.7	16600	0.183	0.181	1.01
	785	26.0	20400	0.184	0.181	1.01
Moser et al. [1999]	∞	0	2730	0.171	0.105	1.63
			6560	0.154	0.106	1.46
			10500	0.145	0.104	1.40
Neves [1992]	311	9.23	2870	0.181	0.156	1.15
	674	4.20	2830	0.183	0.146	1.25
Schewe [1983]	∞	0	12500	0.153	0.110	1.39
Snarski and Lueptow [1995]	3642	5.04	18400	0.178	0.156	1.14
Willmarth et al. [1976]	736	37.5	27600	0.185	0.158	1.17
	1439	27.0	38900	0.146	0.139	1.05
	4330	16.0	69300	0.178	0.153	1.16
	9494	9.45	89700	0.203	0.161	1.27
	23100	4.64	107000	0.147	0.133	1.11
	74260	1.76	131000	0.157	0.135	1.17

Table 4.4: Integral thickness parameters for reference data.

where $\overline{U_z^+} = \overline{U_z}/u_\tau$ and $y^+ = yu_\tau/\nu$. In the outermost region, the mean velocity profile is given by the velocity-defect law,

$$(V_\infty - \overline{U_z})/u_\tau = f[y/\delta], \tag{4.11}$$

where f is an empirically determined function. In the intermediate region, the inner and outer scaling laws overlap, and the resulting velocity profile is given by the logarithmic law,

$$\overline{U_z^+} = 2.5\ln[y^+] + 5.1, \quad y^+ \gtrsim 70. \tag{4.12}$$

In the region $5 \lesssim y^+ \lesssim 70$, known as the buffer layer, the mean velocity profile varies smoothly between the law of the wall and the logarithmic law. The velocity profile departs gradually from the logarithmic law for $y/\delta \gtrsim 0.3$.

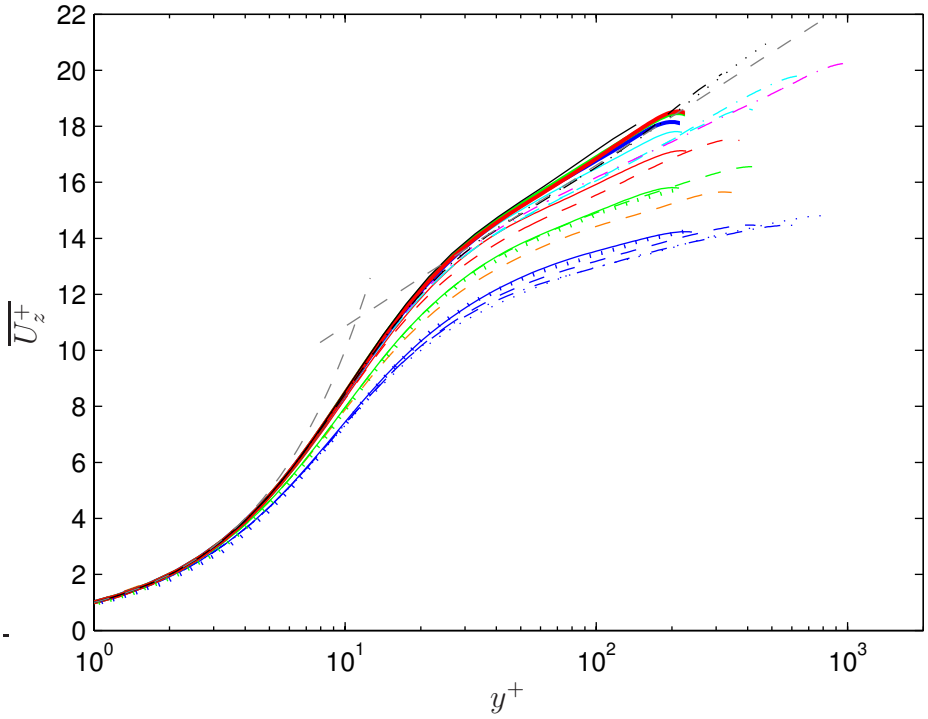

Figure 4.1: Mean velocity profiles in flat-plate wall units. Planar profile: – – law of the wall, $\overline{U_z^+} = y^+$, and log law, $\overline{U_z^+} = 2.5\ln[y^+] + 5.1$. Moser et al. [1999]: —— $\delta^+ \approx 149$; – – $\delta^+ \approx 326$; ····· $\delta^+ \approx 495$. Neves [1992]: ····· $a^+ = 21.7$, $\delta/a \approx 9.23$, $\delta^+ \approx 201$; ····· $a^+ = 42.8$, $\delta/a \approx 4.20$, $\delta^+ \approx 180$. Present simulations:

a^+	δ/a	δ^+	Line	a^+	δ/a	δ^+	Line	a^+	δ/a	δ^+	Line	a^+	δ/a	δ^+	Line
21.9	7.82	171	——	31.5	7.85	247	– –	74.3	3.63	270	– –	163	4.92	802	– · –
21.5	14.0	302	– –	42.7	3.74	159	——	146	1.18	173	——	287	0.574	165	——
21.5	19.1	411	– · –	40.8	7.74	315	– –	140	2.30	321	– –	564	0.313	177	——
21.0	27.6	580	·····	76.0	2.33	177	——	131	4.01	527	– · –	1130	0.157	177	——

Mean velocity profiles resulting from the present simulations (as listed in table 4.1) are shown in figure 4.1 with $\overline{U_z^+}$ plotted as a function of y^+. Also shown are the profiles given by the axisymmetric boundary layer simulations of Neves [1992] and the plane-channel simulations of Moser et al. [1999]. As may be expected, the law of the wall (equation 4.10) and the logarithmic law (equation 4.12) are a good fit to the plane-channel profiles. The present results for nearly-planar flows with $\delta/a \lesssim 0.5$ are consistent with the plane-channel results. The validity of the present results for large δ/a is indicated by the good agreement of the present profiles with those obtained by Neves [1992] for $a^+ \approx 22$ and 43 and $\delta/a \approx 8$ and 4, respectively.

The profiles of mean velocity appear to cluster into groups with similar a^+. A recognisable logarithmic region exists for all of the flows considered. As a^+ decreases, the slope of the profiles in the logarithmic region decreases below that of the planar case. Furthermore, the profiles depart from the planar profile at decreasing values of

y^+, so that the viscous sublayer is noticeably affected when a^+ is sufficiently small. The boundary layer thickness characterised by δ/a appears to have a secondary influence on the velocity profiles. For a given value of a^+, increasing δ/a shifts the velocity profile slightly downwards in the logarithmic region, while the corresponding increase in δ^+ causes the profile to extend to larger values of y^+ so that the maximum value of $\overline{U_z^+}$ increases.

Various laws of the wall have been proposed that incorporate the effects of transverse curvature [see, for example, Richmond, 1957, Rao, 1967, Denli and Landweber, 1979]. The approach of Rao [1967] is based on similar reasoning to that leading to the law of the wall for planar flow. In the axisymmetric viscous sublayer, inertial effects and Reynolds stresses may be neglected and, in the absence of a significant streamwise pressure-gradient, the Reynolds-average of the Navier-Stokes equation for the axial velocity component (equation 2.11c) reduces to

$$\frac{1}{r}\frac{\partial}{\partial r}\left(\nu r\frac{\partial\overline{U_z}}{\partial r}\right) = 0. \tag{4.13}$$

Integration outwards from the surface leads to

$$\nu r\frac{\partial\overline{U_z}}{\partial r} = a\frac{\tau_w}{\rho} = au_\tau^2 \quad \Rightarrow \quad \frac{\partial\overline{U_z^+}}{\partial r^+} = \frac{a^+}{r^+}. \tag{4.14}$$

Integration a second time yields the law of the wall for axisymmetric flow:

$$\overline{U_z^+} = a^+\ln[1 + y^+/a^+]. \tag{4.15}$$

Comparison with the relation for the planar viscous sublayer (equation 4.10) suggests that $a^+\ln[1+y^+/a^+]$ should replace y^+ as the wall variable for cylindrical boundary layers. The new wall variable has the expected property that the flat-plate variable y^+ is recovered as a^+ tends to infinity.

Velocity profiles in the axisymmetric wall units of Rao [1967] are shown for the present simulations in figure 4.2. The collapse is considerably better than that achieved with flat-plate wall units (figure 4.1). The law of the wall for axisymmetric flow,

$$\overline{U_z^+} = 2.5\ln\left[a^+\ln[1 + y^+/a^+]\right] + 5.1, \tag{4.16}$$

is a good fit to the simulated profiles inside the viscous sublayer. In the logarithmic region, all profiles appear to have a similar slope. The profiles collapse to a common curve except those with $a^+ \approx 20$. For these flows, the lack of collapse may indicate that the outer layer is not fully turbulent.

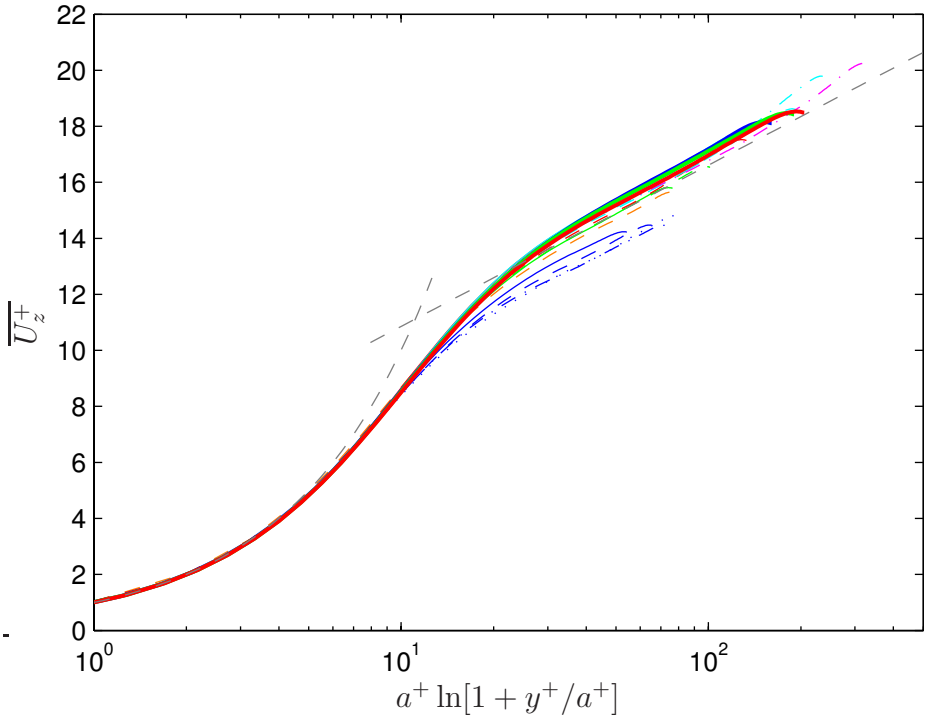

Figure 4.2: Mean velocity profiles in axisymmetric wall units [Rao, 1967]. Analytical profiles for axisymmetric flow: – – law of the wall, $\overline{U_z^+} = a^+ \ln[1 + y^+/a^+]$, and logarithmic law, $\overline{U_z^+} = 2.5 \ln\big[a^+ \ln[1 + y^+/a^+]\big] + 5.1$. Present simulations:

a^+	δ/a	δ^+	Line	a^+	δ/a	δ^+	Line	a^+	δ/a	δ^+	Line	a^+	δ/a	δ^+	Line
21.9	7.82	171	———	31.5	7.85	247	– –	74.3	3.63	270	– –	163	4.92	802	– · –
21.5	14.0	302	– –	42.7	3.74	159	———	146	1.18	173	———	287	0.574	165	———
21.5	19.1	411	– · –	40.8	7.74	315	– –	140	2.30	321	– –	564	0.313	177	———
21.0	27.6	580	·····	76.0	2.33	177	———	131	4.01	527	– · –	1130	0.157	177	———

It is interesting to note that the values of $\overline{U_z^+}$ at $y = \delta$ for the velocity profiles in figure 4.2 lie close to the profile corresponding to the logarithmic law for axisymmetric flow (equation 4.16). This observation is expressed mathematically as follows:

$$\overline{U_z^+}[y = \delta] \approx V_\infty/u_\tau \approx 2.5 \ln\big[a^+ \ln[1 + \delta/a]\big] + 5.1. \tag{4.17}$$

The above expression may, in principle, be used to obtain an estimate of the value of V_∞/u_τ for a given set of flow conditions. Substitution of $a^+ = Re_a u_\tau/V_\infty$ into the above expression and collection of all terms involving V_∞/u_τ into the left-hand-side yields

$$V_\infty/u_\tau + 2.5 \ln\left[V_\infty/u_\tau\right] \approx 2.5 \ln\big[Re_a \ln[1 + \delta/a]\big] + 5.1. \tag{4.18}$$

The slow variation of $\ln[V_\infty/u_\tau]$ relative to V_∞/u_τ suggests the more convenient empirical formula

$$V_\infty/u_\tau \approx A \ln\big[Re_a \ln[1 + \delta/a]\big] + B, \tag{4.19}$$

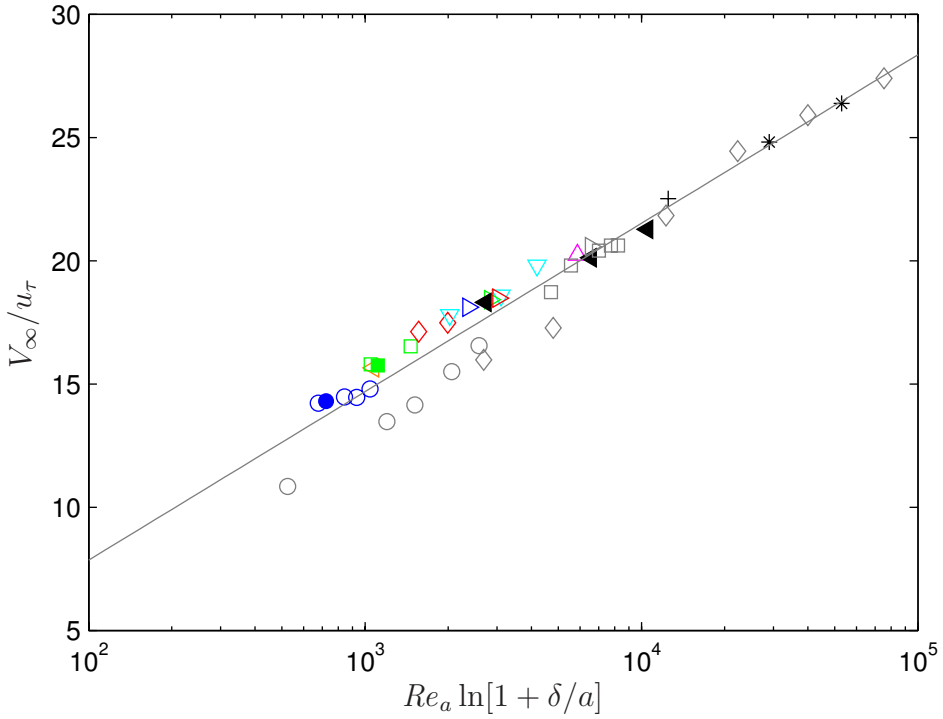

Figure 4.3: Ratio V_∞/u_τ as a function of both Re_a and δ/a for the present simulations and the reference data in table 4.2. Line of best fit: —— $V_\infty/u_\tau = 2.97 \ln\big[Re_a \ln[1+\delta/a]\big] - 5.82$. Values of Re_a for present simulations: ○ 311, ◁ 492, □ 674, ◇ 1300, ▽ 2600, △ 3300, ▷ 5200, ▷ 10400, ▷ 20800. Reference simulations: ● ■ Neves [1992], $Re_a = 311, 674$; ◀ Moser et al. [1999], $Re_a = \infty$. Cylinder experiments: □ Berera [2004], $Re_a \approx 3300$; ○ Luxton et al. [1984], $Re_a = 140$–785; ▷ Snarski and Lueptow [1995], $Re_a = 3642$; ♢ Willmarth et al. [1976], $Re_a = 736$–74260. Flat-plate measurements ($Re_a = \infty$): + Schewe [1983]; ✳ Farabee and Casarella [1991].

where A and B are constants. The values of V_∞/u_τ for the present simulations and the reference data in table 4.2 are shown in figure 4.3 as a function of $Re_a \ln[1+\delta/a]$, which reduces to Re_δ in the limit of $\delta/a \to 0$. The line-of-best-fit through the data (in a least-squares sense) is equivalent to equation 4.19 with the constants $A = 2.97$ and $B = -5.82$. With these constants, equation 4.19 may be used to estimate V_∞/u_τ, along with other wall-parameters such as $a^+ = Re_a u_\tau/V_\infty$ and the skin friction coefficient $C_f = 2(u_\tau/V_\infty)^2$, for given values of the outer-flow parameters Re_a and δ/a.

The data points in figure 4.3 corresponding to experiments at low values of Re_a, including the measurements of Luxton et al. [1984] and some of the measurements of Willmarth et al. [1976], show a slightly different trend from that of the present simulation results. The slight discrepancy may be due to errors in the measured values of the wall-shear-stress (and hence u_τ) on the very thin cylinders used in the

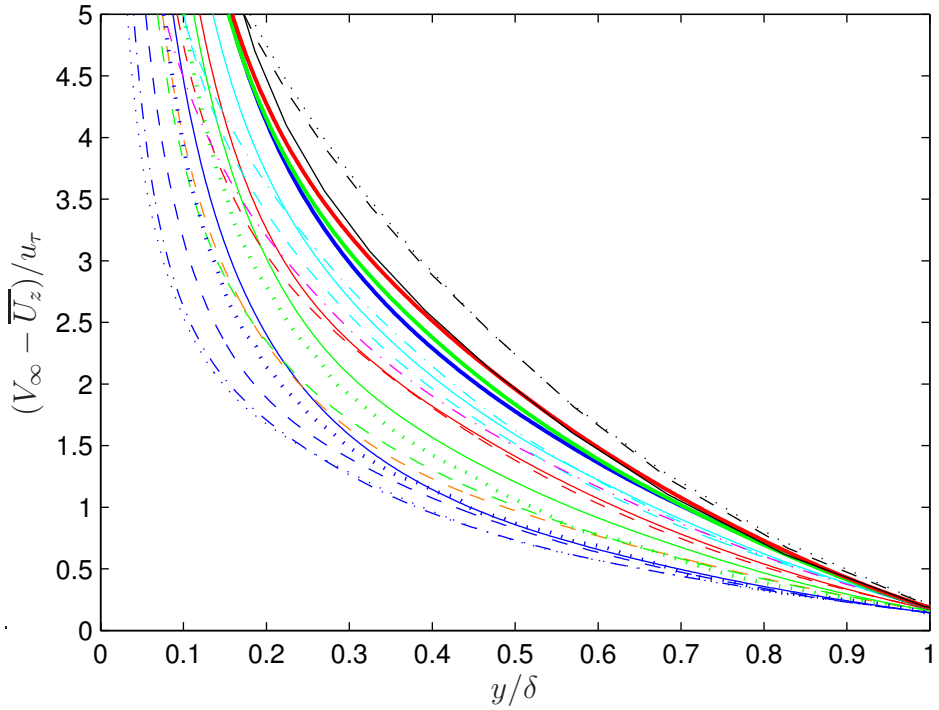

Figure 4.4: Velocity-defect profiles for cylinder and plane-channel simulations. Moser et al. [1999]: —— $\delta^+ \approx 149$; – – $\delta^+ \approx 326$; ····· $\delta^+ \approx 495$. Neves [1992]: ····· $\delta/a \approx 9.23$, $\delta^+ \approx 201$; ····· $\delta/a \approx 4.20$, $\delta^+ \approx 180$. Present data:

a^+	δ/a	δ^+	Line	a^+	δ/a	δ^+	Line	a^+	δ/a	δ^+	Line	a^+	δ/a	δ^+	Line
21.9	7.82	171	——	31.5	7.85	247	– –	74.3	3.63	270	– –	163	4.92	802	– · –
21.5	14.0	302	– –	42.7	3.74	159	——	146	1.18	173	——	287	0.574	165	——
21.5	19.1	411	– · –	40.8	7.74	315	– –	140	2.30	321	– –	564	0.313	177	——
21.0	27.6	580	·····	76.0	2.33	177	——	131	4.01	527	– · –	1130	0.157	177	——

experiments. This explanation is supported by the comments of Willmarth et al. [1976, p. 47], who suggest that the accuracy of their wall-shear-stress measurements is probably only ±10–15%. The wall-shear-stress data reported by Luxton et al. [1984] have a similar level of accuracy, because their data are estimates based on the measurements of Willmarth et al. [1976].

To examine the effects of transverse curvature on the outer part of the boundary layer, velocity profiles in the form suggested by the velocity-defect law (equation 4.11), that is $(V_\infty - \overline{U_z})/u_\tau$ as a function of y/δ, are shown in figure 4.4. The data included in the figure are taken from the present simulations, the cylinder simulations of Neves [1992] and the plane-channel simulations of Moser et al. [1999]. The results for plane-channel flow indicate that the velocity-defect profiles are nearly independent of δ^+ when the value of δ^+ is greater than approximately 326. For small values of δ/a, the profiles for cylinders are similar to the plane-channel profiles. As δ/a increases, the slope of the cylinder profiles becomes less negative near $y/\delta = 1$,

where the value of the velocity-defect is $0.01V_\infty/u_\tau$ by definition. The trend is consistent with the experimental observations and dimensional analysis of Willmarth et al. [1976]. Denli and Landweber [1979] formulate a velocity-defect law for thick, axisymmetric boundary layers, based on the idea that the outer flow is similar to an axisymmetric wake. The empirical constants in their formula are tuned to fit a limited number of experimental measurements, but the resulting velocity-defect law does not provide a reliable fit to the present data. It appears that further work may be necessary before a general scaling relation is devised for the mean velocity profile in the outer part of axisymmetric boundary layers.

4.2 Reynolds Shear-Stress

Reynolds shear-stresses in wall coordinates for the present simulations are shown in conjunction with reference data in figure 4.5. The current calculations are in close agreement with the corresponding simulations of Neves [1992]. The present profile for $a^+ = 1130$ and $\delta^+ = 177$ ($\delta/a = 0.157$) is placed, as expected, between the plane-channel profiles of Moser et al. [1999] for $\delta^+ = 149$ and 326.

The location of the peak Reynolds shear-stress moves outwards from the wall as the peak value increases. The peak location moves from $y^+ \approx 20$ to $y^+ \approx 40$ as the peak value varies from $0.35u_\tau^2$ to $0.85u_\tau^2$. For flows with large a^+, the peak value of the Reynolds shear-stress appears to increase towards u_τ^2 as δ^+ increases. For example, in the plane-channel flows ($a^+ = \infty$), the peak values are, respectively, $-\overline{u_r u_z}/u_\tau^2 \approx 0.72, 0.84, 0.87$ when $\delta^+ \approx 149, 326, 495$. On the other hand, when a^+ is small (about 40 or less), the peak value is little affected by δ^+.

For flow over cylinders at a given δ^+, the peak value of the Reynolds shear-stress increases towards the plane-channel result as a^+ is increased. For example, when $\delta^+ \approx 170$, the peak value increases from $\sim 0.35u_\tau^2$ to the plane-channel value $\sim 0.75u_\tau^2$ as a^+ varies from 22 to ∞.

The shear-stress data are re-plotted in figure 4.6a with the wall-normal distance scaled as a proportion of h, which denotes the radial width $(b-a)$ of the cylindrical domain or the plane-channel half-width. The plane-channel profiles collapse to a common line in the outer portion of the domain. The profiles for the present calculations depart further from the planar case as δ/a (or b/a) increases. The Reynolds shear-stress is substantially reduced in the outer part of the layer when δ/a is large.

Outside the viscous sublayer, the Reynolds shear-stress makes the dominant contribution to the total shear-stress at the statistically-steady state. The total

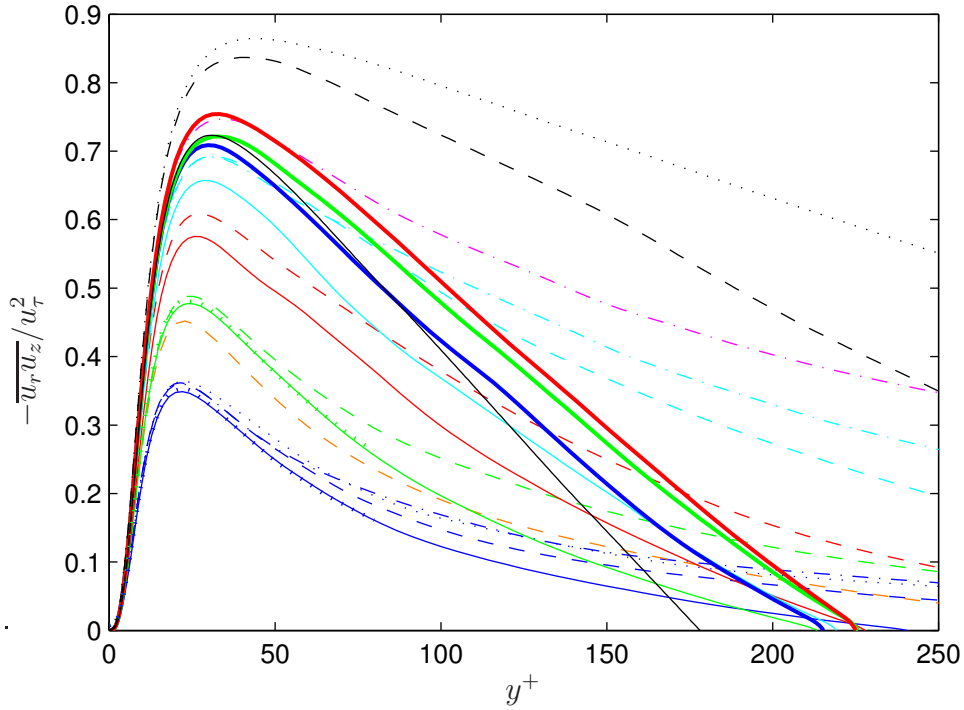

Figure 4.5: Reynolds shear-stress in wall units. Line-styles for present simulations are shown in the legend below. Moser et al. [1999]: —— $\delta^+ \approx 149$; – – $\delta^+ \approx 326$; ····· $\delta^+ \approx 495$. Neves [1992]: ····· $a^+ = 21.7$, $\delta^+ \approx 201$; ····· $a^+ = 42.8$, $\delta^+ \approx 180$.

a^+	δ/a	δ^+	Line	a^+	δ/a	δ^+	Line	a^+	δ/a	δ^+	Line	a^+	δ/a	δ^+	Line
21.9	7.82	171	——	31.5	7.85	247	– –	74.3	3.63	270	– –	163	4.92	802	– · –
21.5	14.0	302	– –	42.7	3.74	159	——	146	1.18	173	——	287	0.574	165	——
21.5	19.1	411	– · –	40.8	7.74	315	– –	140	2.30	321	– –	564	0.313	177	——
21.0	27.6	580	·····	76.0	2.33	177	——	131	4.01	527	– · –	1130	0.157	177	——

shear-stress has the analytical form given by equation 3.9, which may be rewritten as

$$\overline{\tau}|_{\text{cyl}} \approx \rho u_\tau^2 \left(\frac{a}{r}\right)\left(\frac{b+r}{b+a}\right)\left(1-\frac{y}{h}\right) \tag{4.20}$$

since the Reynolds stress at the outer boundary is generally negligible. The corresponding expression for a plane-channel is

$$\overline{\tau}|_{\text{plane}} = \rho u_\tau^2 \left(1-\frac{y}{h}\right). \tag{4.21}$$

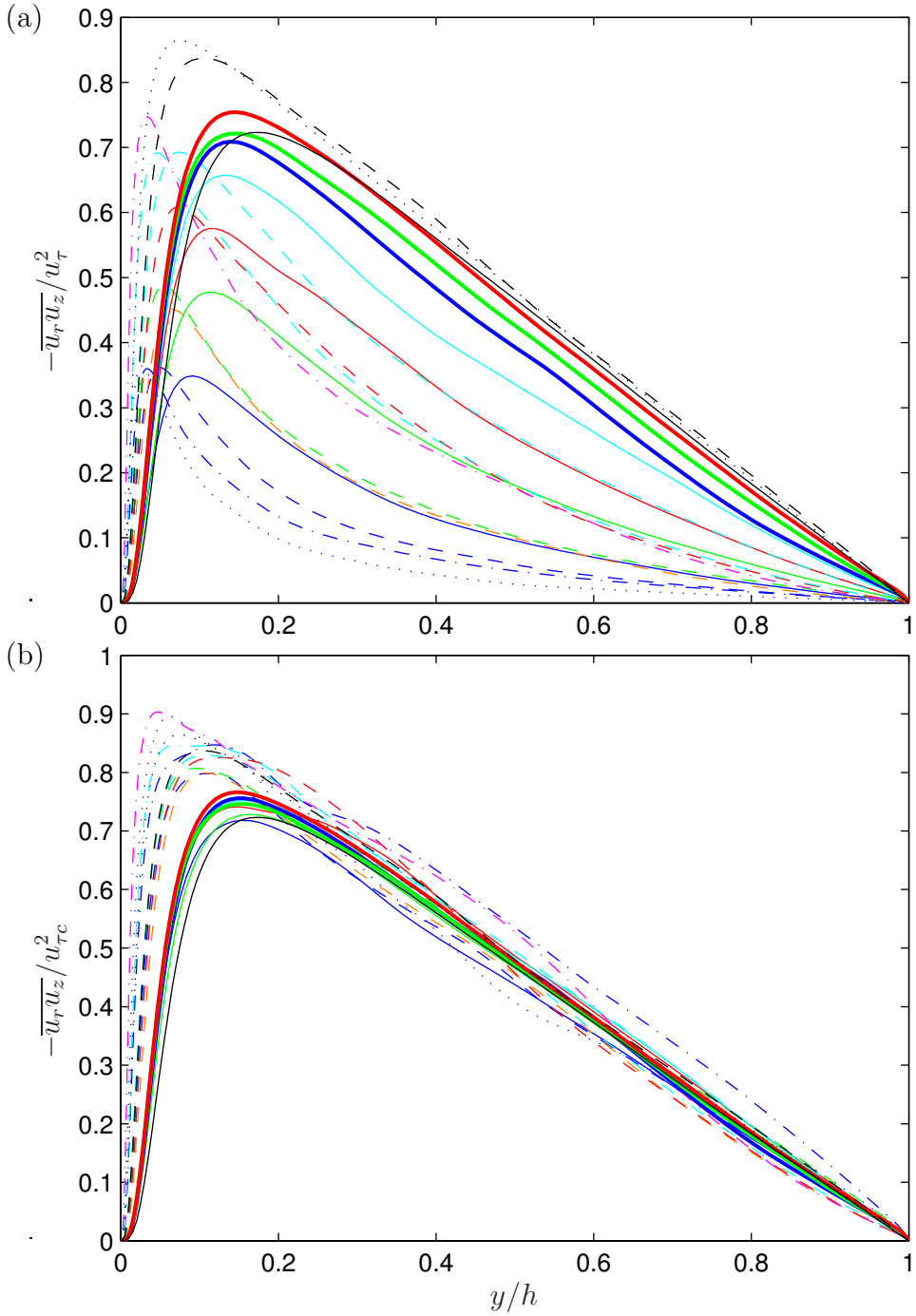

Figure 4.6: Reynolds shear-stress as functions of y/h scaled with (a) u_τ and (b) $u_{\tau c}$. Moser et al. [1999]: —— $\delta^+ \approx 149$; – – $\delta^+ \approx 326$; ····· $\delta^+ \approx 495$. Present data:

a^+	δ/a	δ^+	Line	a^+	δ/a	δ^+	Line	a^+	δ/a	δ^+	Line	a^+	δ/a	δ^+	Line
21.9	7.82	171	——	31.5	7.85	247	– –	74.3	3.63	270	– –	163	4.92	802	– · –
21.5	14.0	302	– –	42.7	3.74	159	——	146	1.18	173	——	287	0.574	165	——
21.5	19.1	411	– · –	40.8	7.74	315	– –	140	2.30	321	– –	564	0.313	177	——
21.0	27.6	580	·····	76.0	2.33	177	——	131	4.01	527	– · –	1130	0.157	177	——

Comparison of these two expressions led Neves [1992] to propose a new velocity-scale for transversely curved boundary layers, which in the present notation is given by

$$\begin{aligned} u_{\tau c}^2[r] &= u_\tau^2 \left(\frac{a}{r}\right)\left(\frac{b+r}{b+a}\right), \\ u_{\tau c}^2[y] &= u_\tau^2 \left(\frac{a}{a+y}\right)\left(\frac{b+a+y}{b+a}\right). \end{aligned} \tag{4.22}$$

The value of $u_{\tau c}$ decreases from u_τ at the cylinder wall to $u_\tau\sqrt{2/(b/a+1)}$ at $r=b$. In the limit as b/a approaches unity ($\delta/a \to 0$), $u_{\tau c}$ is equivalent to the planar velocity-scale u_τ throughout the boundary layer.

The cylinder velocity-scale $u_{\tau c}$ depends explicitly on the ratio b/a, as is made clear when equation 4.22 is written in the form

$$u_{\tau c}^2[y/h, b/a] = u_\tau^2 \left(\frac{1}{1+(y/h)(b/a-1)}\right)\left(\frac{b/a+1+(y/h)(b/a-1)}{b/a+1}\right). \tag{4.23}$$

Near the cylinder wall, the definition of $u_{\tau c}$ reduces to

$$u_{\tau c}^2[y] \approx u_\tau^2 \left(\frac{a}{a+y}\right) = u_\tau^2 \left(\frac{a^+}{a^+ + y^+}\right), \quad y \ll b+a. \tag{4.24}$$

Thus, the near-wall values of $u_{\tau c}$ differ significantly from u_τ when a^+ is small.

Reynolds stresses normalised by $u_{\tau c}$ for the present simulations and the plane-channel calculations of Moser et al. [1999] are shown in figure 4.6b. As may be expected from the definition of $u_{\tau c}$, the profiles collapse to a common line away from the wall. In fact, the profiles for flows with similar δ^+ collapse throughout the boundary layer, independently of transverse curvature.

4.3 Turbulence Intensities

Root-mean-square (RMS) values of the velocity fluctuations for the current simulations are shown in figure 4.7 along with suitable reference data. The present calculations are in good agreement with the simulations of Neves [1992] and consistent with the plane-channel simulations of Moser et al. [1999]. The present data for $Re_a = 311$ and 674 are in good agreement, near the wall, with the experimental results of Luxton et al. [1984]. Further from the wall, the experimental data depart from the calculated profiles due to the differing values of δ/a.

The profiles of RMS velocity fluctuations increase to maximum values $u'_{\max}$ at short distances $y^+_{\max}$ from the wall. In a given flow, the maxima $u'_{\max,z}$, $u'_{\max,r}$ and

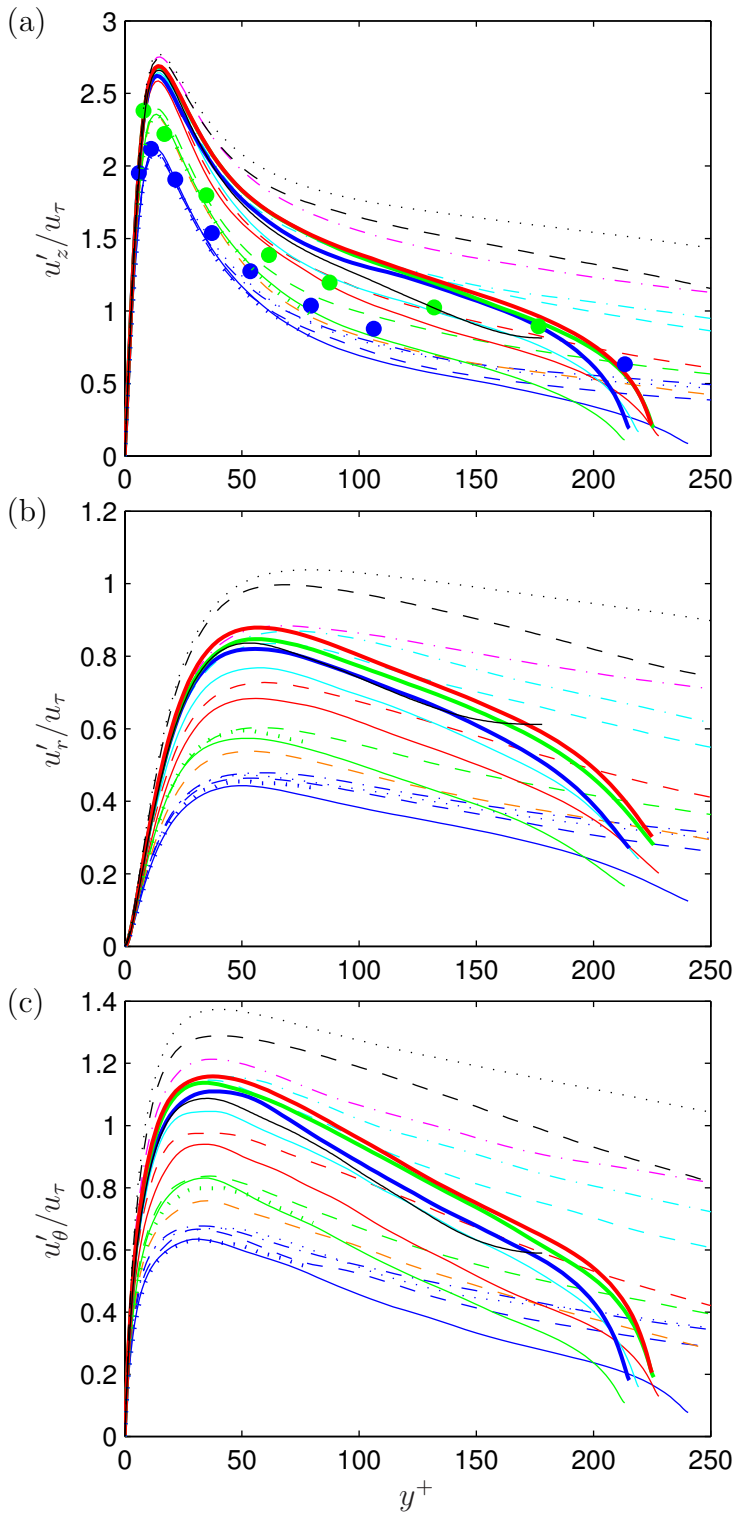

a^+	δ/a	δ^+	Line
21.9	7.82	171	
21.5	14.0	302	
21.5	19.1	411	
21.0	27.6	580	
31.5	7.85	247	
42.7	3.74	159	
40.8	7.74	315	
76.0	2.33	177	
74.3	3.63	270	
146	1.18	173	
140	2.30	321	
131	4.01	527	
163	4.92	802	
287	0.574	165	
564	0.313	177	
1130	0.157	177	

Figure 4.7: RMS velocity fluctuations in wall units. Velocity components: (a) axial, (b) radial, (c) azimuthal. Line-styles for present simulations are defined in the legend. Moser et al. [1999]: —— $\delta^+ \approx 149$; – – $\delta^+ \approx 326$; ····· $\delta^+ \approx 495$. Neves [1992]: ····· $a^+ = 21.7$, $\delta^+ \approx 201$; ····· $a^+ = 42.8$, $\delta^+ \approx 180$. Luxton et al. [1984]: ● $a^+ = 24.1$, $\delta^+ = 943$; ● $a^+ = 40.0$, $\delta^+ = 1070$.

$u'_{\max,\theta}$ for the three velocity components are typically different from one another, as are the corresponding wall-normal distances $y^+_{\max,z}$, $y^+_{\max,r}$ and $y^+_{\max,\theta}$. For each vector component, the distance $y^+_{\max}$ increases as the corresponding $u'_{\max}$ increases. Over the range of flows considered in figure 4.7, the maximum RMS velocity values and the corresponding locations vary as follows: $u'_{\max,z}/u_\tau \approx 2.1 \to 2.8$, $y^+_{\max,z} \approx 13 \to 15$; $u'_{\max,r}/u_\tau \approx 0.4 \to 1.0$, $y^+_{\max,r} \approx 50 \to 80$; $u'_{\max,\theta}/u_\tau \approx 0.6 \to 1.4$, $y^+_{\max,\theta} \approx 30 \to 40$.

The results for the plane-channel simulations of Moser et al. [1999] suggest that the peak turbulence intensity increases towards a limiting value as δ^+ increases. The limiting values suggested by the simulation results are $u'_z/u_\tau \lesssim 3.0$, $u'_r/u_\tau \lesssim 1.1$ and $u'_\theta/u_\tau \lesssim 1.5$. The results of the present cylinder simulations suggest that the peak value of the turbulence intensity becomes less sensitive to changes in δ^+ as a^+ decreases.

For flow over cylinders, the peak value of each component of the turbulence intensity approaches the plane-channel result for a given δ^+ as a^+ is increased. For example, when $\delta^+ \approx 170$ and a^+ varies from 22 to ∞, the approximate peak values of u'_z, u'_r, u'_θ (normalised by u_τ) respectively increase from $2.1, 0.45, 0.65$ to the plane-channel values $2.7, 0.85, 1.1$. The relative variation of these peak values, that is the change relative to the final value, is larger for the radial and azimuthal components than for the more energetic axial component.

The turbulence intensities shown in figure 4.8 are normalised by the velocity-scale $u_{\tau c}$ defined by equation 4.22. When plotted as functions of y/h, the profiles for each velocity component collapse to a common curve away from the wall. For the axial velocity component (figure 4.8a), but not the radial or azimuthal components, the profiles for flows with similar δ^+ collapse throughout the boundary layer, independently of transverse curvature. The present simulations differ from those of Moser et al. [1999] near $y = h$. The plane-channel statistics are symmetrical about the channel half-width, whereas the present turbulence intensities decay rapidly near the outer limit of the computational domain. As intended in the design of the present computational procedure, the turbulence intensities, including the radial component, are non-zero at the outer boundary.

Profiles of the RMS axial (streamwise) velocity fluctuations normalised by $u_{\tau c}$ have approximately the same peak value (2.7–2.8) for all of the flows shown in figure 4.8a. In fact, the same profiles plotted as functions of y^+ (not shown) collapse quite well for $y^+ \lesssim 30$, which includes the peak at $y^+ \approx 15$. Consequently, the intensities

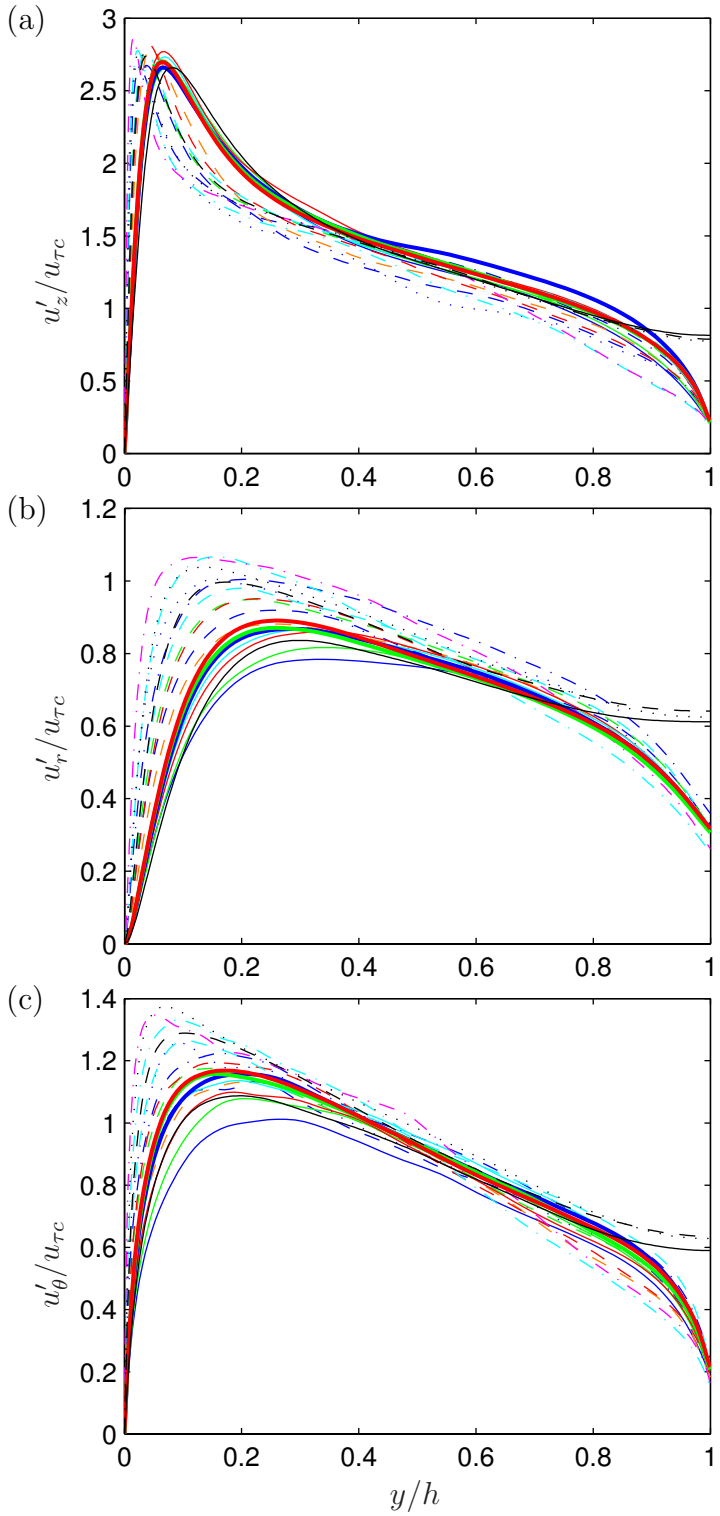

a^+	δ/a	δ^+	Line
21.9	7.82	171	
21.5	14.0	302	
21.5	19.1	411	
21.0	27.6	580	
31.5	7.85	247	
42.7	3.74	159	
40.8	7.74	315	
76.0	2.33	177	
74.3	3.63	270	
146	1.18	173	
140	2.30	321	
131	4.01	527	
163	4.92	802	
287	0.574	165	
564	0.313	177	
1130	0.157	177	

Figure 4.8: RMS velocity fluctuations as functions of y/h scaled with $u_{\tau c}$. Velocity components: (a) axial, (b) radial, (c) azimuthal. Line-styles for present simulations are defined in the legend. Moser et al. [1999]: —— $\delta^+ \approx 149$; – – $\delta^+ \approx 326$; ····· $\delta^+ \approx 495$.

of the near-wall axial velocity fluctuations for cylindrical and planar boundary layers are related by the following expression:

$$\frac{\overline{u_z^2}|_{\text{cyl}}}{\overline{u_z^2}|_{\text{plane}}} \approx \frac{u_{\tau c}^2}{u_\tau^2} \approx \frac{2\pi a^+}{2\pi(a^+ + y^+)}, \quad y^+ \lesssim 30 \ll (b^+ + a^+). \tag{4.25}$$

The mean-square value of the axial (streamwise) velocity fluctuations at a small distance y^+ from a cylinder is reduced, relative to the corresponding value for planar flow, as the spanwise distance around the cylinder at radius $a^+ + y^+$ increases relative to the cylinder circumference. The mean-square values of the radial (wall-normal) and azimuthal (spanwise) velocity fluctuations are also reduced in cylindrical boundary layers compared with planar flow, but not by the same proportion as the axial (streamwise) fluctuations.

4.4 Turbulence Kinetic Energy Budget

For flow in cylindrical geometry, the turbulence kinetic energy per unit volume is defined as

$$\overline{q} = \frac{1}{2}\rho\left(\overline{u_r^2} + \overline{u_\theta^2} + \overline{u_z^2}\right). \tag{4.26}$$

The transport equation for the turbulence kinetic energy, as derived by Neves [1992, appendix A] for flow with azimuthal and axial homogeneity, is expressed in the present notation as follows:

$$
\begin{aligned}
&\frac{1}{\rho}\frac{\partial \overline{q}}{\partial t} = && \leftarrow \text{total rate of change}\\
&-\overline{u_z u_r}\,\frac{\partial \overline{U_z}}{\partial r} && \leftarrow \text{production rate}\\
&-\frac{1}{\rho}\left[\overline{u_r\frac{\partial p}{\partial r}} + \overline{\frac{u_\theta}{r}\frac{\partial p}{\partial \theta}} + \overline{u_z\frac{\partial p}{\partial z}}\right] && \leftarrow \text{velocity pressure-gradient term}\\
&-\frac{1}{\rho r}\frac{\partial}{\partial r}\left(r\,\overline{q u_r}\right) && \leftarrow \text{turbulent transport rate}\\
&+\frac{\nu}{\rho r}\frac{\partial}{\partial r}\left(r\frac{\partial \overline{q}}{\partial r}\right) && \leftarrow \text{viscous diffusion rate}\\
&-\nu\Bigg\{\left[\overline{\left(\frac{\partial u_r}{\partial r}\right)^2} + \overline{\left(\frac{\partial u_\theta}{\partial r}\right)^2} + \overline{\left(\frac{\partial u_z}{\partial r}\right)^2}\right]\\
&\quad + \frac{1}{r^2}\left[\overline{\left(\frac{\partial u_r}{\partial \theta} - u_\theta\right)^2} + \overline{\left(\frac{\partial u_\theta}{\partial \theta} + u_r\right)^2} + \overline{\left(\frac{\partial u_z}{\partial \theta}\right)^2}\right]\\
&\quad + \left[\overline{\left(\frac{\partial u_r}{\partial z}\right)^2} + \overline{\left(\frac{\partial u_\theta}{\partial z}\right)^2} + \overline{\left(\frac{\partial u_z}{\partial z}\right)^2}\right]\Bigg\}. && \leftarrow \text{viscous dissipation rate}
\end{aligned}
\tag{4.27}
$$

Profiles of the terms on the right-hand-side of equation 4.27 for the present calculations* are shown, as functions of y^+ and normalised by τ_w and u_τ^2/ν, in figures 4.9, 4.10 and 4.11a. The results of Neves [1992] are shown for reference, and they agree well with the present results for flows with $a^+ \approx 22$ and 43. The plane-channel results calculated by Moser et al. [1999] are also shown to allow the effects of transverse curvature to be distinguished from any dependence on the Reynolds number δ^+.

At the near-wall positions shown in the figures ($y^+ \leq 80$), the profiles for planar flow tend towards a common curve as δ^+ increases. Similarly, the near-wall profiles for axisymmetric flows with a given value of a^+ tend towards a common curve as δ^+ increases.

As may be expected, the profiles for axisymmetric flows with large a^+ and small δ/a are similar to the plane-channel results. For example, there is good agreement between the plane-channel results for $\delta^+ = 149$ and the present results for $\delta^+ = 177$

*Flow cases $Re_a = 492$, $b/a = 12$ and $Re_a = 1300$, $b/a = 6$ are omitted because the format of their data-files, created using an early version of the simulation code, is not compatible with the post-processing code used to calculate the turbulence kinetic energy balance.

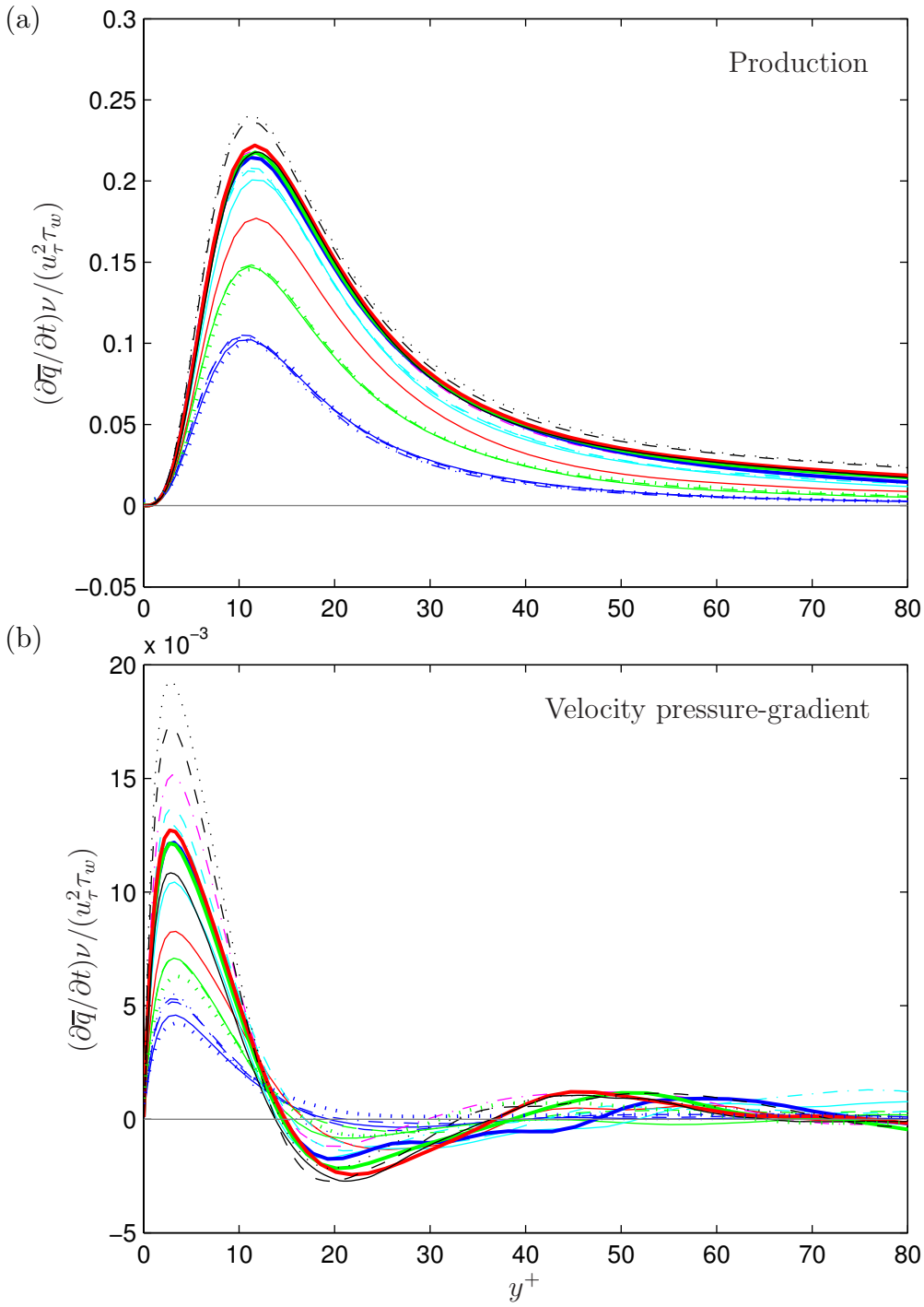

Figure 4.9: Terms of turbulence kinetic energy budget: (a) production and (b) velocity pressure-gradient. Moser et al. [1999]: —— $\delta^+ \approx 149$; – – $\delta^+ \approx 326$; ····· $\delta^+ \approx 495$. Neves [1992]: ····· $a^+ = 21.7$, $\delta^+ \approx 201$; ····· $a^+ = 42.8$, $\delta^+ \approx 180$.

a^+	δ/a	δ^+	Line	a^+	δ/a	δ^+	Line	a^+	δ/a	δ^+	Line	a^+	δ/a	δ^+	Line
21.9	7.82	171	——	-	-	-	-	-	-	-	-	163	4.92	802	- · -
21.5	14.0	302	– –	42.7	3.74	159	——	146	1.18	173	——	287	0.574	165	——
21.5	19.1	411	- · -	40.8	7.74	315	– –	140	2.30	321	– –	564	0.313	177	——
21.0	27.6	580	·····	76.0	2.33	177	——	131	4.01	527	- · -	1130	0.157	177	——

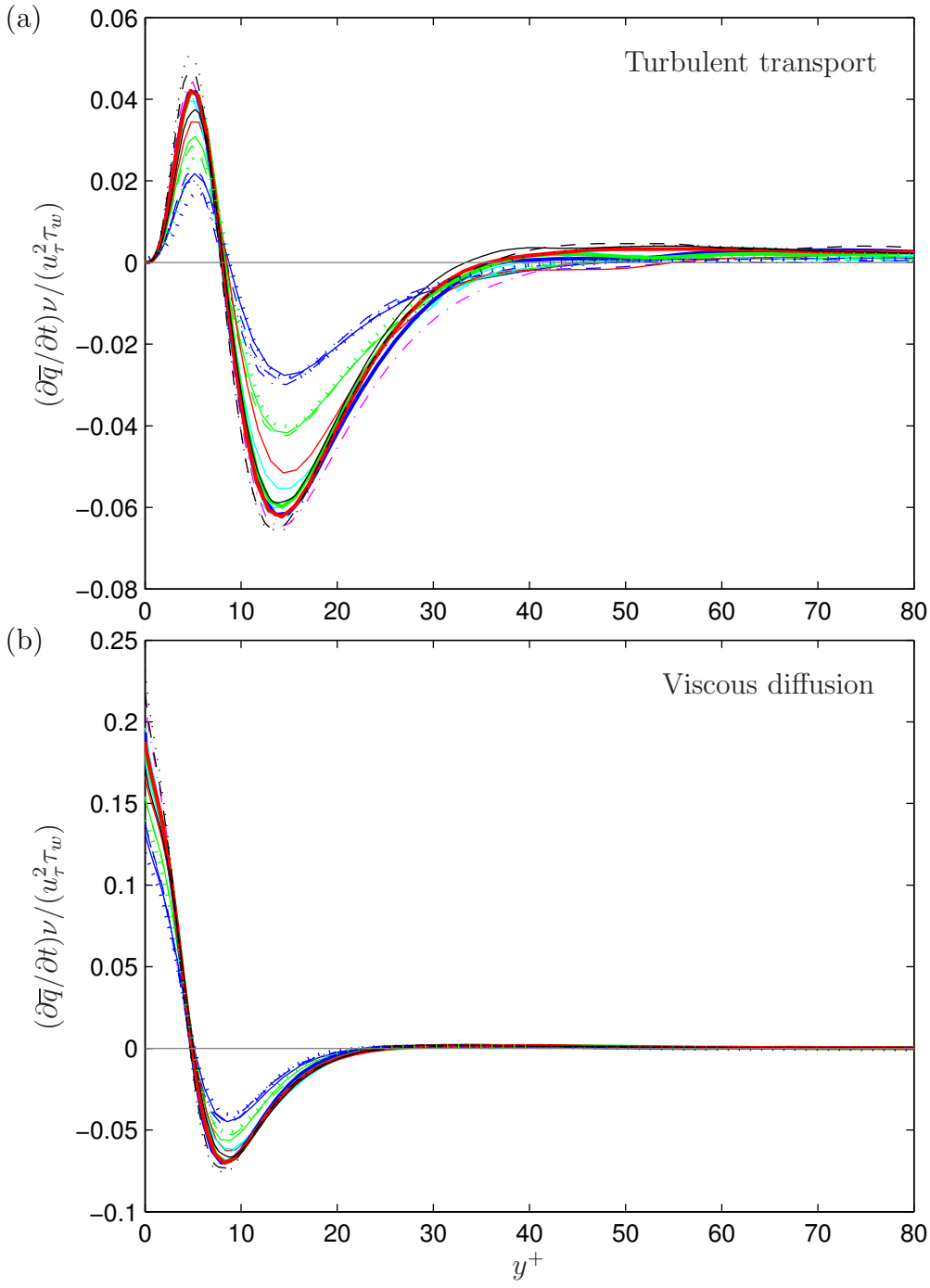

Figure 4.10: Terms of turbulence kinetic energy budget: (a) turbulent transport and (b) viscous diffusion. Moser et al. [1999]: —— $\delta^+ \approx 149$; – – $\delta^+ \approx 326$; ····· $\delta^+ \approx 495$. Neves [1992]: ····· $a^+ = 21.7$, $\delta^+ \approx 201$; ····· $a^+ = 42.8$, $\delta^+ \approx 180$.

a^+	δ/a	δ^+	Line	a^+	δ/a	δ^+	Line	a^+	δ/a	δ^+	Line	a^+	δ/a	δ^+	Line
21.9	7.82	171	——	-	-	-	-	-	-	-	-	163	4.92	802	- · –
21.5	14.0	302	– –	42.7	3.74	159	——	146	1.18	173	——	287	0.574	165	——
21.5	19.1	411	- · –	40.8	7.74	315	– –	140	2.30	321	– –	564	0.313	177	——
21.0	27.6	580	·····	76.0	2.33	177	——	131	4.01	527	- · –	1130	0.157	177	——

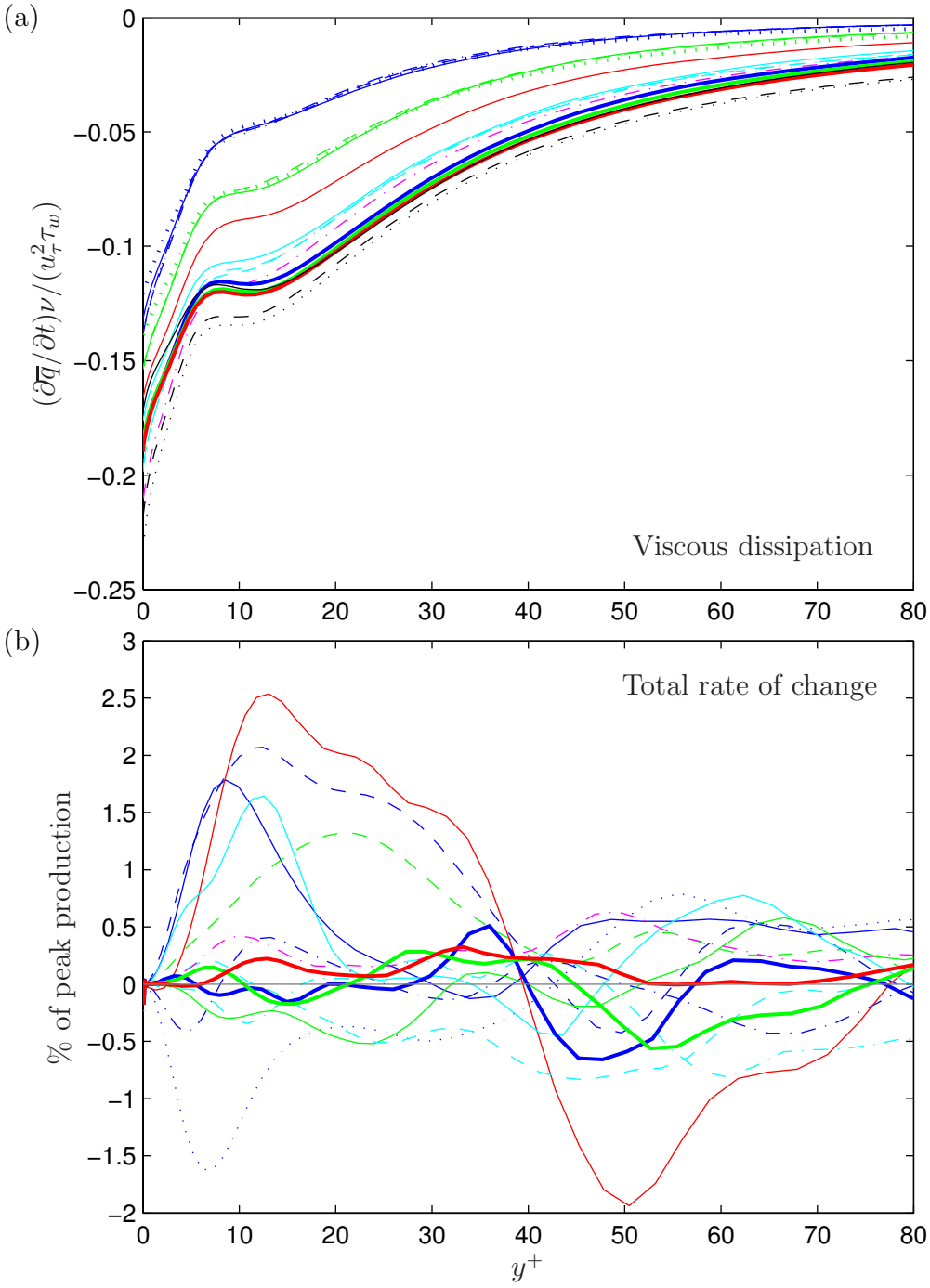

Figure 4.11: Terms of turbulence kinetic energy budget: (a) viscous dissipation and (b) total rate of change (present data only). Moser et al. [1999]: —— $\delta^+ \approx 149$; – – $\delta^+ \approx 326$; ····· $\delta^+ \approx 495$. Neves [1992]: ····· $a^+ = 21.7$, $\delta^+ \approx 201$; ····· $a^+ = 42.8$, $\delta^+ \approx 180$.

a^+	δ/a	δ^+	Line	a^+	δ/a	δ^+	Line	a^+	δ/a	δ^+	Line	a^+	δ/a	δ^+	Line
21.9	7.82	171	——	-	-	-	-	-	-	-	-	163	4.92	802	- · -
21.5	14.0	302	– –	42.7	3.74	159	——	146	1.18	173	——	287	0.574	165	——
21.5	19.1	411	- · -	40.8	7.74	315	– –	140	2.30	321	– –	564	0.313	177	——
21.0	27.6	580	·····	76.0	2.33	177	——	131	4.01	527	- · -	1130	0.157	177	——

with $a^+ = 1130$ and $\delta/a = 0.157$. The magnitude of the profiles for the axisymmetric flows decreases as a^+ decreases and δ/a increases. This trend is also found in the profiles of Reynolds shear-stress and turbulence intensity (plotted in wall units), as discussed earlier in sections 4.2 and 4.3. However, unlike those other quantities, the profiles for each term of the turbulence kinetic energy budget do not collapse with normalisation based on the velocity-scale $u_{\tau c}$ defined by equation 4.22.

All of the displayed results are obtained from simulations that are considered to have reached a statistically-steady state, for which the total-rate-of-change term of equation 4.27 is expected to be zero. The value of this term, calculated by addition of the terms on the right-hand-side of the equation, is shown as a function of y^+ in figure 4.11b. For all of the present simulations, the absolute value of the total-rate-of-change term is smaller than 2.5% of the peak value of the production-rate term (figure 4.9a). The non-zero value of the total-rate-of-change term indicates that the simulation results do not correspond exactly to a statistically-steady state. The statistical steadiness of the simulation results is, however, considered to be adequate for present purposes, as discussed previously in section 3.5.

4.5 Higher-Order Moments

The axisymmetric boundary layer experiments of Luxton et al. [1984] at low cylinder Reynolds numbers reveal velocity fluctuations similar in character to those shown in figure 4.12. The signals exhibit negative spikes that are large and infrequent compared with positive fluctuations about the mean. The negative spikes indicate the passage past the measurement point of low-speed fluid originating from regions close to the cylinder surface. The increased intensity of these so-called "low-speed spots" in relation to planar boundary layers led Luxton et al. to surmise that the turbulence generation mechanism in boundary layers with large δ/a is enhanced by the motion of large-scale turbulence structures across the cylinder. Such cross-flows become less probable as δ/a decreases and they can never occur in a planar layer.

The intensity and frequency of low-speed spots can be determined by examination of the probability density function (PDF). Rather than attempting the direct comparison of PDFs for different flows, it is expedient instead to compare skewness and flatness statistics. These are shown for each velocity component of the present simulations and a selection of reference flows in figures 4.13 and 4.14. The skewness and flatness profiles given by the present simulations are in reasonable agreement with the experiments of Luxton et al. [1984] and the simulations of Neves [1992].

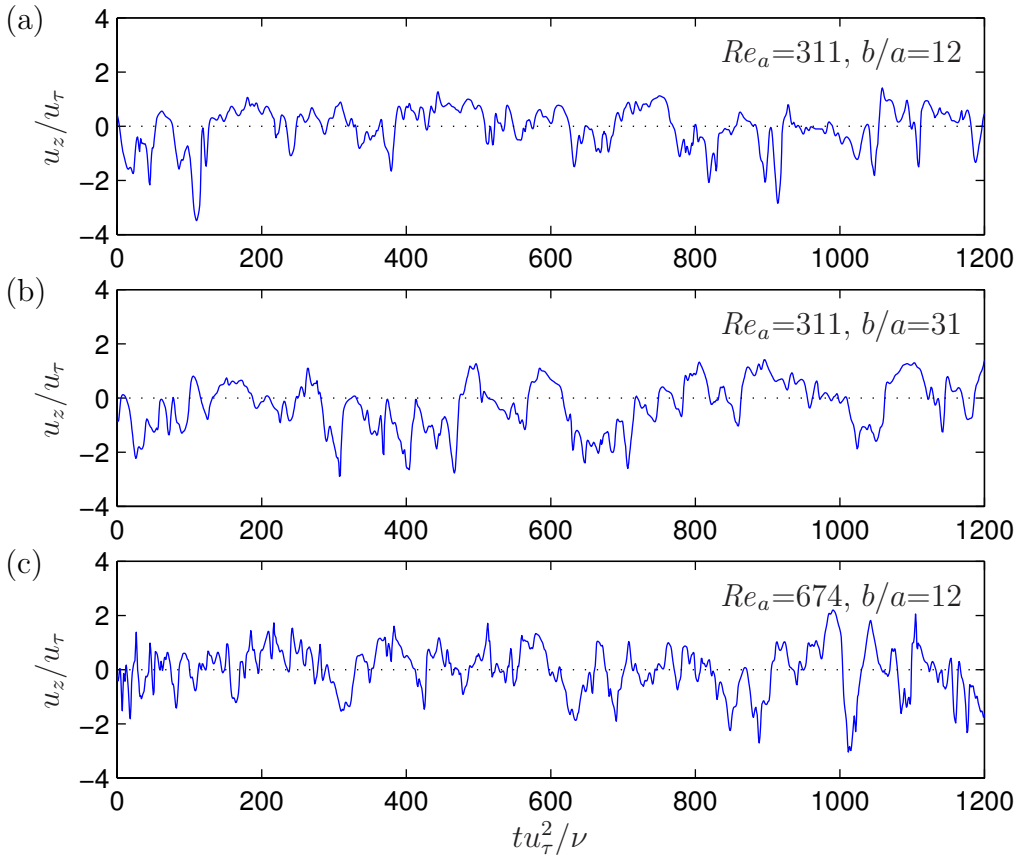

Figure 4.12: Example time-series of axial velocity fluctuations at $y^+ = 100$ from three of the present simulations.

The present results for nearly-planar flow with $\delta/a \lesssim 0.5$ and $\delta^+ \approx 170$ are, as expected, similar to the plane-channel result of Moser et al. [1999] for $\delta^+ \approx 149$.

The PDF of the velocity fluctuations has a mean of zero, by definition. The normal distribution has skewness of 0 and flatness of 3. Negative skewness corresponds to a PDF that has a heavier tail on the negative than on the positive side, indicating the increased likelihood of large negative velocity fluctuations compared with positive fluctuations of the same magnitude. Flatness greater than 3 corresponds to a PDF that has a sharper peak and heavier tails than a normal distribution with the same variance, indicating that both very small fluctuations and very large fluctuations about the mean are more common than they are in normally distributed velocity data.

Away from the wall, the azimuthal velocity component has skewness of ~ 0 and flatness of ~ 3. For the axial and radial velocity components, there are significant variations of the skewness and flatness values between the different flows. These variations are described in the following paragraphs for the wall-normal position $y^+ \approx 100$.

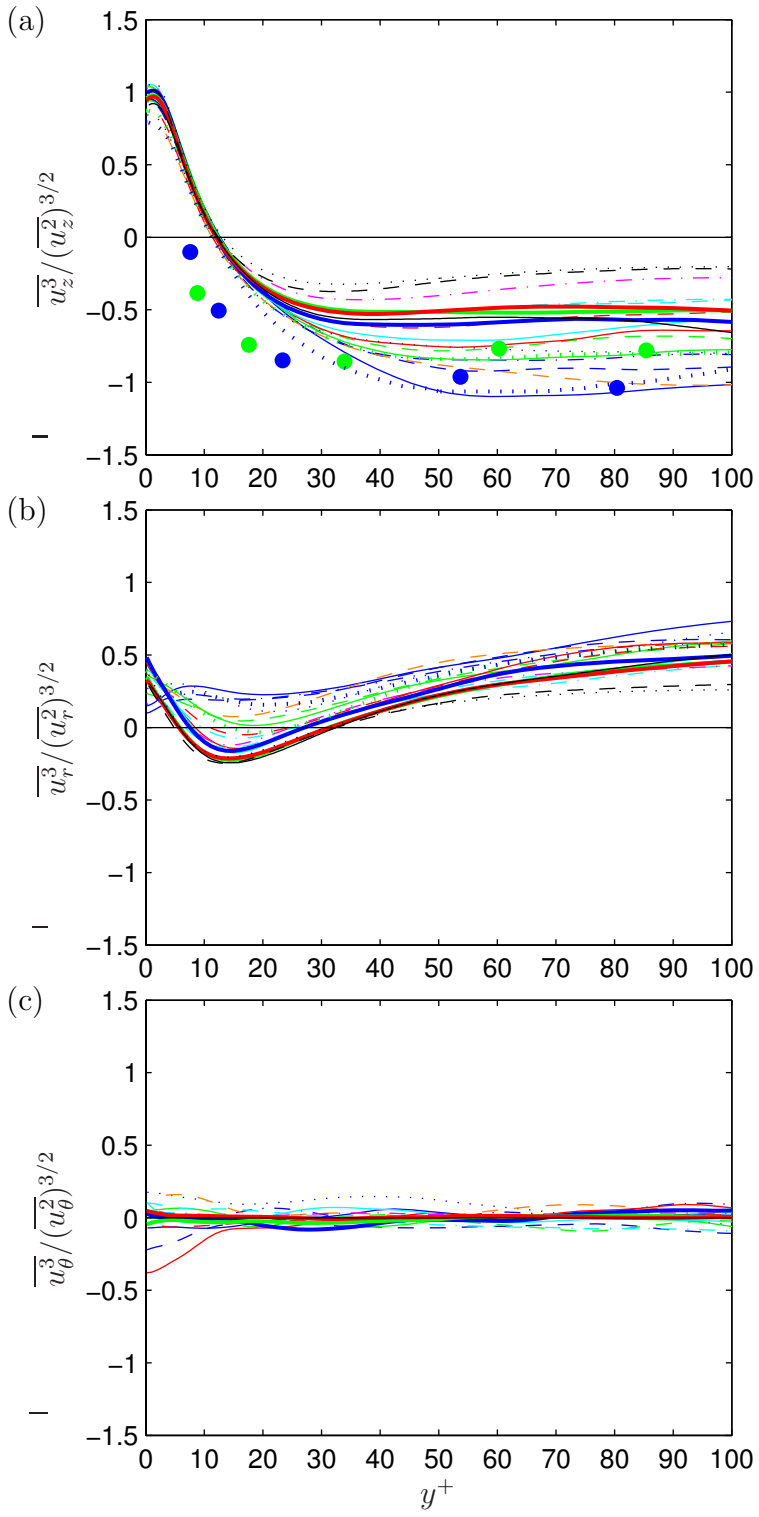

a^+	δ/a	δ^+	Line
21.9	7.82	171	
21.5	14.0	302	
21.5	19.1	411	
21.0	27.6	580	
31.5	7.85	247	
42.7	3.74	159	
40.8	7.74	315	
76.0	2.33	177	
74.3	3.63	270	
146	1.18	173	
140	2.30	321	
131	4.01	527	
163	4.92	802	
287	0.574	165	
564	0.313	177	
1130	0.157	177	

Figure 4.13: Skewness profiles of velocity fluctuations. Velocity components: (a) axial, (b) radial, (c) azimuthal. Line-styles for present simulations are defined in the legend. Moser et al. [1999]: —— $\delta^+ \approx 149$; – – $\delta^+ \approx 326$; ····· $\delta^+ \approx 495$. Neves [1992]: ····· $a^+ = 21.7$, $\delta^+ \approx 201$; ····· $a^+ = 42.8$, $\delta^+ \approx 180$. Luxton et al. [1984]: ● $a^+ = 24.1$, $\delta^+ = 943$; ● $a^+ = 40.0$, $\delta^+ = 1070$.

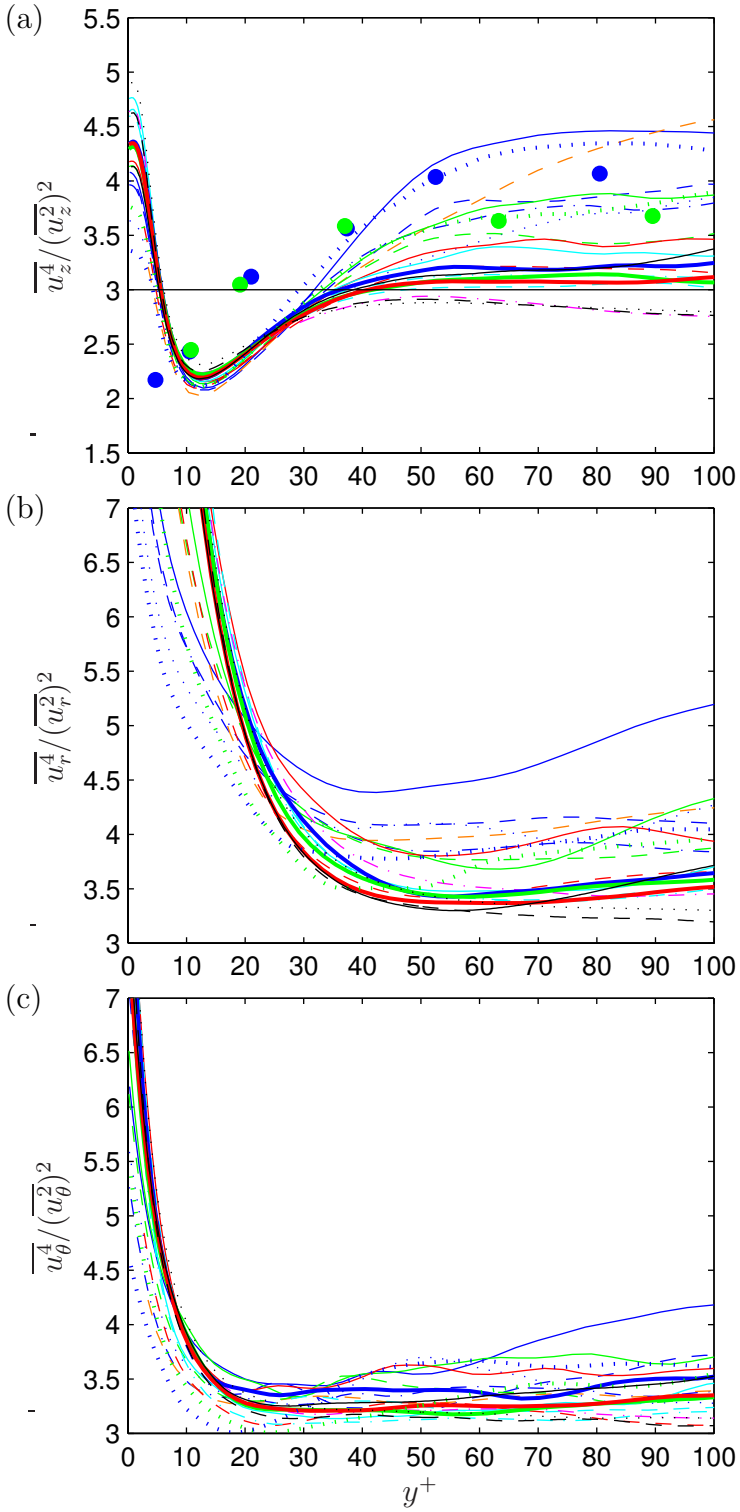

a^+	δ/a	δ^+	Line
21.9	7.82	171	
21.5	14.0	302	
21.5	19.1	411	
21.0	27.6	580	
31.5	7.85	247	
42.7	3.74	159	
40.8	7.74	315	
76.0	2.33	177	
74.3	3.63	270	
146	1.18	173	
140	2.30	321	
131	4.01	527	
163	4.92	802	
287	0.574	165	
564	0.313	177	
1130	0.157	177	

Figure 4.14: Flatness profiles of velocity fluctuations. Velocity components: (a) axial, (b) radial, (c) azimuthal. Line-styles for present simulations are defined in the legend. Moser et al. [1999]: —— $\delta^+ \approx 149$; – – $\delta^+ \approx 326$; ····· $\delta^+ \approx 495$. Neves [1992]: ····· $a^+ = 21.7$, $\delta^+ \approx 201$; ····· $a^+ = 42.8$, $\delta^+ \approx 180$. Luxton et al. [1984]: ● $a^+ = 24.1$, $\delta^+ = 943$; ● $a^+ = 40.0$, $\delta^+ = 1070$.

For flows with similar δ^+ (for example, the flows with $\delta^+ \approx 170$, denoted by solid lines), small values of a^+ ($\lesssim 40$) are associated with skewness values that are more negative for u_z and more positive for u_r compared with the corresponding values for planar or nearly-planar flow (large a^+). For the same selection of flows, the flatness values for both u_z and u_r are more positive for flows with small a^+.

For flows with a given value of a^+ (for example, the flows with $a^+ \approx 22$, denoted by thin blue lines), small values of δ^+ (or δ/a) are associated with skewness values that are more negative for u_z and more positive for u_r compared with the corresponding values for flows with large δ^+. For the same selection of flows, the flatness values for both u_z and u_r are more positive for flows with small δ^+. Thus, the changes caused by decreasing δ^+ (or δ/a) are generally in the same direction as the changes caused by decreasing a^+ (discussed in the previous paragraph).

In the turbulence enhancement mechanism proposed by Luxton et al. [1984], the increase in size of the largest turbulent eddies caused by increasing δ/a is expected to increase the likelihood of large-scale fluid motion across the cylinder. These cross-flows are expected to sweep low-speed fluid outwards from the inner layer. Therefore, as δ/a increases, the skewness of the axial velocity fluctuations outside the wall region is expected to become more negative. However, the present results for $y^+ \approx 100$ indicate that for a given value of a^+, the skewness is typically *less* negative when δ/a is large than when δ/a is small. Therefore the turbulence enhancement mechanism proposed by Luxton et al. [1984] does not appear to be fully consistent with the present data. A tentative explanation for the observed changes in skewness and flatness is given in the remainder of this section.

The proposed explanation begins with the observation that the dominant contribution to the Reynolds shear-stress for $y^+ \gtrsim 12$ is made by flow structures that have $u_z < 0$ and $u_r > 0$, as found by Kim et al. [1987] for planar flow and Neves [1992] for axisymmetric flow (see also section 4.6 of this thesis). Because the velocity signal at $y^+ \approx 100$ contains the signatures of these structures, it is reasonable to suppose that the observed differences in skewness and flatness of the velocity fields between different flows are due to changes in the signatures of these structures.

The effect of decreasing the boundary layer thickness δ^+ is considered first. Because the size of the largest turbulent eddies is of a similar order to δ while the size of the smallest turbulent eddies is of a similar order to ν/u_τ, reduction of $\delta^+ = \delta/(\nu/u_\tau)$ narrows the range of turbulence scales in the flow. The decreased range of turbulence scales can be expected to result in less efficient mixing of the fluid by turbulence. With reduced mixing of the fluid, coherent flow structures may retain their identities over longer temporal and spatial intervals. The signatures of

flow structures, particularly the predominant structures with $u_z < 0$ and $u_r > 0$, are likely to become more distinct as the efficiency of turbulent mixing decreases. Thus the skewness of axial velocity fluctuations is expected to be more negative and that of radial fluctuations to be more positive for flows with small δ^+ than those with large δ^+ (assuming similar values of a^+). Because the signatures of the structures are likely to be sharper and less "noisy" in flows with small δ^+ than in flows with large δ^+ (assuming similar values of a^+), the flatness values of both u_z and u_r are expected to be more positive when δ^+ is small. These expectations are consistent with the observed behaviour of the skewness and flatness profiles at $y^+ \approx 100$.

The effect of decreasing the value of a^+ is now considered. The instantaneous flow fields presented by Neves [1992], as well as those of the present study shown later in section 6.1, suggest that the number of coherent flow structures distributed around the cylinder tends to decrease as a^+ decreases. The smaller the number of structures present in a region of the flow, the less complicated the interactions between the structures can be, so that structures can be expected to retain their identities over longer temporal and spatial intervals. The velocity signatures of the structures, particularly of the predominant structures with $u_z < 0$ and $u_r > 0$, are likely to become more distinct as the number of structures in a region of fluid decreases. Thus the effects of decreasing a^+ are expected to be similar to those of decreasing δ^+ discussed in the previous paragraph. The skewness of axial velocity fluctuations is expected to be more negative and that of radial fluctuations to be more positive for flows with small a^+ than those with large a^+ (assuming similar values of δ^+). Because the signatures of the structures are likely to be sharper and less "noisy" in flows with small a^+ than in flows with large a^+ (assuming similar values of δ^+), the flatness values of both u_z and u_r are expected to be more positive when a^+ is small. These expectations are consistent with the observed behaviour of the skewness and flatness profiles at $y^+ \approx 100$.

It is noted in closing this section that turbulence enhancement due to large-scale cross-flows, of the kind proposed by Luxton et al. [1984], is not ruled out by the above explanation. However, the skewness and flatness results obtained from the present simulations suggest that large-scale cross-flows do not play a major role in the generation or transport of turbulence in axisymmetric boundary layers.

Quadrant	Sign[u_z]	Sign[u_r]	Description of Event
1	+	+	Outward motion of high-speed fluid
2	−	+	Outward motion of low-speed fluid — "burst"
3	−	−	Inward motion of low-speed fluid
4	+	−	Inward motion of high-speed fluid — "sweep"

Table 4.5: Quadrants of the Reynolds shear-stress.

4.6 Quadrant Analysis

Quadrant analysis provides information on the significance of various events in the production of Reynolds stress. The quadrants are identified by the signs of u_z and u_r, as shown in table 4.5.

The relative contribution of events from each quadrant to the total Reynolds shear-stress is shown in figure 4.15. The dominance of the fourth quadrant events for $y^+ \lesssim 12$ and the second quadrant events for $y^+ \gtrsim 12$ has been noted in previous studies, including the plane-channel simulations of Kim et al. [1987] and the cylinder simulations of Neves [1992]. The results of the present calculations for a range of a^+, δ^+ and δ/a (δ^+/a^+) values indicate that the partition of the Reynolds stress is only slightly affected by transverse surface curvature, and then only when a^+ is very small.

Figure 4.16 shows the partition of Reynolds stress events both by quadrant and intensity threshold at three different wall-normal positions. For a threshold of zero, the contribution of each quadrant corresponds to that shown in figure 4.15 at a given value of y^+. There is little difference between the results for the range of flows considered.

The quadrant analyses suggest that the generation of Reynolds shear-stress in transversely curved boundary layers involves the same fundamental processes in similar proportions to those found in planar boundary layers.

4.7 Vorticity Fluctuations

The cylindrical components of the vorticity vector are related to the velocity field by equation 2.6. The intensity of the vorticity fluctuations for the present simulations and those of Neves [1992] and Moser et al. [1999] are shown, normalised by u_τ^2/ν and as functions of y^+, in figure 4.17. There is good agreement between the results of the different investigations for similar flow cases.

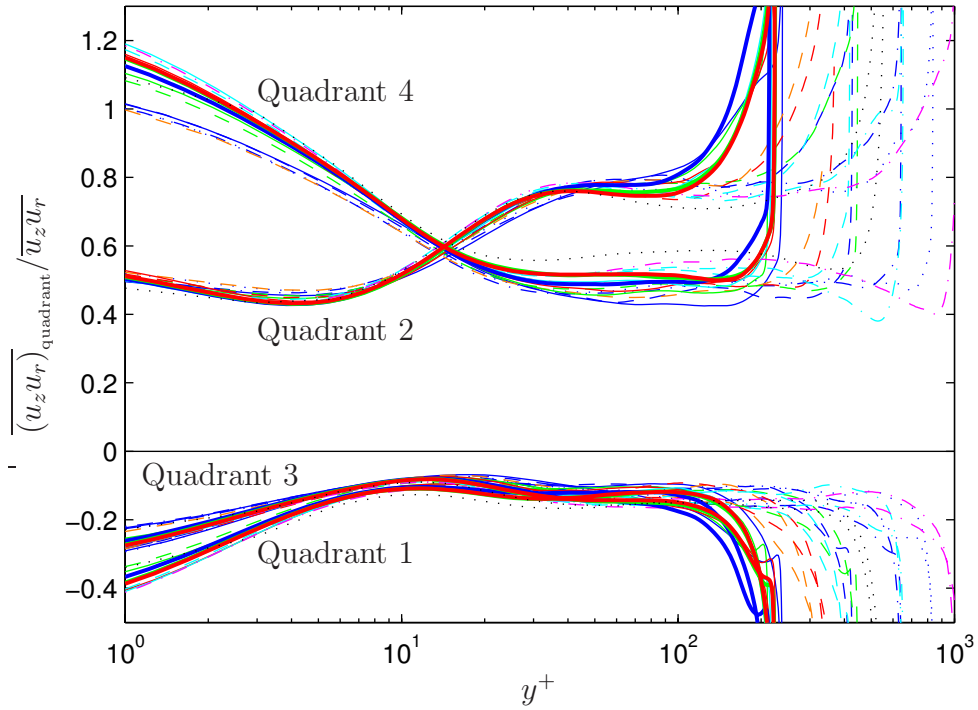

Figure 4.15: Fraction of mean Reynolds shear-stress contributed by each quadrant as a function of y^+. Moser et al. [1999]: ····· $\delta^+ \approx 495$. Present data:

a^+	δ/a	δ^+	Line	a^+	δ/a	δ^+	Line	a^+	δ/a	δ^+	Line	a^+	δ/a	δ^+	Line
21.9	7.82	171	——	31.5	7.85	247	– –	74.3	3.63	270	– –	163	4.92	802	– · –
21.5	14.0	302	– –	42.7	3.74	159	——	146	1.18	173	——	287	0.574	165	——
21.5	19.1	411	– · –	40.8	7.74	315	– –	140	2.30	321	– –	564	0.313	177	——
21.0	27.6	580	·····	76.0	2.33	177	——	131	4.01	527	– · –	1130	0.157	177	——

Near the wall, the profiles of the three vector components of vorticity for each individual flow are significantly different from one another, reflecting the geometry of the instantaneous flow structures that occur in the wall region. The maximum intensity of the azimuthal and axial components occurs at the wall, where the radial component goes to zero to satisfy the no-slip condition. The axial component has a local minimum at $y^+ \approx 5$ and a local maximum at $y^+ \approx 20$. The azimuthal component decreases rapidly away from the wall until $y^+ \approx 10$, where there is a marked decrease in the rate of decay. The maximum of the radial component occurs at $y^+ \approx 13$ for plane channel flow, decreasing to $y^+ \approx 10$ when a^+ is small.

In the neighbourhood of the wall ($y^+ \lesssim 40$), the RMS vorticity profiles for flows with similar a^+ are little affected by the value of δ^+ (or δ/a). On the other hand, the profiles are strongly affected by the value of a^+. When a^+ is small, the profiles for each vorticity component are greatly reduced compared with plane-channel profiles;

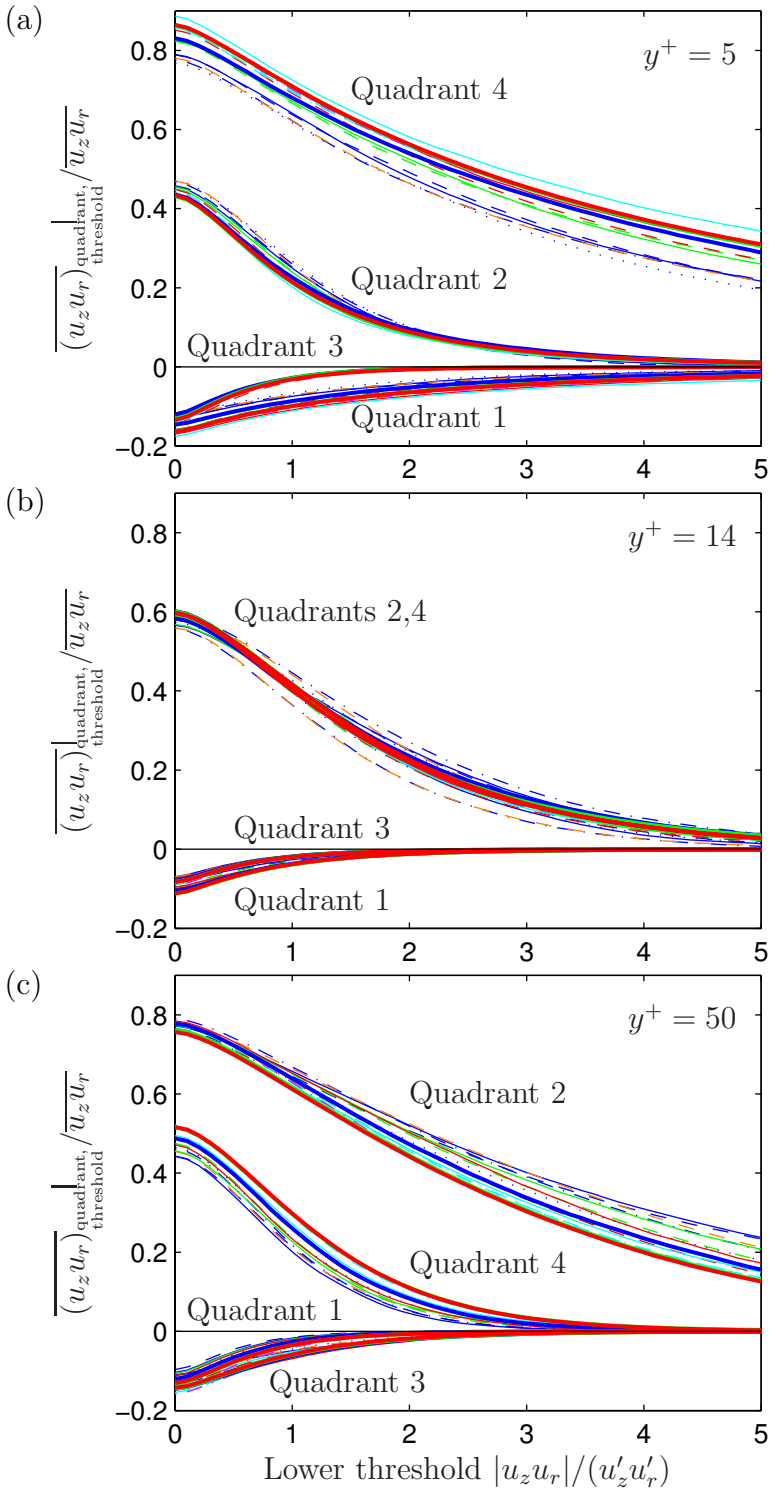

a^+	δ/a	δ^+	Line
21.9	7.82	171	
21.5	14.0	302	
21.5	19.1	411	
21.0	27.6	580	
31.5	7.85	247	
42.7	3.74	159	
40.8	7.74	315	
76.0	2.33	177	
74.3	3.63	270	
146	1.18	173	
140	2.30	321	
131	4.01	527	
163	4.92	802	
287	0.574	165	
564	0.313	177	
1130	0.157	177	

Figure 4.16: Fraction of mean Reynolds shear-stress contributed by each quadrant as a function of threshold at (a) $y^+ = 5$, (b) $y^+ = 14$, (c) $y^+ = 50$. Threshold values are normalised by $u_r' u_z'$. Line-styles for present simulations are defined in the legend.

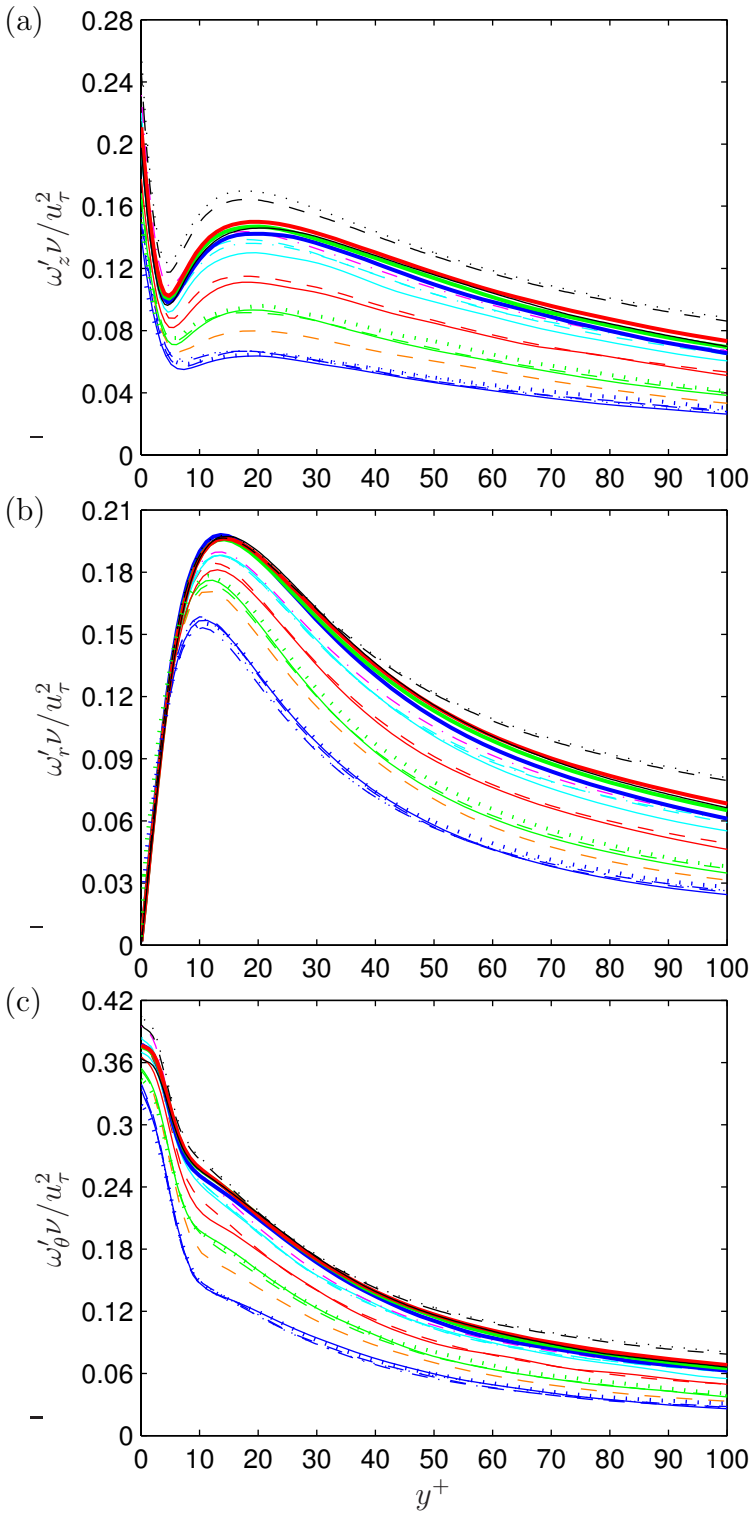

a^+	δ/a	δ^+	Line
21.9	7.82	171	
21.5	14.0	302	
21.5	19.1	411	
21.0	27.6	580	
31.5	7.85	247	
42.7	3.74	159	
40.8	7.74	315	
76.0	2.33	177	
74.3	3.63	270	
146	1.18	173	
140	2.30	321	
131	4.01	527	
163	4.92	802	
287	0.574	165	
564	0.313	177	
1130	0.157	177	

Figure 4.17: RMS vorticity fluctuations in wall units. Vorticity components: (a) axial, (b) radial, (c) azimuthal. Line-styles for present simulations are defined in the legend. Moser et al. [1999]: —— $\delta^+ \approx 149$; – – $\delta^+ \approx 326$; ····· $\delta^+ \approx 495$. Neves [1992]: ····· $a^+ = 21.7$, $\delta^+ \approx 201$; ····· $a^+ = 42.8$, $\delta^+ \approx 180$.

the profiles for flow over cylinders become more similar to the plane-channel results as a^+ increases.

The RMS vorticity profiles are re-plotted in figure 4.18 as functions of y/h, where h denotes the radial width $(b-a)$ of the cylindrical domain or the plane-channel half-width. Results for some of the present simulations are omitted for clarity. Profiles for the plane-channel simulations do not collapse to a common curve away from the wall, unlike the corresponding profiles for RMS velocity (figure 4.8). In fact, the RMS vorticity at a given y/h location decreases as δ^+ increases. For flow at a given value of δ^+, the RMS vorticity profile is shifted downwards as transverse curvature of the boundary layer increases, that is as δ/a increases (and a^+ decreases). The RMS vorticity profiles for cylinders do not collapse with scaling based on $u_{\tau c}$ (equation 4.22), not even for flows with similar δ^+. A satisfactory scaling relation for the RMS vorticity in the outer boundary layer has yet to be found.

For a chosen flow at a given y/h location in the outer part of the boundary layer, the fluctuation intensities of the three vorticity components are similar. In fact, when the RMS vorticity profiles for the three vector components of a given flow are plotted on a single set of axes (not shown), the profiles tend towards a common curve with increasing y/h.

The RMS vorticity profiles for the present simulations (in figure 4.18) decay smoothly in the outer part of the boundary layer, except in the immediate vicinity of the outer domain boundary. The computational method forces the radial component of vorticity to vanish at the outer boundary. Consequently, there is a local, sharp increase in the fluctuation intensity of the azimuthal and axial vorticity components so that the vorticity field remains divergence-free. In comparison, the profiles for the cylinder simulations of Neves [1992] indicate that the fluctuation intensity of the azimuthal and axial vorticity components decays rapidly towards zero as y/h approaches unity. There is no correspondingly rapid variation in the RMS vorticity profile for the radial vorticity component. Unlike the vorticity boundary conditions used for the present simulations, the velocity boundary conditions used by Neves appear not to produce significant distortion of the vorticity field near the outer boundary. However, the velocity boundary condition $U_r[b] = 0$, which confines the flow within the domain boundaries, hinders the motion of large-scale structures either in the wall-normal direction or across the cylinder. Regardless of the details of the chosen boundary conditions, some form of distortion is unavoidable in simulations of the statistically-steady state in a truncated domain.

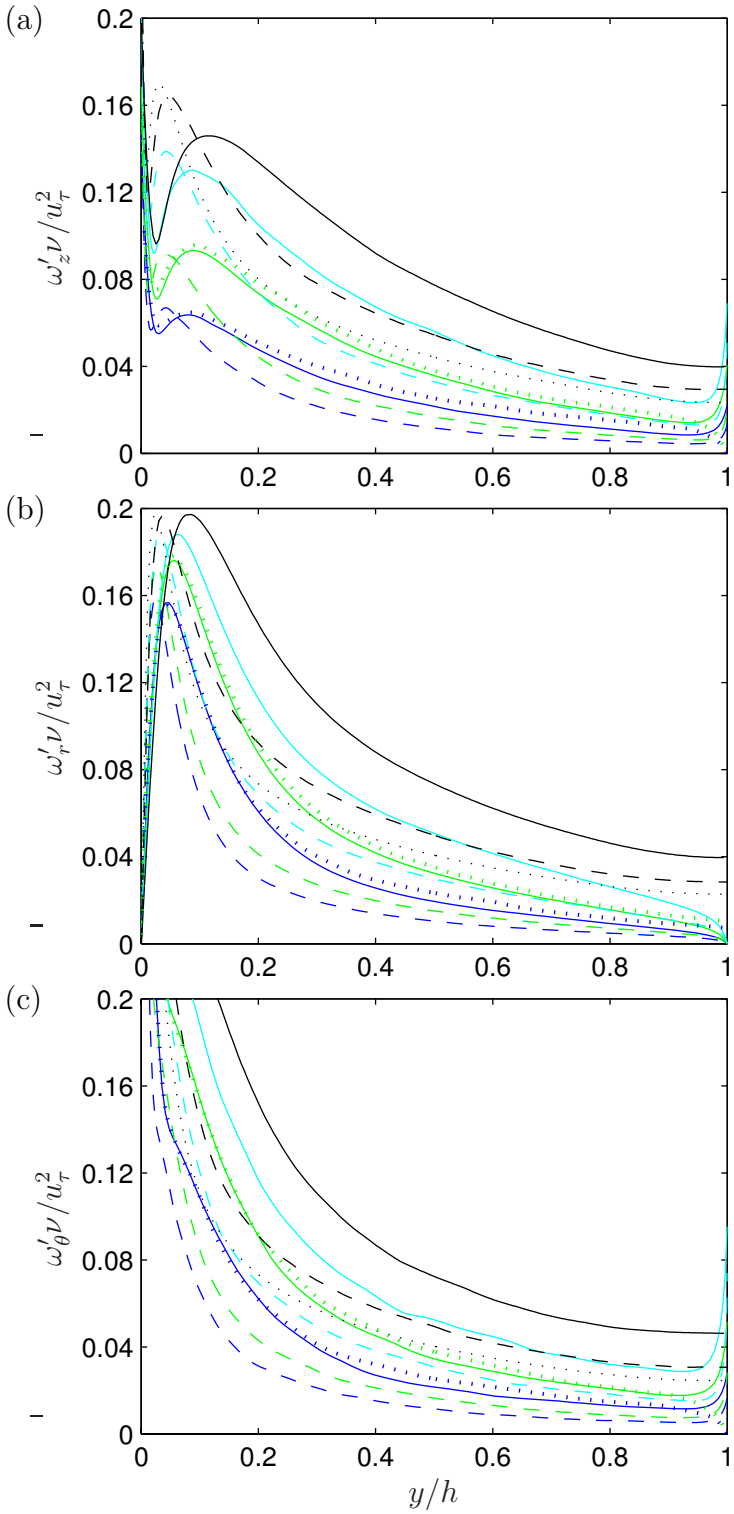

Source	a^+	δ/a	δ^+	Line
Present work	21.9	7.82	171	
	21.5	14.0	302	
	42.7	3.74	159	
	40.8	7.74	315	
	146	1.18	173	
	140	2.30	321	
Neves [1992]	21.7	9.23	201	
	42.8	4.20	180	
Moser et al. [1999]	∞	0	149	
			326	
			495	

Figure 4.18: RMS vorticity fluctuations normalised by u_τ^2/ν as functions of y/h. Vorticity components: (a) axial, (b) radial, (c) azimuthal. Line-styles for reference data and a selection of the present simulations are defined in the legend.

4.8 Summary and Conclusions

Quantities derived from the calculated velocity fields of cylinder and plane-channel simulations have been examined to determine the effects of changing Re_a (or a^+), Re_δ (or δ^+) and δ/a.

Mean velocity profiles in wall units, with $\overline{U_z}/u_\tau$ plotted as functions of y^+, appear to cluster into groups with similar values of a^+. As a^+ decreases, the profiles depart from the planar profile at decreasing values of y^+, and the slope of the profiles in the logarithmic region decreases below that corresponding to planar flow. The calculated profiles nearly collapse to a common curve when they are scaled using the axisymmetric wall units of Rao [1967] ($\overline{U_z}/u_\tau$ versus $a^+ \ln[1 + y^+/a^+]$). In velocity-defect form, with $(V_\infty - \overline{U_z})/u_\tau$ plotted against y/δ, the profiles are strongly dependent on δ/a in the outer part of the boundary layer. As δ/a increases, the slope of the cylinder profiles becomes less negative near $y/\delta = 1$, where the value of the velocity-defect is $0.01V_\infty/u_\tau$ by definition. A generally applicable scaling relation for the mean velocity profile in the outer part of axisymmetric boundary layers is yet to be found.

The values of $\overline{U_z^+}$ at $y = \delta$ for velocity profiles plotted in the axisymmetric wall units of Rao [1967] lie close to the profile corresponding to the logarithmic law for axisymmetric flow (equation 4.16). This observation leads to the empirical expression $V_\infty/u_\tau \approx 2.97 \ln\big[Re_a \ln[1 + \delta/a]\big] - 5.82$, which may be used to estimate wall-parameters such as a^+ and the skin friction coefficient C_f for given values of the outer-flow parameters Re_a and δ/a.

Profiles of the Reynolds shear-stress normalised by u_τ^2, for flow over cylinders at a given δ^+, have a peak value that increases towards the corresponding plane-channel result as a^+ increases. For flows where a^+ is large, the peak Reynolds shear-stress increases towards u_τ^2 as δ^+ increases. Profiles of the Reynolds shear-stress normalised by $u_{\tau c}^2$, where $u_{\tau c}$ is the velocity-scale proposed by Neves [1992] (equation 4.22), collapse to a common curve away from the wall when plotted as functions of y/h, where h denotes either the radial width $(b - a)$ of the computational domain or the plane-channel half-width. The collapse extends all the way to the wall for flows with similar δ^+, indicating that the velocity-scale $u_{\tau c}$ successfully accounts for the effects of transverse curvature on the distribution of the Reynolds shear-stress.

The peak values of RMS velocity profiles normalised by u_τ appear to increase as δ^+ increases. The limiting values suggested by the data for plane-channels are $u'_z/u_\tau \lesssim 3.0$, $u'_r/u_\tau \lesssim 1.1$ and $u'_\theta/u_\tau \lesssim 1.5$. For flow over cylinders at a given value of δ^+, the peak value of each component of the turbulence intensity increases towards

the corresponding plane-channel result as a^+ is increased. When normalised by $u_{\tau c}$ and plotted as functions of y/h, the RMS velocity profiles collapse to a common curve away from the wall, reflecting the behaviour of the Reynolds shear-stress. For the axial velocity component, but not the radial or azimuthal components, the RMS velocity profiles (in the form $u'/u_{\tau c}$ vs y/h) for flows with similar δ^+ collapse throughout the boundary layer, including near the wall. In fact, the mean-square value of the axial (streamwise) velocity fluctuations at a small distance y^+ ($\lesssim 30$) from a cylinder is reduced, relative to the corresponding value for planar flow, as the spanwise distance around the cylinder at radius $a^+ + y^+$ increases relative to the cylinder circumference (see equation 4.25). The mean-square values of the radial (wall-normal) and azimuthal (spanwise) velocity fluctuations are also reduced in cylindrical boundary layers compared with planar flow, but not by the same proportion as the axial (streamwise) fluctuations.

Terms of the transport equation for turbulence kinetic energy, when normalised by τ_w and u_τ^2/ν and plotted as functions of y^+, are strongly affected by the value of a^+; as a^+ decreases, the absolute value of the profiles decreases at a given y^+. This trend is consistent with the results for Reynolds shear-stress and turbulence intensity, although the terms of the turbulence kinetic energy budget do not scale with $u_{\tau c}$. The total-rate-of-change term of the budget is very small in relation to the production-rate term, confirming that the results of the present simulations correspond very nearly to a statistically-steady state.

Away from the wall, the skewness and flatness values of the axial and radial velocity components exhibit significant variations between the different flows considered in the present simulations. The turbulence enhancement mechanism proposed by Luxton et al. [1984], based on the idea that low-speed fluid may be swept into the outer flow by motion across the cylinder of large-scale turbulence structures, does not appear to be fully consistent with the observed trends. A possible explanation for the observed trends is proposed which focuses on the interaction and mixing of coherent structures in the flow. The less effective the mixing is, the more distinct the velocity signatures of the structures are likely to be. It is argued that changes in the quality of the velocity signatures of the individual structures combine to produce the observed differences in skewness and flatness values between different flows.

Quadrant analyses of the velocity fluctuations indicate that the fraction of the Reynolds shear-stress contributed by each quadrant is similar for all of the present cylinder simulations and the plane-channel calculations of Moser et al. [1999]. The results suggest that the processes responsible for generation of the Reynolds shear-

stress in boundary layers on cylinders are not fundamentally different from those in planar boundary layers.

Profiles of RMS vorticity fluctuations for the three vorticity components in a given flow are greatly different from one another near the cylinder surface, but they tend towards a common curve away from the wall. At a given value of δ^+, the intensity of the vorticity fluctuations, normalised by u_τ^2/ν, decreases throughout the boundary layer as a^+ decreases. None of the scaling relations considered in the present study, for either planar or axisymmetric flow, successfully collapses the RMS vorticity profiles to a common curve in the inner or outer boundary layer; a satisfactory scaling relation for the RMS vorticity has yet to be identified.

Scaling relations based on the velocity-scale $u_{\tau c}$ successfully account for the effects of transverse boundary layer curvature on several different velocity statistics computed from the results of the present simulations. The velocity-scale, in the form given by equation 4.23, is a function of y/h with explicit dependence on the ratio b/a. The value of $u_{\tau c}$ decreases from u_τ at the cylinder wall to $u_\tau\sqrt{2/(b/a+1)}$ at $y = h$. When $b/a \approx 1$, $u_{\tau c}$ is similar to the friction velocity u_τ throughout the boundary layer. Near the cylinder wall, that is for $y \ll b+a$, $u_{\tau c}^2/u_\tau^2 \approx a^+/(a^+ + y^+)$, so that $u_{\tau c}$ differs significantly from u_τ when a^+ is small. These properties of the velocity-scale $u_{\tau c}$ support the idea that, when a^+ is large, transverse curvature effects associated with non-zero values of δ/a ($b/a > 1$) are significant only in the outer boundary layer, and when a^+ is small, both the inner and outer portions of the boundary layer are affected by curvature.

Profiles of velocity statistics plotted in wall units for the plane-channel simulations of Moser et al. [1999] exhibit a dependence on the value of δ^+ even at positions y^+ that are close to the solid wall. However, the results suggest that for large values of δ^+, the near-wall velocity statistics are little affected by further increases in δ^+. In other words, the observed influence of δ^+ on the near-wall velocity statistics is significant only at low Reynolds numbers. For the present simulations of flow over cylinders, the effects of transverse boundary layer curvature and δ^+ are combined in a complicated fashion. It is reasonable to suppose that when δ^+ is large, the near-wall velocity statistics (in wall units) will be affected only by curvature, and then only when a^+ is small (and δ/a therefore very large).

The velocity statistics obtained for two flow cases by Neves [1992], with boundary conditions imposed on velocity, have been compared with the statistics produced by the present simulation procedure, which imposes boundary conditions on vorticity. The effects of the different boundary conditions are most noticeable near the outer boundary of the computational domain; there appears to be no significant effect on

the velocity statistics near the cylinder wall. While it is possible to argue that the present boundary conditions are more realistic than those used by Neves, there is no suggestion in the velocity statistics that the velocity boundary conditions suppress any of the essential physical processes at work near the cylinder wall. Regardless of the choice of boundary conditions, some form of distortion is unavoidable in simulations of the statistically-steady state in a truncated domain.

Chapter 5

Pressure Statistics

The simulation procedure described in chapter 2 solves the vorticity transport equation for the vorticity and velocity fields on a cylindrical mesh at each time-step. The pressure field is not an essential part of the solution; it is calculated as a post-processing step or at intervals during the simulation using the method described in section 2.6. For each of the axial-flow simulations discussed in the previous chapter, a temporal record of the turbulent pressure fields at the statistically-steady state has been obtained, in accordance with the temporal parameters listed in tables 3.3 and 3.4.

A variety of statistics calculated from the recorded pressure fields are presented here in conjunction with appropriate reference data for planar and axisymmetric boundary layers. The statistics are analysed to determine the effects of transverse wall curvature on the pressure field. The initial focus is directed towards profiles of the intensity and higher-order moments of the pressure fluctuations. Attention is then given to the radial distribution of the intensity of pressure-source fluctuations, along with the properties of the Green's function that relates the strength of pressure-sources to the pressure they generate at the cylinder wall. The focus is subsequently shifted to the wall-pressure statistics, including spatial and temporal spectra, the convection velocity of pressure-producing eddies, and the root-mean-square wall-pressure. Of particular interest are the scaling relations applicable to the temporal spectra of wall-pressure. The main findings are summarised at the end of the chapter.

5.1 Moments about the Mean

Profiles of the root-mean-square (RMS) pressure fluctuations for the present simulations are shown, normalised by the wall-shear-stress, in figure 5.1a as functions

of y^+. Data are also shown for the cylinder simulations of Neves [1992], and the plane-channel simulations of Moser et al. [1999]. The reference data are in good agreement with the present results for similar flow cases.

The peak value of the RMS pressure fluctuations occurs at $y^+ \approx 30$ for all flows considered. For flow over cylinders at a given δ^+, the peak value increases towards the plane-channel result as a^+ is increased. For example, when $\delta^+ \approx 170$, the peak value of the RMS pressure increases (approximately) from $0.7\tau_w$ to the plane-channel value $2.0\tau_w$ as a^+ varies from 22 to ∞. For the same δ^+ and range of a^+ values, the wall-pressure increases (approximately) from $0.6\tau_w$ to $1.7\tau_w$.

The RMS pressure profiles for the plane-channel simulations are shifted upwards throughout the boundary layer as δ^+ increases. For example, the peak values of the profiles are, respectively, $p'/\tau_w \approx 1.9, 2.5, 2.7$ for $\delta^+ \approx 149, 326, 495$. The velocity statistics for plane-channel flow, such as the Reynolds shear-stress (section 4.2) and RMS velocity fluctuations (section 4.3), have peak values that appear to approach a limiting value with increasing δ^+. The same is not necessarily true of the RMS pressure, because the pressure at a given point is the sum of contributions from pressure-sources located throughout the boundary layer (see section 5.2). It is reasonable to suppose that the RMS pressure at points near the wall continues to increase with δ^+ as the number and size of the pressure-sources supported by the boundary layer increases. The experimental measurements of wall-pressure discussed in section 5.7 suggest that the RMS wall-pressure increases logarithmically with δ^+.

The RMS pressure profiles are re-plotted in figure 5.1b as functions of y/h, where h is either the radial domain width $(b-a)$ or the plane-channel half-width. In the outer part of the boundary layer, the profiles for plane-channels collapse to a common curve. Similarly, the profiles for cylinders are in good agreement in the outer boundary layer for flows with close values of δ/a. In fact, the profiles for all of the flows nearly collapse to a common curve, away from the wall, when normalised by $\rho u_{\tau c}^2$ (not shown) instead of τ_w (ρu_τ^2).

The skewness and flatness of pressure fluctuations across the boundary layer are shown in figure 5.2. Some of the differences between the profiles for different flows have the character of random fluctuations, suggesting that the temporal and spatial extent of the data record may be marginal for the calculation of higher-order moments. Nevertheless, there are consistent trends in the data. For boundary layers on cylinders with large a^+, the skewness and flatness profiles are similar to the profiles for the plane-channel flows. On the other hand, for flow along cylinders with small a^+ ($\lesssim 40$), the skewness is typically more negative and the flatness is typically more positive than is the case for the plane-channel flows. These trends

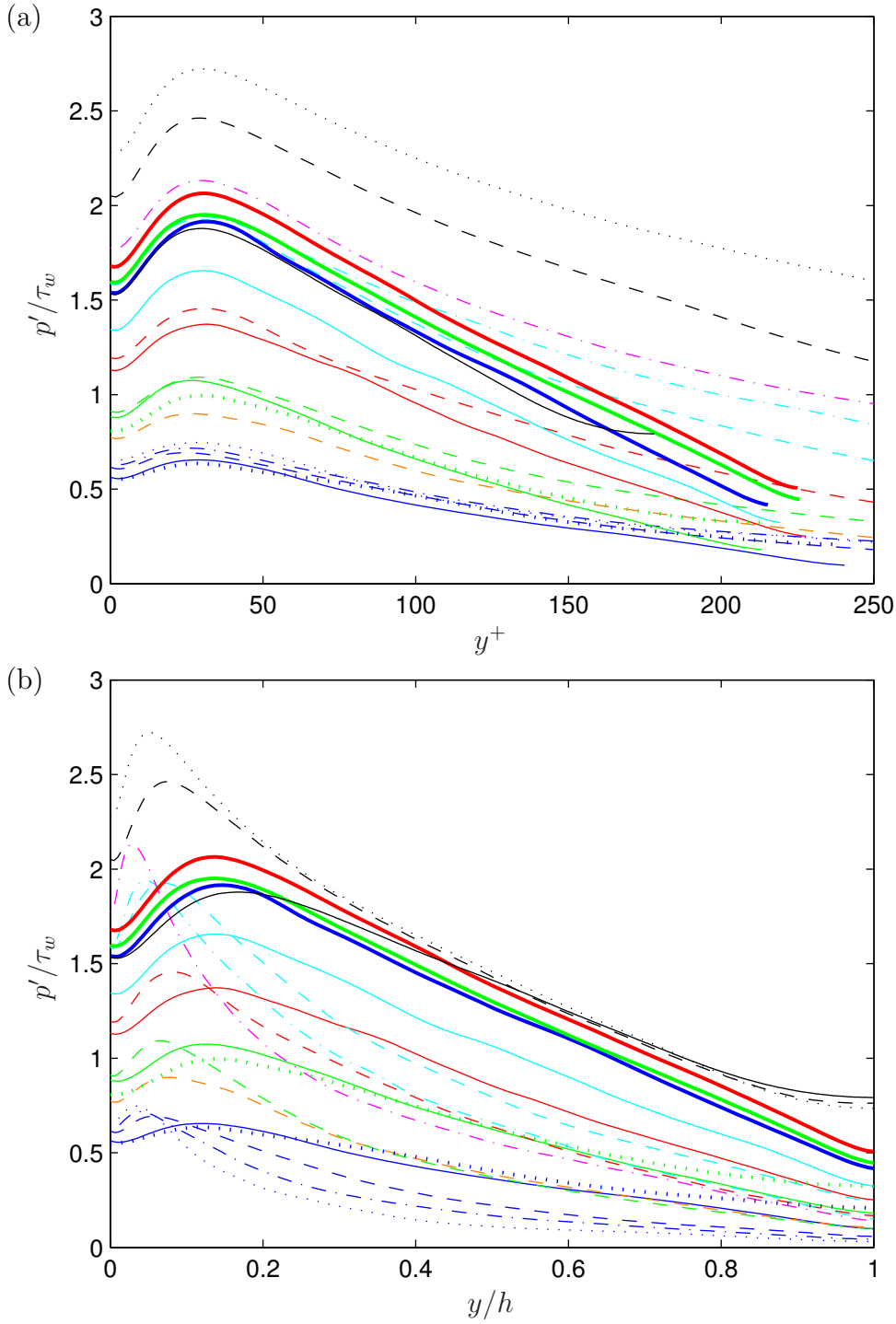

Figure 5.1: Profiles of RMS pressure fluctuations (p'/τ_w) as functions of (a) y^+ and (b) y/h. Moser et al. [1999]: —— $\delta^+ \approx 149$; – – $\delta^+ \approx 326$; ····· $\delta^+ \approx 495$. Neves [1992]: ····· $a^+ = 21.7$, $\delta^+ \approx 201$; ····· $a^+ = 42.8$, $\delta^+ \approx 180$. Present data:

a^+	δ/a	δ^+	Line	a^+	δ/a	δ^+	Line	a^+	δ/a	δ^+	Line	a^+	δ/a	δ^+	Line
21.9	7.82	171	——	31.5	7.85	247	– –	74.3	3.63	270	– –	163	4.92	802	– · –
21.5	14.0	302	– –	42.7	3.74	159	——	146	1.18	173	——	287	0.574	165	——
21.5	19.1	411	– · –	40.8	7.74	315	– –	140	2.30	321	– –	564	0.313	177	——
21.0	27.6	580	·····	76.0	2.33	177	——	131	4.01	527	– · –	1130	0.157	177	——

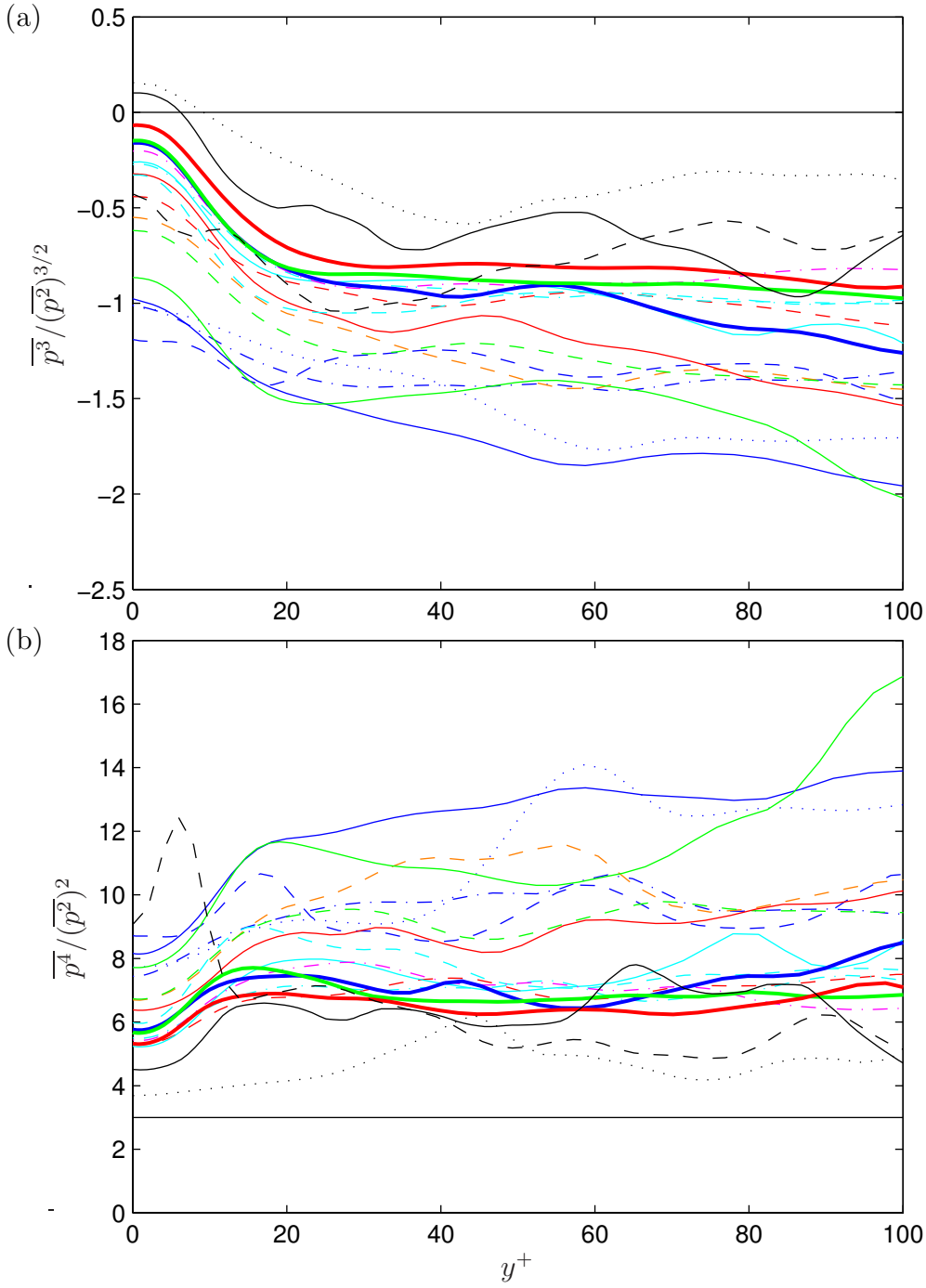

Figure 5.2: (a) Skewness and (b) flatness profiles of pressure fluctuations. Moser et al. [1999]: —— $\delta^+ \approx 149$; – – $\delta^+ \approx 326$; ····· $\delta^+ \approx 495$. Present data:

a^+	δ/a	δ^+	Line	a^+	δ/a	δ^+	Line	a^+	δ/a	δ^+	Line	a^+	δ/a	δ^+	Line
21.9	7.82	171		31.5	7.85	247		74.3	3.63	270		163	4.92	802	
21.5	14.0	302		42.7	3.74	159		146	1.18	173		287	0.574	165	
21.5	19.1	411		40.8	7.74	315		140	2.30	321		564	0.313	177	
21.0	27.6	580		76.0	2.33	177		131	4.01	527		1130	0.157	177	

are similar to those that apply to the axial component of the velocity field away from the wall. The process underlying these trends is discussed in section 4.5.

5.2 Green's Function Analysis

The Fourier coefficients of the pressure field, denoted by $\hat{P}$, are obtained from the velocity field by solution of equation 2.110. Expressed in non-dimensional form with respect to the cylinder radius a and the free-stream velocity V_∞, equation 2.110 becomes

$$(r/a)^2\frac{\partial^2\big(\hat{P}/(\rho V_\infty^2)\big)}{\partial(r/a)^2}+(r/a)\frac{\partial\big(\hat{P}/(\rho V_\infty^2)\big)}{\partial(r/a)}- \\ \big(m^2+(k_z a)^2(r/a)^2\big)\big(\hat{P}/(\rho V_\infty^2)\big)=(r/a)^2(\hat{\lambda}_p a^2/V_\infty^2), \quad (5.1)$$

where $\hat{\lambda}_p$ denotes the Fourier coefficients of the pressure-source field defined by equation 2.111. The corresponding boundary condition at the cylinder wall, where $r/a=1$, is given by equation 2.113, which has the non-dimensional form

$$\frac{\partial\big(\hat{P}/(\rho V_\infty^2)\big)}{\partial(r/a)}[1]=\frac{1}{Re_a}\frac{\partial^2(\hat{U}_r/V_\infty)}{\partial(r/a)^2}[1]. \quad (5.2)$$

The pressure is defined relative to the free-stream pressure, so that the boundary condition at infinity is given by

$$\hat{P}/(\rho V_\infty^2)[\infty]=0. \quad (5.3)$$

The Green's function $\hat{G}[r/a, r_s/a]$ is defined as the solution of equation 5.1 with the right-hand-side set to the Dirac delta function $\delta[r/a-r_s/a]$, where the evaluation point is r/a and the source location is r_s/a. The boundary conditions imposed on the solution are those given by equations 5.2 and 5.3 with the right-hand-sides set to zero. The solution of equation 5.1 with the original right-hand-side may then be expressed as

$$\hat{P}/(\rho V_\infty^2)[r/a]=\int_1^{b/a}\hat{G}[r/a,r_s/a]\left\{(r_s/a)^2(\hat{\lambda}_p a^2/V_\infty^2)[r_s/a]\right\}\,d(r_s/a)+ \\ \text{boundary condition terms.} \quad (5.4)$$

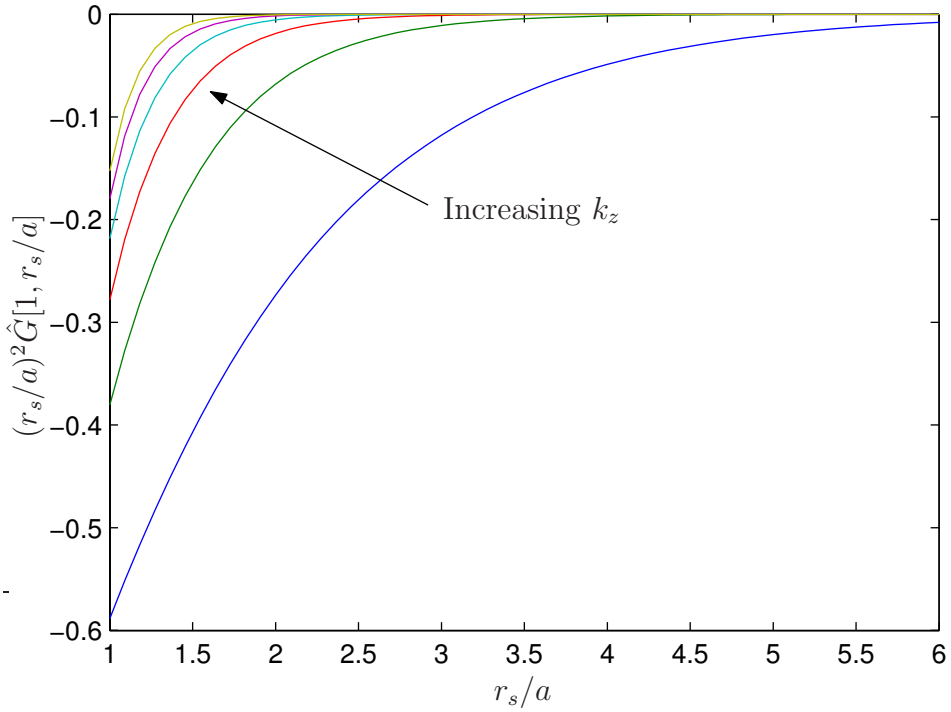

Figure 5.3: Wall-pressure $\left(\hat{P}/(\rho V_\infty^2)[1] = \hat{G}[1, r_s/a](r_s/a)^2\right)$ due to a point source of unit strength $\left(\hat{\lambda}_p a^2/V_\infty^2 = \delta[1 - r_s/a]\right)$ as a function of source position (r_s/a). The azimuthal Fourier mode-number is $m = 1$ and the axial wave-number range is $ak_z = 1, 2, \ldots, 6$; the corresponding Green's function is given by equation 5.5.

The Green's function may be determined by use of the method described by Stakgold [1998, §3.2]. For axial wave-numbers $k_z \neq 0$, the Green's function evaluated at the cylinder wall $(r/a = 1 \leq r_s/a)$ is

$$\hat{G}[1, r_s/a] = \frac{1}{|k_z a|(r_s/a)} \frac{K_{|m|}\left[|k_z a|(r_s/a)\right]}{K'_{|m|}\left[|k_z a|\right]}, \tag{5.5}$$

where $K_{|m|}$ is the modified Bessel function of the second kind of integer order $|m|$ (see figure 2.2) and $K'_{|m|}$ is its derivative.

Figure 5.3 shows the wall-pressure, $\hat{P}/(\rho V_\infty^2)[1] = \hat{G}[1, r_s/a](r_s/a)^2$, due to a point source of unit strength, $\hat{\lambda}_p a^2/V_\infty^2 = \delta[1 - r_s/a]$, for a range of source positions (r_s/a) and axial wave-numbers (k_z). The wall-pressure decreases with increasing axial wave-number. Similar behaviour can be demonstrated for increasing azimuthal wave-number. Thus turbulent eddies that are large in the streamwise or spanwise directions can be expected to make the dominant contribution to the wall-pressure (assuming that the wave-number spectrum of pressure-sources is a uniform or decaying function of wave-number). The other important observation is that wall-pressure decreases rapidly as the pressure-source is moved to larger values of r_s/a. Thus it

is expected that the proportion of the wall-pressure contributed by the outer part of the boundary layer will decrease as the cylinder radius a decreases relative to the boundary layer thickness δ (assuming that for all values of a, the same distribution of pressure-sources is mapped to the radial interval $r_s/a = [1, 1 + \delta/a]$).

5.3 Pressure-Source Fluctuations

The pressure-source in the Poisson equation for pressure (equation 2.109) is expressed in cylindrical coordinates by equation 2.111. The azimuthal and axial homogeneity of the mean flow produced by the present simulations allows the pressure-source to be written in terms of mean and fluctuating velocity components as follows:

$$\lambda_p = -2\frac{d\overline{U_z}}{dr}\frac{\partial u_r}{\partial z} - \left(\frac{\partial u_r}{\partial r}\right)^2 - \frac{2}{r}\frac{\partial u_\theta}{\partial r}\left(\frac{\partial u_r}{\partial \theta} - u_\theta\right) - 2\frac{\partial u_z}{\partial r}\frac{\partial u_r}{\partial z} - \frac{1}{r^2}\left(\frac{\partial u_\theta}{\partial \theta} + u_r\right)^2 - \frac{2}{r}\frac{\partial u_z}{\partial \theta}\frac{\partial u_\theta}{\partial z} - \left(\frac{\partial u_z}{\partial z}\right)^2. \quad (5.6)$$

Profiles of the RMS fluctuations of λ_p, in the form λ_p' normalised by u_τ^4/ν^2 versus y/h, are shown for a representative selection of the present simulations in figure 5.4. The RMS fluctuations are shown separately for each individual term of the above expression and for the total pressure-source.

The first term of the pressure-source represents the contribution of the linear interaction between the mean shear and the velocity fluctuations. The remaining terms represent non-linear interactions within the turbulent velocity field. As found by Kim et al. [1987] and Neves [1992], the linear term is not the dominant contributor to the pressure-source fluctuations. The dominant term near the wall is in fact the third term of equation 5.6, $(2/r)(\partial u_\theta/\partial r)(\partial u_r/\partial\theta - u_\theta)$, which involves velocity derivatives associated with axial (streamwise) vorticity. The peak intensity of the linear term is as low as 1/2 that of the dominant term and 2/5 the peak intensity of the total pressure-source. Away from the wall, the intensity profiles of the pressure-source terms for a given flow tend towards two separate curves. The upper (dominant) curve corresponds to the third, fourth and sixth terms of equation 5.6: $(2/r)(\partial u_\theta/\partial r)(\partial u_r/\partial\theta - u_\theta)$, $2(\partial u_z/\partial r)(\partial u_r/\partial z)$ and $(2/r)(\partial u_z/\partial\theta)(\partial u_\theta/\partial z)$. These terms involve velocity derivatives that are associated, respectively, with axial, azimuthal and radial vorticity fluctuations; their similar intensity in the outer boundary layer reflects the RMS fluctuations of the three vorticity components (figure 4.17).

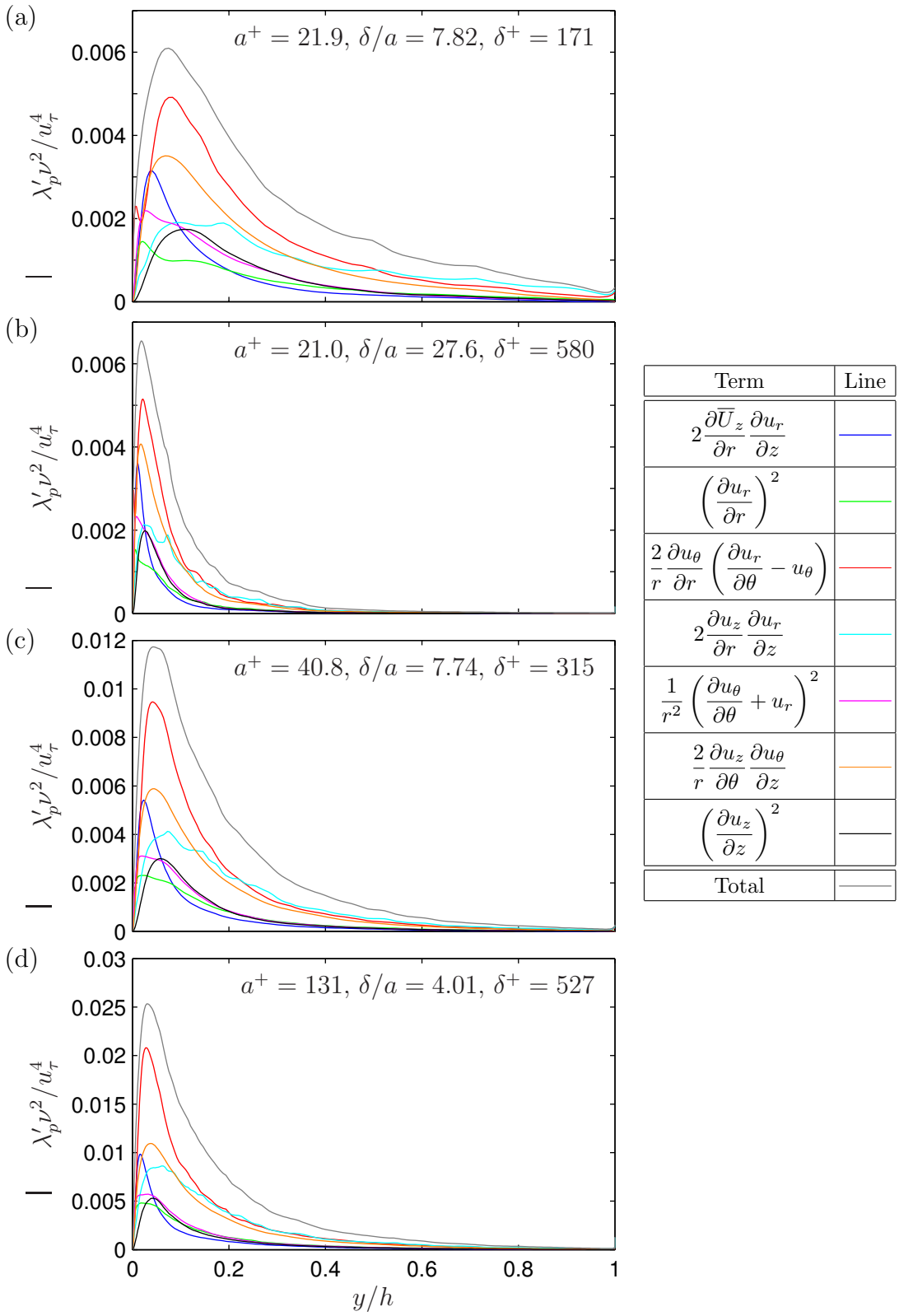

Figure 5.4: RMS fluctuations of pressure-source terms for four of the present simulations. Line-styles for the pressure-source terms are defined in the legend.

Profiles of the RMS fluctuations of the total pressure-source are shown for the present simulations*† as functions of y^+ in figure 5.5a. The peak intensity of the pressure-source fluctuations occurs in the vicinity of $y^+ = 20$ for all of the flows considered. For flow at small values of a^+ ($\approx 20, 40$), the peak intensity does not appear to be greatly affected by the value of δ^+ (or δ/a). However, in flows with large a^+ ($\gtrsim 130$), including planar boundary layers (not shown), there is reason to expect that the peak intensity of the pressure-source fluctuations increases towards a limiting value with increasing δ^+. This is because the pressure-source terms at a given point are directly related to local fluctuations in the velocity field. Presumably, the behaviour of the velocity statistics, including the finite limiting values of the peak Reynolds shear-stress (section 4.2) and RMS velocity (section 4.3), is reflected in the RMS pressure-source fluctuations.

In flows with similar values of δ^+, the intensity of the pressure-source fluctuations increases towards the planar result ($\delta/a \to 0$) as the value of a^+ increases. For example, when $\delta^+ \approx 170$, the peak value of the RMS pressure-source profiles (normalised by u_τ^4/ν^2) increases from 0.006 to 0.030 as a^+ increases from 21.9 to 1130 and δ/a decreases from 7.82 to 0.157.

The same profiles are re-plotted as functions of y/h in figure 5.5b. Away from the wall, at a given y/h, the intensity of the pressure-source fluctuations for flows with similar values of δ^+ tends to decrease as δ/a increases. For example, when $\delta^+ \approx 170$, the value of $\lambda_p'\nu^2/u_\tau^4$ at $y/h = 0.5$ decreases from $9.9{\times}10^{-3}$ to $1.4{\times}10^{-3}$ as δ/a increases from 0.157 to 7.82. However, the profiles in the outer boundary layer do not appear to depend solely on the value of δ/a. For flows with similar values of δ/a, the intensity of the pressure-source fluctuations at a given position y/h decreases as δ^+ increases. For example, in the respective flows with similar $\delta/a = 3.74, 4.01, 4.92$ and increasing $\delta^+ = 159, 527, 802$, the corresponding, decreasing values of $\lambda_p'\nu^2/u_\tau^4$ at $y/h = 0.5$ are $3.4 \times 10^{-3}, 1.4 \times 10^{-3}, 0.75 \times 10^{-3}$. A similar trend is observed for flows with $\delta/a \approx 2.3$, and the trend is expected to apply to other values of δ/a including that for planar flow.

A successful scaling relationship for the profiles of pressure-source fluctuation intensity has not been determined. Any such relationship is required to account for the effects of Reynolds number (δ^+) and boundary layer curvature (a^+, δ/a). The replacement of u_τ by $u_{\tau c}$ in figures 5.5a,b does not collapse the profiles to a

*Flow cases $Re_a = 492$, $b/a = 12$ and $Re_a = 1300$, $b/a = 6$ are omitted because the format of their data-files, created using an early version of the simulation code, is not compatible with the post-processing code used to calculate the pressure-source profiles.

†Pressure-source profiles for the plane-channel simulations of Moser et al. [1999] are not currently available, as confirmed by private communication with R. D. Moser.

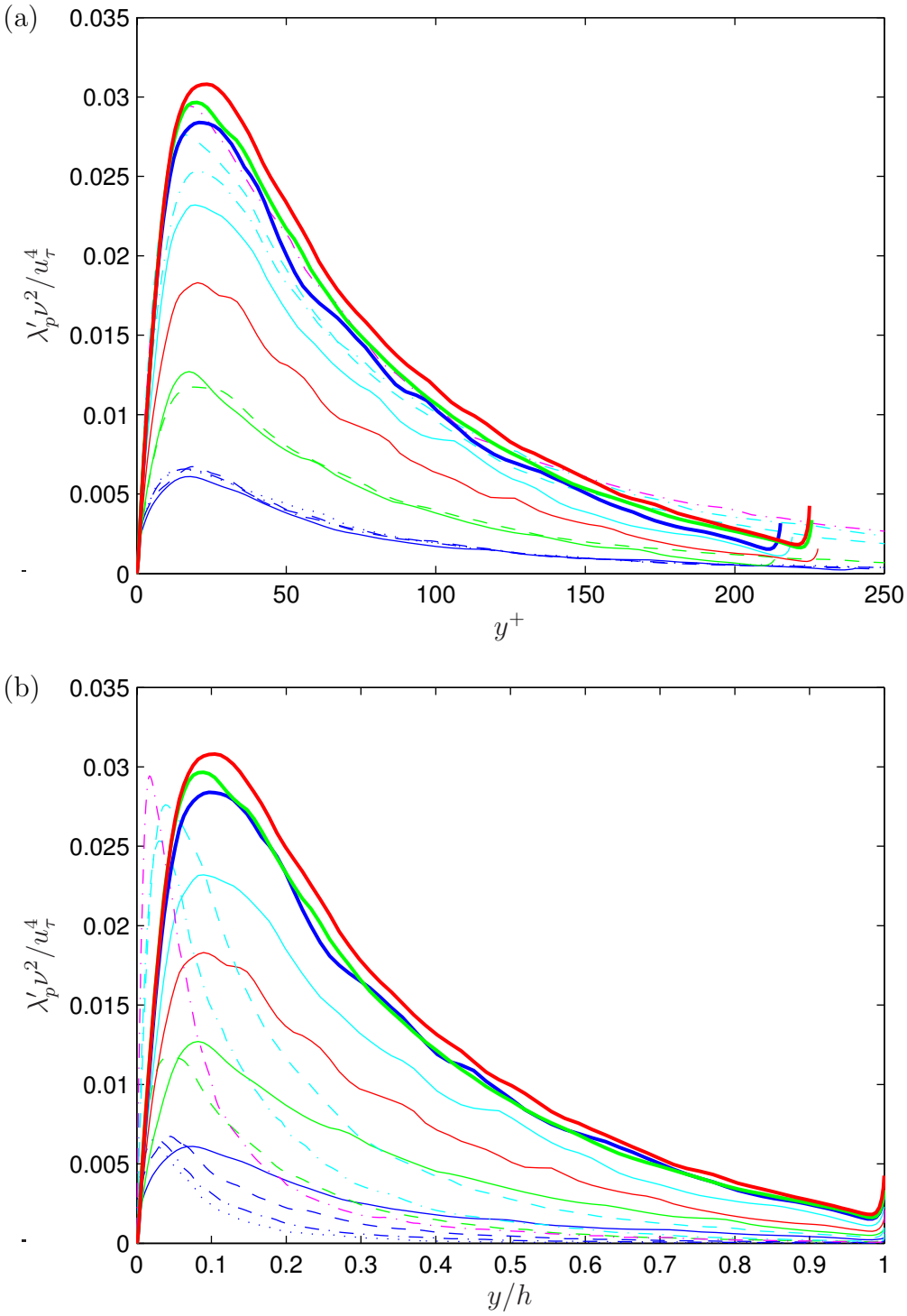

Figure 5.5: RMS fluctuations of total pressure-source for the present simulations as functions of (a) y^+ and (b) y/h. Legend:

a^+	δ/a	δ^+	Line	a^+	δ/a	δ^+	Line	a^+	δ/a	δ^+	Line	a^+	δ/a	δ^+	Line
21.9	7.82	171		-	-	-	-	-	-	-	-	163	4.92	802	
21.5	14.0	302		42.7	3.74	159		146	1.18	173		287	0.574	165	
21.5	19.1	411		40.8	7.74	315		140	2.30	321		564	0.313	177	
21.0	27.6	580		76.0	2.33	177		131	4.01	527		1130	0.157	177	

common curve, not even for flows with similar values of δ^+. Clearly, the scaling of the pressure-source fluctuations is considerably more complicated than the scaling of velocity statistics such as the Reynolds shear-stress or RMS velocity. Nevertheless, determination of the scaling relationship for λ'_p may be a worthwhile subject for future investigation, because the knowledge may enhance our understanding of the trends in the wall-pressure statistics, which are presented in the following sections.

5.4 Spatial Spectra of Wall-Pressure

The azimuthal (spanwise) and axial (streamwise) spectra for wall-pressure fluctuations p_w are defined respectively by

$$E_p[k_\theta] = c_\theta \overline{\left| \sum_{n=0}^{N_\theta - 1} p_w[an\Delta\theta] \, \exp\bigl[-ik_\theta an\Delta\theta\bigr] \right|^2} \tag{5.7}$$

and

$$E_p[k_z] = c_z \overline{\left| \sum_{n=0}^{N_z - 1} p_w[n\Delta z] \, \exp\bigl[-ik_z n\Delta z\bigr] \right|^2}, \tag{5.8}$$

where the grid geometry parameters N_θ, N_z, $\Delta\theta$ and Δz are listed for the present simulations in tables 3.1 and 3.2. Azimuthal and axial wave-numbers are defined by equations 2.26 and 2.27. The overbar denotes averaging in the azimuthal or axial direction and over the temporal record. The scale factors c_θ and c_z are set so that when E_p is plotted against positive wave-number, the area under the single-sided spectrum equals the mean-square value of p_w, that is

$$\int_{k_\theta>0} E_p[k_\theta] \, dk_\theta = \int_{k_z>0} E_p[k_z] \, dk_z = \overline{p_w^2}. \tag{5.9}$$

Wall-pressure spectra as functions of the spanwise (azimuthal) and streamwise (axial) spatial wave-numbers are presented in figure 5.6. The spectra are non-dimensionalised with respect to τ_w and h (which is comparable with δ). The present simulations are in good agreement with the cylinder calculations of Neves [1992] and the plane-channel results of Moser et al. [1999].

The spanwise spectra collapse in the high wave-number range for flows with similar δ^+, independently of δ/a. As δ^+ increases, the spectra are extended in the direction of increasing wave-number. For sufficiently large δ^+, the plane-channel spectra collapse to a common curve in the low wave-number range. As δ/a increases,

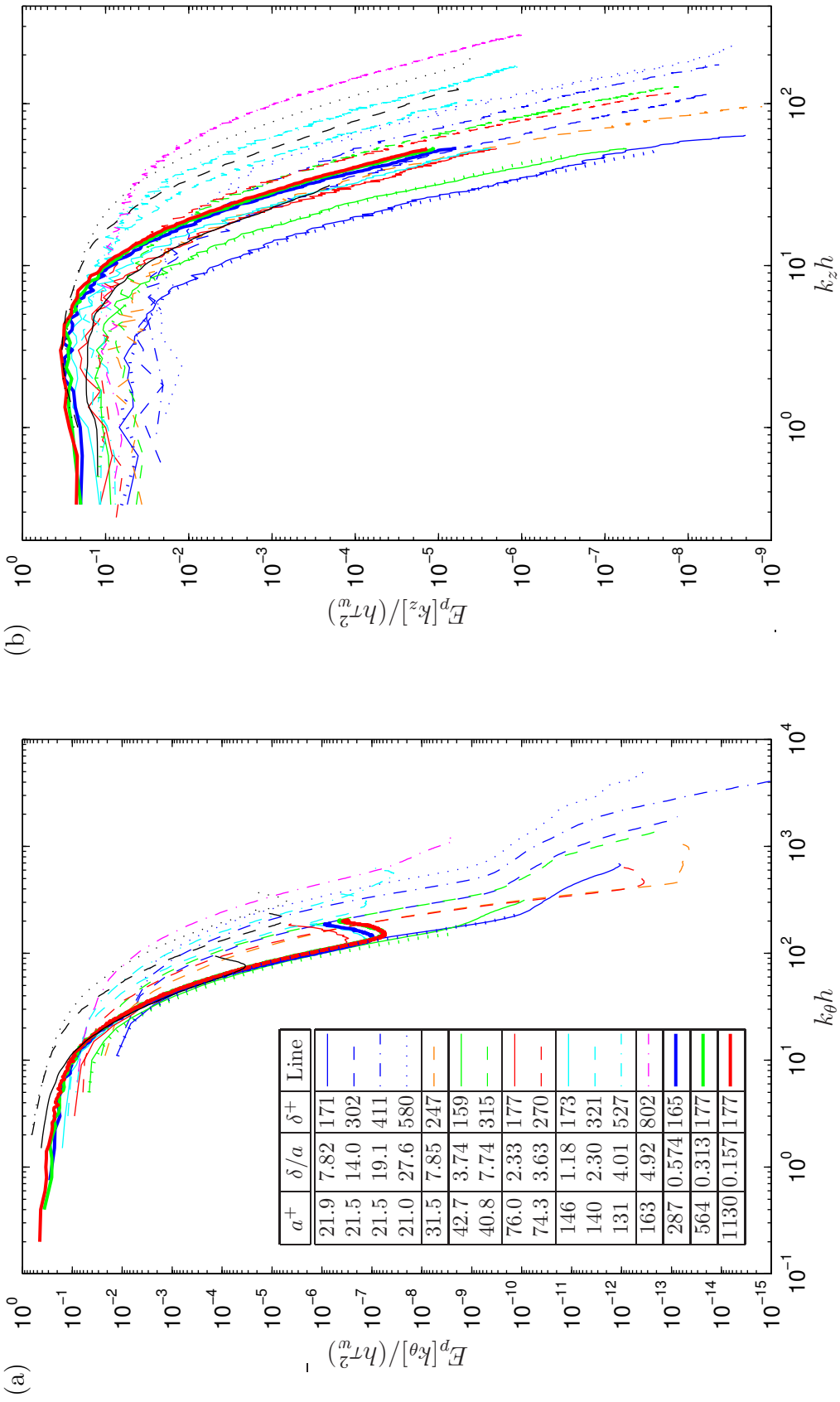

Figure 5.6: Spatial spectra of wall-pressure fluctuations for (a) azimuthal/spanwise and (b) axial/streamwise wave-numbers. Line-styles for present simulations are defined in the legend. Moser et al. [1999]: —— $\delta^+ \approx 149$; – – $\delta^+ \approx 326$; ····· $\delta^+ \approx 495$. Neves [1992]: ····· $a^+ = 21.7$, $\delta^+ \approx 201$; ····· $a^+ = 42.8$, $\delta^+ \approx 180$.

and the corresponding a^+ decreases, the spectra in the low wave-number range are reduced.

The streamwise spectra in the low wave-number range are similar for flows with similar δ/a. As δ/a increases, the spectral level is reduced. In the high wave-number range, there is dependence on both δ^+ and δ/a. Increasing δ^+ extends the spectra in the direction of increasing wave-number, and increasing δ/a has the opposite effect.

Investigation of the scaling relationship between the streamwise spectra in the high wave-number range led Neves [1992] to propose a modified length-scale, which in the current notation is

$$h_f = h\sqrt{1 + \frac{h}{2a}}. \tag{5.10}$$

When h is replaced by h_f in the spectral plot, the cylinder simulations of Neves and the plane-channel simulation of Kim et al. [1987] are found to collapse in the high wave-number range. However, all of these cases involve similar values of δ^+. For other values of δ^+, the spectra do not exhibit similarity.

The scaling properties of streamwise wall-pressure spectra are similar to those of temporal spectra, because the two types of spectra are related by the convection velocity, which is discussed in the section 5.6. The temporal spectra are examined in the following section.

5.5 Temporal Spectra of Wall-Pressure

Definitions

The temporal spectrum φ_p of wall-pressure fluctuations p_w is defined as a function of angular frequency ω by

$$\varphi_p[\omega] = c_t \overline{\left| \sum_{n=0}^{N_t-1} p_w[n\Delta t_s + t_0]\, f_w[n\Delta t_s]\, \exp\left[-i\omega n\Delta t_s\right] \right|^2}, \tag{5.11}$$

where f_w is the Hanning window function:

$$f_w[t] = \frac{1}{2} - \frac{1}{2}\cos\left[\frac{2\pi t}{L_t}\right]. \tag{5.12}$$

The temporal parameters are Δt_s, the sampling period, N_t, the number of samples in an interval, L_t, the duration of an interval, and t_0, the start time of an interval. For the present simulations, values of the temporal parameters are listed in table 3.4. The overbar denotes averaging over a number of temporal intervals and over

Frequency Range	Frequency Limits	Spectral Form
Low-frequency	$\omega\delta^*/V_\infty \leq 0.03$	$\varphi_p V_\infty/(\delta^* Q_\infty^2) = c_1(\omega\delta^*/V_\infty)^2$
Mid-frequency	$5 \leq \omega\delta/u_\tau \leq 100$	$\varphi_p u_\tau/(\delta\tau_w^2) = f_2[\omega\delta/u_\tau]$
Universal	$100 \leq \omega\delta/u_\tau \leq 0.3\delta^+$	$\omega\varphi_p/\tau_w^2 = c_3$
High-frequency	$\omega^+ = \omega\nu/u_\tau^2 \geq 0.3$	$\varphi_p^+ = \varphi_p u_\tau^2/(\nu\tau_w^2) = f_4[\omega^+]$

Table 5.1: Frequency ranges and spectral forms for wall-pressure in planar boundary layers. $Q_\infty = \frac{1}{2}\rho V_\infty$, c_1 and c_3 are constants, and f_2 and f_4 represent functions.

the azimuthal and axial directions. The scale factor c_t is set so that when φ_p is plotted against ω, the area under the single-sided spectrum equals the mean-square value of p_w, that is

$$\int_{\omega>0} \varphi_p[\omega]\, d\omega = \overline{p_w^2}. \tag{5.13}$$

Flat-Plate Spectral Scaling

The turbulent boundary layer on a flat plate has been extensively investigated. Analyses of experimental measurements of surface-pressure fluctuations [see, for example, Farabee and Casarella, 1991, Bull, 1996] have identified four frequency ranges with different forms of spectral scaling. These ranges and forms are listed in table 5.1.

The spectral scaling and frequency ranges for flat-plate flow make an obvious point of reference for the examination of axisymmetric boundary layers.

Low-Frequency Range

The length of the temporal intervals used for calculation of the temporal spectra is such that the lowest spectral frequency (other than $\omega = 0$) is $\omega\delta^*/V_\infty \approx 0.07$, which exceeds the upper limit of the flat-plate low-frequency range. In principle, it is possible to extend the time records so that the low-frequency range is properly resolved. However, the accuracy of the computed flow at low wave-numbers, and hence low frequencies, is limited by the streamwise length of the computational domain. The computational requirements for extension of the domain lengths are well beyond the resources available for the present work. Consequently, comparison of axisymmetric and flat-plate flow similarity in the low-frequency range cannot usefully be made.

Mid-Frequency Range

Temporal wall-pressure spectra for the present calculations and appropriate reference data are plotted in flat-plate mid-frequency form in figure 5.7a. Unlike the flat-plate measurements and plane channel simulation, the spectra for cylinders do not exhibit similarity.

The analysis of the Green's function in section 5.2 suggests that contributions to the wall-pressure from the outer boundary layer can be expected to become less significant as δ/a increases. Therefore the boundary layer thickness δ is unlikely to be the most appropriate length-scale for this frequency range. In fact, the data collapse quite well when the cylinder radius a is used as the length-scale instead of δ. However, in the limiting case of very small δ/a, when the cylinder becomes effectively a flat plate with $a = \infty$, the radius of curvature ceases to be a useful length-scale and must be replaced by δ. A possible composite length-scale L_p that meets the limiting requirements at the extremes of very large and very small δ/a can be defined as

$$L_p = \frac{\delta}{1 + c\delta/a}, \tag{5.14}$$

where c is an empirical constant. Similarity of the results of the present calculations is not very sensitive to the value of c; it is quite close for values of c from about 0.25 to 1. A value of $c = 0.4$ has been chosen as this seems to give the most satisfactory agreement with flat-plate data. This value of c differs slightly from the value $c = 0.25$ chosen by Woods and Bull [2004], whose temporal spectra were derived from wave-number spectra by application of Taylor's hypothesis (as explained later in section 5.6). In the planar limit as $\delta/a \to 0$, $L_p \to \delta$. As δ/a increases, the ratio L_p/δ decreases; at the same time, L_p/a increases towards a limiting value of $L_p/a = 2.5$. For $\delta/a \geq 2.5$, L_p is biased towards the cylinder radius ($L_p \leq \delta/2$).

The spectral data in modified mid-frequency form, where δ is replaced by $L_p = \delta/(1 + 0.4\delta/a)$, are shown in figure 5.7b. In this form there is similarity, with $\varphi_p u_\tau/(L_p \tau_w^2)$ approximately constant over the lower part of the frequency range, down to $\omega L_p/u_\tau \approx 5$. The upper-limit is Reynolds number dependent and given by $\omega L_p/u_\tau \approx 0.4 L_p^+$ (where $L_p^+ = L_p u_\tau/\nu$). The range can therefore be tentatively taken as $5 \leq \omega L_p/u_\tau \leq 0.4 L_p^+$. Other cylinder data are consistent with this range, including the numerical simulations of Neves [1992] and the experimental results of Berera [2004] (which are in good agreement with Snarski and Lueptow [1995]).

The frequency range for similarity of the cylinder spectra contrasts with the flat-plate mid-frequency range of $5 \leq \omega\delta/u_\tau \leq 100$ proposed by Farabee and Casarella [1991]. The plane-channel spectrum of Kim et al. [1987] suggests that the upper

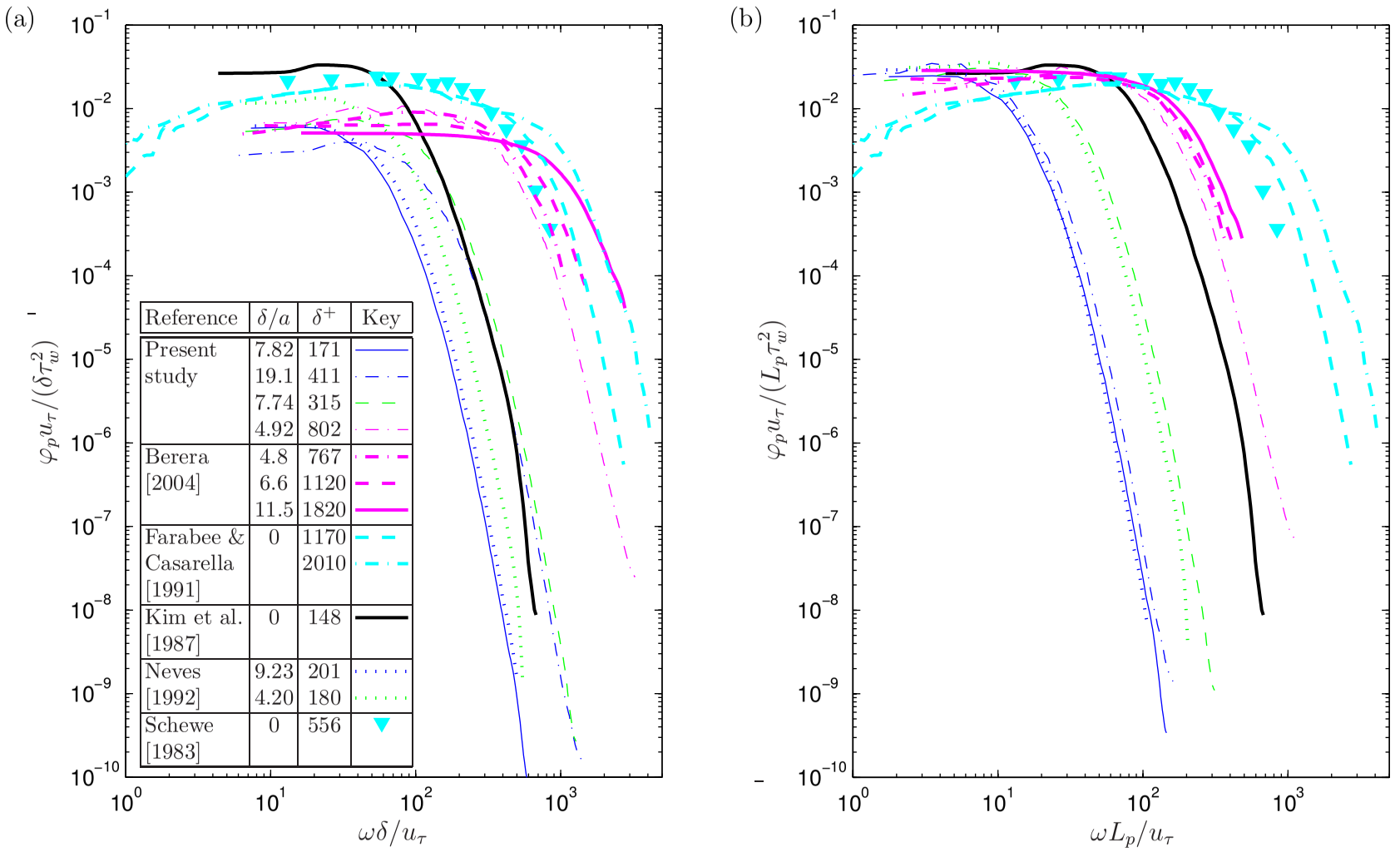

Figure 5.7: Temporal spectra of wall-pressure in mid-frequency form: (a) flat-plate scaling; (b) scaling modified for transverse curvature, where $L_p = \delta/(1 + 0.4\delta/a)$. Line-styles and symbols are defined in the legend.

limit of the flat-plate range may need to be reduced when the Reynolds number δ^+ is small. The dependency of the upper limit of the frequency range on the Reynolds number is a reflection of the fact that the overall RMS pressure fluctuation is also dependent on the Reynolds number, as shown later in section 5.7.

High-Frequency Range

The temporal wall-pressure spectra examined previously are plotted in figure 5.8a in the flat-plate high-frequency form, $\varphi_p^+ = \varphi_p u_\tau^2/(\nu\tau_w^2)$ as a function of $\omega^+ = \omega\nu/u_\tau^2$. For flows with similar values of the cylinder Reynolds number Re_a (or a^+), the spectra show close similarity that is almost independent of the value of δ/a. For all values of a^+ considered, the similarity occurs for ω^+ greater than approximately 0.4, a value near to that for high-frequency similarity in the flat-plate case. However, the similarity curve is not the same for all a^+, the spectral levels increasing with a^+.

The spectral curves for the various cylinder Reynolds numbers have similar forms that can be brought together if the horizontal and vertical scales are multiplied by a function that depends primarily on a^+. Such a function is devised empirically by Woods and Bull [2004], although there does not appear to be any physical basis for the chosen function. The need for such a function suggests that u_τ and the corresponding τ_w are not the appropriate velocity- and stress-scales for transversely curved boundary layers. A plausible substitute for the velocity-scale may be derived from $u_{\tau c}$, which is defined by equation 4.22. It is expected that the high-frequency wall-pressure fluctuations are dominated by contributions from sources near the wall, where $u_{\tau c}$ may be expressed in the form

$$u_{\tau c}^2 \approx u_\tau^2 \left(\frac{a}{a+y} \right), \quad y \ll b + a. \tag{5.15}$$

Evaluation of $u_{\tau c}$ at the location of the maximum RMS fluctuation of the total pressure-source, which occurs at $y^+ \approx 20$ in figure 5.5a, yields the proposed velocity-scale U_p:

$$U_p^2 = u_\tau^2 \left(\frac{1}{1 + 20/a^+} \right). \tag{5.16}$$

For small a^+, $U_p < u_\tau$, and in the planar limit as $a^+ \to \infty$, $U_p = u_\tau$.

The wall-pressure spectra in modified high-frequency form, where u_τ and τ_w are replaced respectively by U_p and ρU_p^2, are shown in figure 5.8b. In this form there is similarity over the approximate frequency range $\omega\nu/U_p^2 \geq 0.4$. The results of the present simulations are in good agreement with the simulations of Kim et al. [1987] and Neves [1992] and the experiments of Farabee and Casarella [1991]. The present

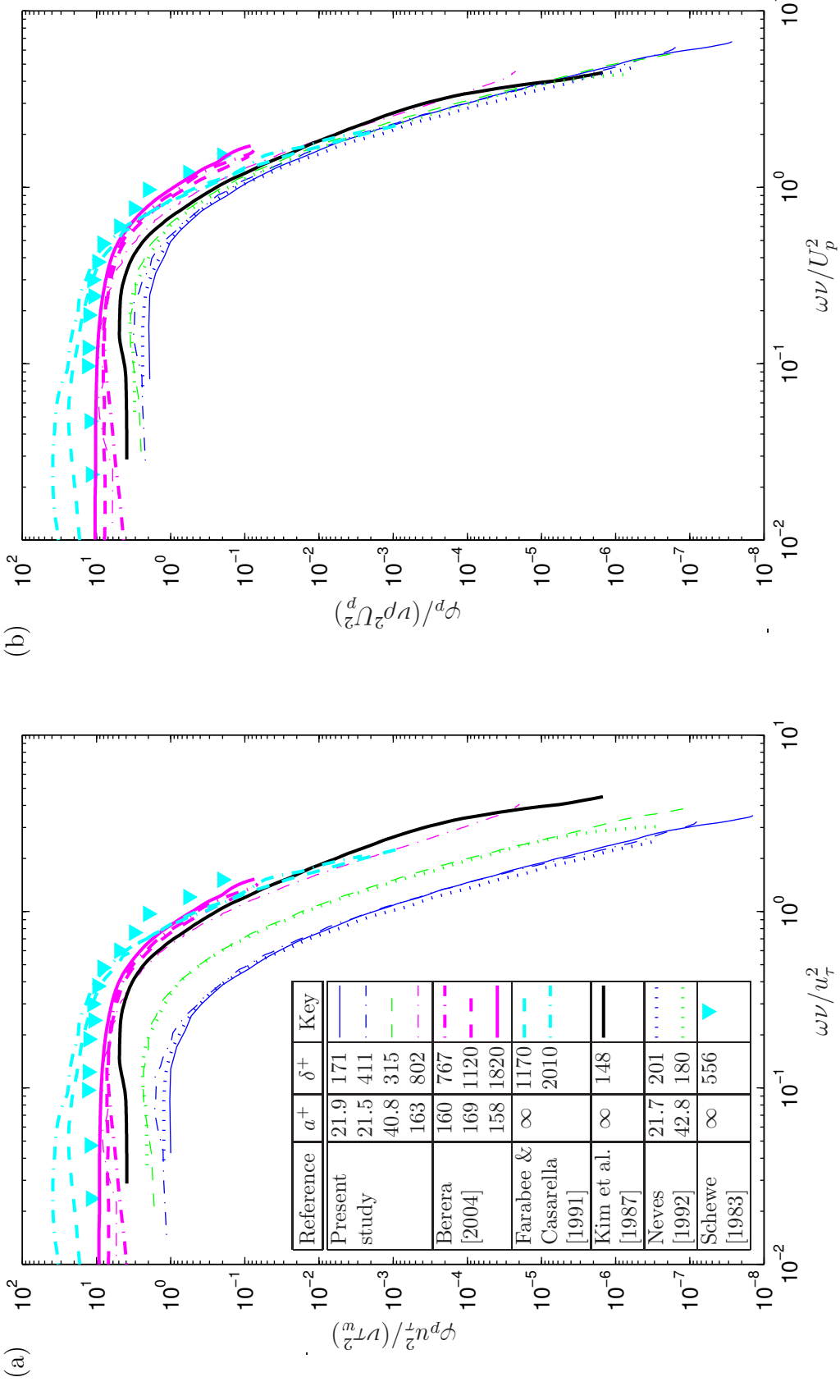

Figure 5.8: Temporal spectra of wall-pressure in high-frequency form: (a) flat-plate scaling; (b) scaling modified for transverse curvature, where $U_p^2 = u_\tau^2/(1 + 20/a^+)$. Line-styles and symbols are defined in the legend.

data are also consistent with the experiments of Schewe [1983] and Berera [2004], although their measurements yield high-frequency spectral levels that are slightly higher than those of the other investigations considered here.

Universal Frequency Range

The flat-plate universal range represents an overlap of the mid-frequency and high-frequency ranges. Such an overlap implies that, in this range, the spectral density is independent of any length- or velocity-scale, which in turn implies that $\varphi_p\omega =$ constant or $\varphi_p \propto \omega^{-1}$. For the present simulations, the character of the variation of the spectral density with increasing frequency — a transition from a constant value to a rapidly falling value — inevitably means that over some part of the frequency range the spectral density will vary inversely with the frequency. The frequency range over which this form of variation occurs is in fact very small, and there is certainly no extended region of overlap similar to that found in high-Reynolds-number measurements on flat plates. For the low Reynolds numbers under consideration, the upper limit of the mid-frequency range and the lower limit of the high-frequency range can therefore be taken as coincident. The upper limit of the low-frequency range can then be defined by $\omega\nu/U_p^2 \leq 0.4$.

The frequency ranges and similarity scaling relations for temporal spectra of axi-symmetric boundary layers are summarised at the end of the chapter.

5.6 Convection Velocity

In experimental investigations of turbulent flow, quantitative measurements are typically obtained using probes at discrete spatial positions in the flow. Temporal variations of flow quantities are therefore readily examined, whereas study of spatial variations requires the comparison of signals from several probes distributed over the region of interest. Taylor's hypothesis allows spatial variations to be estimated from temporal measurements, or vice-versa, through the idea that "frozen" structures are convected with the mean flow at some proportion of the free-stream velocity.

Typical definitions of the convection velocity involve either the two-dimensional space-time correlation or its Fourier transform, the frequency-wave-number spectrum. The convection velocity is related to the location of the maximum, along either axis, of the correlation or spectrum. The resulting velocity is a function of streamwise separation, time delay, wave-number or frequency. Neves [1992] found that the convection velocity is roughly constant over most of the range of each of

the possible independent variables. The magnitude of the convection velocity varies slightly depending on the chosen definition.

The convection velocity U_c may be used to convert the spatial spectrum E_p and streamwise wave-number k_z to an estimated temporal spectrum φ_p^* and frequency ω^* as follows:

$$\begin{aligned} \varphi_p^* &= \frac{E_p}{U_c} \\ \omega^* &= k_z U_c. \end{aligned} \tag{5.17}$$

For present purposes, U_c is considered to be independent of frequency. The value of U_c is determined so that the temporal spectrum φ_p^* estimated from the spatial spectrum E_p is the closest possible match to the temporal spectrum φ_p calculated from time-series data. Specifically, the convection velocity is defined to be the value of U_c that minimises the mean absolute value of $\big(\varphi_p[\omega_i] - \varphi_p^*[\omega_i]\big)$. The mean is computed across the set of discrete frequencies ω_i at which the temporal spectrum φ_p is calculated, excluding those frequencies that lie outside the range of ω^*. The values $\varphi_p^*[\omega_i]$ are interpolated between the discrete frequencies ω_i^* corresponding to the discrete wave-numbers k_{z_i} at which the spatial spectrum E_p is calculated.

The convection velocities and estimated spectra corresponding to the above definitions are shown for a selection of simulated flows in figure 5.9. Also shown are the temporal spectra calculated directly from wall-pressure time-series. The treatment of U_c as independent of frequency appears to be justified by the good agreement between estimated and calculated spectra at all frequencies. For the range of flows considered, U_c/V_∞ varies from 0.608 to 0.839 and U_c/u_τ varies from 11.1 to 13.0. The convection velocities correspond to the mean-flow velocities at wall-normal positions ranging from 18.2 to 23.8 axisymmetric wall units (in the form proposed by Rao [1967]). These positions are close to the inner limit of the logarithmic region of the mean velocity profiles in figure 4.2. Thus, for the flows considered here, it appears that the dominant contribution to the wall-pressure is made by pressure-sources that are located in the buffer region of the boundary layer.

5.7 Root-Mean-Square Wall-Pressure

Calculated and experimental values of the RMS fluctuations of wall-pressure, expressed in the form p'/τ_w, are plotted against δ^+ in figure 5.10. The sources of data are summarised in the legend attached to the figure.

The RMS wall-pressures computed by Moser et al. [1999] are consistently lower than those of Spalart [1988]. Moser et al. used a variant of the plane-channel sim-

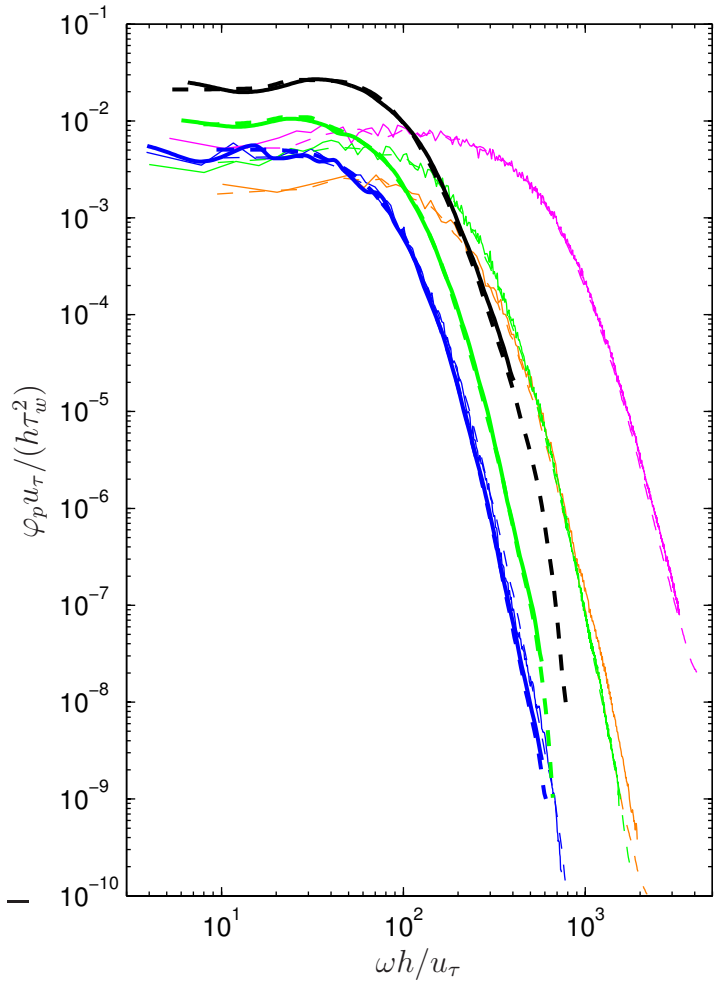

Figure 5.9: Estimated temporal spectra of wall-pressure obtained from spatial spectra using Taylor's hypothesis. Estimated spectra (solid lines) are compared with calculated temporal spectra (dashed lines) for present simulations and reference data. Flow cases and the corresponding line colours are listed in the legend below. Also given for each flow case are the convection velocity U_c and the wall-normal position y_c (in the axisymmetric wall units of Rao [1967]) where the mean-flow velocity equals U_c.

Reference	a^+	δ/a	δ^+	U_c/V_∞	U_c/u_τ	$a^+ \ln[1 + y_c^+/a^+]$	Colour
Present study	21.9	7.82	171	0.815	11.6	19.4	
	21.5	19.1	411	0.768	11.1	18.2	
	40.8	7.74	315	0.726	12.0	19.3	
	163	4.92	802	0.608	12.3	20.3	
Kim et al. [1987]	∞	0	148	0.633	13.0	23.8	
Neves [1992]	21.7	9.23	201	0.705	12.2	21.0	
	42.8	4.20	180	0.839	11.5	18.7	

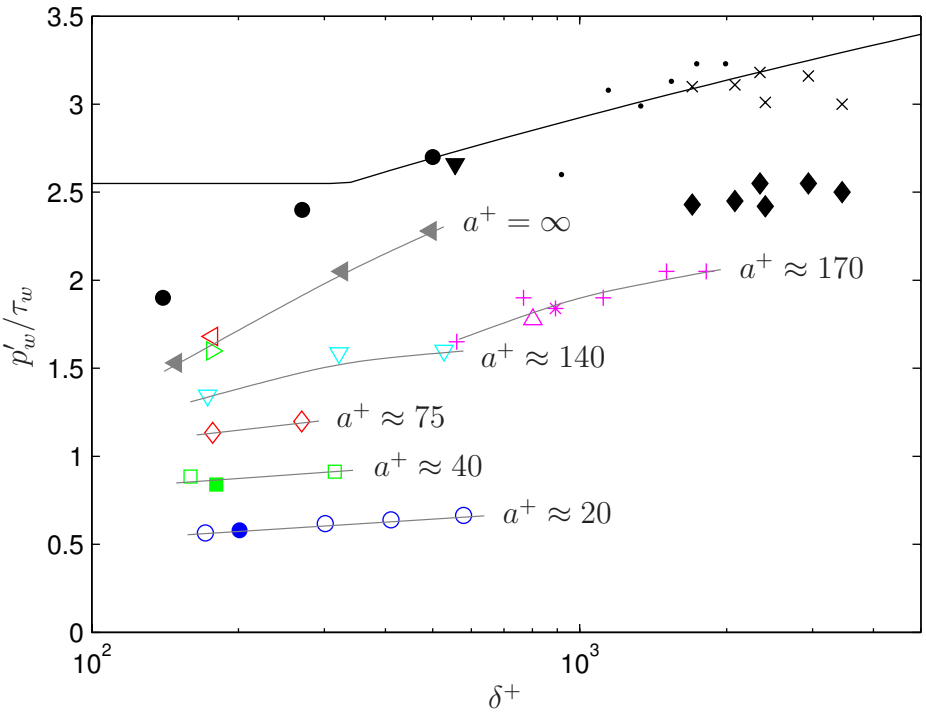

Figure 5.10: RMS wall-pressure fluctuations as a function of δ^+ for present simulations and reference data. Legend:

Reference	Description	a^+	δ/a	δ^+	Symbol
Present study	Cylinder simulation	21.0–21.9	7.82–27.6	171–580	○
		40.8–42.7	3.74–7.74	159–315	□
		74.3–76.0	2.33–3.63	177–270	◇
		131–146	1.18–4.01	173–527	▽
		163	4.92	802	△
		564	0.313	177	▷
		1130	0.157	177	◁
Berera [2004]	Pin-hole sensor	158–175	3.2–11.5	560–1820	+
Bull and Thomas [1976]	Pin-hole sensor	∞	0	1700–3450	×
	Flush sensor				♦
Farabee and Casarella [1991]	Pin-hole sensor	∞	0	1170–2010	·
	Equation 5.18				—
Moser et al. [1999]	Plane-channel simulation	∞	0	149–495	◀
Neves [1992]	Cylinder simulation	21.7	9.23	201	●
		42.8	4.20	180	■
Schewe [1983]	Flush sensor	∞	0	556	▼
Snarski and Lueptow [1995]	Pin-hole sensor	177	5.04	892	✳
Spalart [1988]	Flat plate simulation	∞	0	140–500	●

ulation code of Kim et al. [1987] which, as in the present calculations, effectively imposes a streamwise pressure-gradient on the statistically-steady state. The numerical scheme devised by Spalart accounts for the streamwise development of the mean flow so that the pressure-gradient is eliminated. The difference between these two sets of simulations can therefore be attributed to the presence or otherwise of a streamwise pressure-gradient. Spalart's wall-pressure result at $\delta^+ = 500$ is in good agreement with the flat-plate measurement of Schewe [1983] at $\delta^+ = 556$.

Farabee and Casarella [1991] derive an empirical formula for the RMS wall-pressure in flat-plate flow by integration of measured pressure spectra using the scaling relationship appropriate for each frequency range. The predictions of their formula, which in the present notation is

$$\left(\frac{p'}{\tau_w}\right)^2 = \begin{cases} 6.5 & (\delta^+ \leq 333), \\ 6.5 + 1.86\ln(\delta^+/333) & (\delta^+ > 333), \end{cases} \tag{5.18}$$

are shown as a solid black line in the figure. The formula is consistent with the measurements of Farabee and Casarella, as one would expect, and also with the measurement by Schewe [1983] and, to a lesser extent, with the pin-hole sensor results of Bull and Thomas [1976]. For small δ^+, however, the predictions deviate from the results obtained by Spalart [1988]. The discrepancy would possibly be eliminated by revision of the frequency limits assigned to each region of the wall-pressure spectra.

Bull and Thomas [1976] investigate the effects of pin-holes on wall-pressure measurements. Their measured values of RMS wall-pressure depend strongly on the type of sensors used, be they flush with the surface or mounted behind pin-holes. The values obtained with flush-mounted sensors appear rather low compared with other experimental data, including the measurement by Schewe [1983] which also used a flush sensor. The trend followed by the simulation results of Spalart [1988] also suggests that the flush-sensor results of Bull and Thomas [1976] are too low. It is unlikely that the difference between flush-sensor and pin-hole measurements would be entirely removed by use of smaller sensors, because the smallest sensors used by Bull and Thomas ($d^+ \approx 45$) are only about twice the size of that used by Schewe ($d^+ = 19$). The effect of pin-holes on wall-pressure measurements seems not to have been conclusively established.

The RMS wall-pressures calculated by the present simulations are in good agreement with the simulations of Neves [1992] at $a^+ \approx 21$ and 42. The present simulations for $a^+ \geq 564$ with $\delta^+ = 177$ are consistent with the plane-channel simulation

of Moser et al. [1999] at $\delta^+ = 149$. The present result for $a^+ = 163$ with $\delta/a = 4.9$ ($\delta^+ = 802$) is consistent with the measurements by Berera [2004] and Snarski and Lueptow [1995] for similar a^+ and δ/a.

For cylinder data, the values of p'/τ_w as a function of δ^+ follow separate curves for each value of a^+, as indicated by the grey curves in the figure (5.10). At a given value of δ^+, the RMS wall-pressure increases towards the plane-channel result as a^+ increases (and δ/a decreases); the RMS wall-pressure is substantially reduced when a^+ is small (and δ/a is large). The upward slope of the pressure curves at a given δ^+ appears to be greater for flow with large a^+ (and small δ/a) than for flow with small a^+ (and large δ/a). The slope of a given pressure curve (for flow at a given value of a^+) decreases with increasing δ^+, and therefore with increasing δ/a, as is consistent with the idea that the proportion of the wall-pressure contributed by the outer portion of the boundary layer is reduced as δ/a increases.

The significant changes in RMS wall-pressure caused by transverse curvature of the boundary layer indicate that δ (in the form δ^+) is not the appropriate length-scale to use for the scaling of p'/τ_w when δ/a is non-zero. A possible alternative length-scale is defined by equation 5.14: $L_p = \delta/(1 + 0.4\delta/a)$. The data from figure 5.10 are re-plotted as functions of $L_p^+ = L_p u_\tau/\nu$ in figure 5.11. For cylinder data, the functional form of the relationship between p'/τ_w and $\log[L_p^+]$ appears to be a straight line, which also passes through the plane-channel results of Moser et al. [1999] and the flat-plate measurements of Farabee and Casarella [1991]. The line-of-best-fit to the cylinder data and the above-mentioned planar results is given by $p'/\tau_w = 1.61 \log[L_p^+] - 2.04$, which is shown as a grey line in the figure. The line-of-best-fit has a greater slope than the empirical formula of Farabee and Casarella [1991], which is plotted as a black line in the figure. It is not clear which of the two lines is the more reliable over the range $100 \lesssim L_p^+ \lesssim 3000$, because there is considerable scatter in the available results for planar flow.

The fact that the RMS wall-pressure scales quite well with the length-scale L_p is not without precedent. The same length-scale is used successfully to scale the temporal spectra of wall-pressure in the mid-frequency range. This frequency range contributes a significant proportion of the RMS wall-pressure, which is therefore closely related to the length-scale L_p.

The definition of L_p encapsulates the idea that the fraction of the boundary layer that contributes to the wall-pressure is reduced as δ/a increases. Specifically, $L_p = \delta$ when $\delta/a = 0$, and the fraction L_p/δ decreases monotonically as δ/a increases. For $\delta/a > 2.5$, L_p is less than half of δ. Thus, for the majority of the cylinder flows

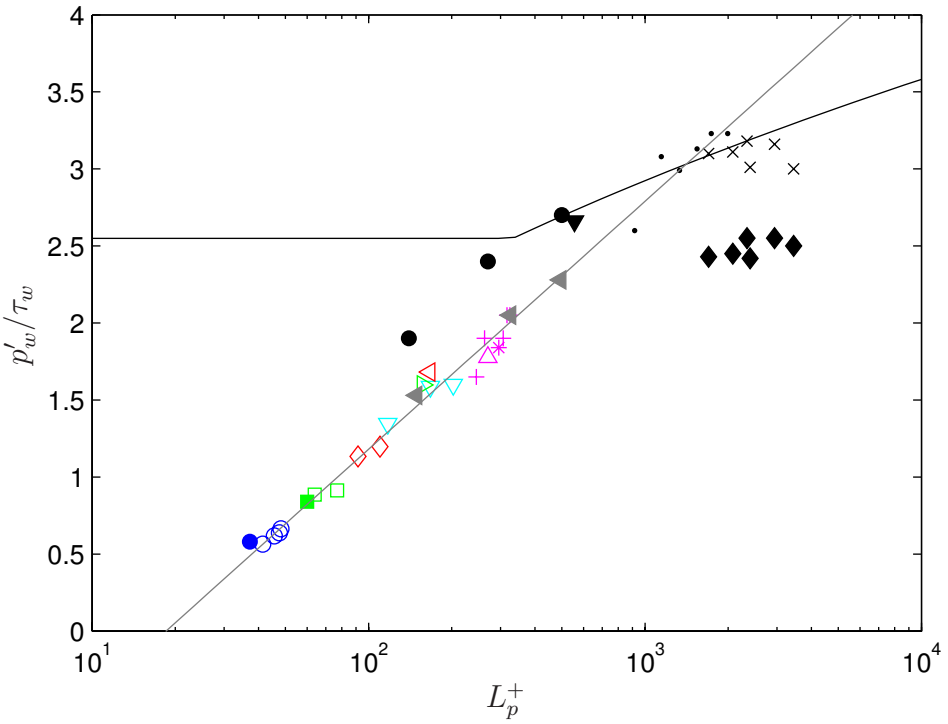

Figure 5.11: RMS wall-pressure fluctuations versus $L_p^+ = \delta^+/(1+0.4\delta/a)$ for present simulations and reference data. —— $p'/\tau_w = 1.61\log[L_p^+] - 2.04$. Other symbols:

Reference	Description	a^+	δ/a	δ^+	Symbol
Present study	Cylinder simulation	21.0–21.9	7.82–27.6	171–580	○
		40.8–42.7	3.74–7.74	159–315	□
		74.3–76.0	2.33–3.63	177–270	◇
		131–146	1.18–4.01	173–527	▽
		163	4.92	802	△
		564	0.313	177	▷
		1130	0.157	177	◁
Berera [2004]	Pin-hole sensor	158–175	3.2–11.5	560–1820	+
Bull and Thomas [1976]	Pin-hole sensor	∞	0	1700–3450	×
	Flush sensor				◆
Farabee and Casarella [1991]	Pin-hole sensor	∞	0	1170–2010	·
	Equation 5.18				——
Moser et al. [1999]	Plane-channel simulation	∞	0	149–495	◀
Neves [1992]	Cylinder simulation	21.7	9.23	201	●
		42.8	4.20	180	■
Schewe [1983]	Flush sensor	∞	0	556	▼
Snarski and Lueptow [1995]	Pin-hole sensor	177	5.04	892	✳
Spalart [1988]	Flat plate simulation	∞	0	140–500	●

considered here, the bulk of the wall-pressure is generated by a small fraction of the boundary layer near the cylinder wall.

For planar flow at moderate to large values of δ^+, it is reasonably well established that the RMS wall-pressure is related to δ^+ by a function of the form $p'/\tau_w = c_1 \log[\delta^+] + c_2$, where c_1 and c_2 are constants. The slope of the function, that is $d(p'/\tau_w)/d\delta^+$, is equal to c_1/δ^+, which decreases as δ^+ increases. A tentative explanation for the decreasing slope is as follows. When δ^+ is increased by a small increment $\Delta\delta^+$, additional pressure-sources are supported near the outer edge of the boundary layer; the intensity of pressure-source fluctuations in the inner boundary layer is little affected. The additional pressure-sources contribute to an increase in the RMS wall-pressure of $\Delta(p'/\tau_w)$. For a given value of $\Delta\delta^+$, the corresponding value of $\Delta(p'/\tau_w)$ decreases as the additional pressure-sources become more distant from the wall. Consequently, the ratio $\Delta(p'/\tau_w)/\Delta\delta^+$ ($\approx d(p'/\tau_w)/d\delta^+$) decreases as δ^+ increases, because the additional pressure-sources are located near $y^+ = \delta^+$.

5.8 Summary and Conclusions

The main findings arising from analysis of the pressure statistics for turbulent boundary layers on cylinders in axial flow are summarised here.

Profiles of RMS pressure, in the form p'/τ_w versus y^+, are strongly dependent, near the wall, on the value of a^+. The profiles are quite similar to plane-channel results when a^+ is large, and they are reduced substantially when a^+ is small. For flows with large values of a^+, the peak value of the RMS pressure profile increases with increasing δ^+; there is no evidence for an upper limit to the near-wall RMS pressure as δ^+ tends to infinity. The RMS pressure profiles plotted as functions of y/h show a strong dependence on b/a (and hence δ/a); the profiles nearly collapse to a common curve outside the buffer region when normalised by $\rho u_{\tau c}^2$ (instead of $\tau_w = \rho u_\tau^2$). Skewness and flatness statistics for the pressure fluctuations are strongly dependent on a^+. As a^+ decreases, the skewness becomes more negative and the flatness more positive, reflecting the trends in the axial component of velocity.

Analysis of the Green's function that corresponds to the Poisson equation for pressure gives insights concerning the proportion of the wall-pressure contributed by different regions or structures within the flow. The form of the Green's function in the present cylindrical geometry suggests that turbulent eddies with large streamwise or spanwise dimensions can be expected to make the dominant contribution to the wall-pressure. Also, for a given pressure-source distribution over the radial interval

$r_s/a = [1, 1 + \delta/a]$, the wall-pressure contributed by the outer part of the boundary layer can be expected to decrease as δ/a is made larger.

The pressure at a given spatial location is generated by the combined influence of infinitesimal pressure-sources that are distributed throughout the boundary layer. The strength of these pressure-sources is a continuous function of spatial position, which can be expressed as a sum of products of spatial derivatives of the instantaneous velocity field. The results of the present simulations have been examined to compare the RMS fluctuation intensity of the different pressure-source terms. Near the cylinder wall, the dominant term is found to be $(2/r)(\partial u_\theta/\partial r)(\partial u_r/\partial\theta - u_\theta)$, in accordance with the results of Neves [1992]. Away from the wall, the dominant terms are $(2/r)(\partial u_\theta/\partial r)(\partial u_r/\partial\theta - u_\theta)$, $2(\partial u_z/\partial r)(\partial u_r/\partial z)$ and $(2/r)(\partial u_z/\partial\theta)(\partial u_\theta/\partial z)$, which have roughly equal fluctuation intensities.

The RMS fluctuations of the total pressure-source field, with all terms taken into account, are at a maximum in the vicinity of $y^+ = 20$ for all of the present simulations. The effects of transverse surface curvature on the pressure-source field appear qualitatively similar to those affecting the underlying velocity field. For axisymmetric flow at a given value of δ^+, the intensity of the pressure-source fluctuations is similar to that for planar flow when δ/a is small and a^+ is large; the fluctuation intensity decreases throughout the boundary layer when a^+ becomes small. For flows with large values of a^+, the pressure-source fluctuation intensity at a given position y^+ increases as δ^+ increases. However, the intensity is likely to approach an upper limit at large values of δ^+, as appears to be the case for the velocity statistics. The combined effects of Reynolds number (δ^+) and curvature ($a^+, \delta/a$) are sufficiently complex that a satisfactory scaling relation for the intensity of the pressure-source fluctuations has yet to be identified.

Temporal wall-pressure spectra for flow over cylinders exhibit characteristic frequency ranges that are counterparts of the frequency ranges identified for flow over flat plates. The cylinder ranges show considerably more complicated similarity scaling relations than the flat-plate ranges, as a result of the effects of curvature on the flow. Empirical forms for the spectral scaling in the mid-frequency and high-frequency ranges have been determined from the present simulations. These ranges and forms are listed in table 5.2. For the low Reynolds numbers (δ^+) under consideration, there is no extended universal range similar to that found in measurements at high Reynolds numbers; the upper limit of the mid-frequency range and the lower limit of the high-frequency range are therefore taken as coincident. The scaling relations are consistent with available experimental data for cylinders in axial flow,

Frequency Range	Frequency Limits	Spectral Form
Mid-frequency	$5 \leq \omega L_p/u_\tau,\ \omega\nu/U_p^2 \leq 0.4$	$\varphi_p u_\tau/(L_p\tau_w^2) = f_2\big[\omega L_p/u_\tau\big]$
High-frequency	$\omega\nu/U_p^2 \geq 0.4$	$\varphi_p/(\nu\rho^2 U_p^2) = f_4\big[\omega\nu/U_p^2\big]$

Table 5.2: Frequency ranges and spectral forms for wall-pressure in transversely curved boundary layers. f_2 and f_4 represent functions. The curvature-adjusted length- and velocity-scales are $L_p = \delta/(1+0.4\delta/a)$ and $U_p = u_\tau/\sqrt{1+20/a^+}$.

and asymptotically approach the flat-plate relations as the radius of the cylinder increases.

The scaling relations for the temporal spectra of wall-pressure on cylinders are based on the corresponding relations for flat-plate flow. In the mid-frequency range, the flat-plate length-scale δ is replaced by $L_p = \delta/(1+0.4\delta/a)$. In the high-frequency range, the flat-plate velocity-scale u_τ is replaced by $U_p = u_\tau/\sqrt{1+20/a^+}$ and the stress-scale $\tau_w = \rho u_\tau^2$ is replaced by ρU_p^2. The length-scale L_p encapsulates the idea that the effective thickness of the boundary layer is reduced by curvature, because the outer portion of the boundary layer contributes less to the wall-pressure as δ/a increases. In the planar limit of $\delta/a = 0$, L_p is equal to δ, and as δ/a increases, the ratio L_p/δ decreases. For $\delta/a \geq 2.5$, L_p is biased towards the cylinder radius ($L_p \leq \delta/2$). The velocity-scale U_p is approximately equal to $u_{\tau c}$ (equation 4.22) evaluated at $y^+ = 20$, which is the approximate location of the maximum fluctuation intensity of the pressure-source field (figure 5.5a). Pressure-sources near this position are presumed to make the dominant contribution to the wall-pressure in the high-frequency range of the spectrum. For planar flow ($a^+ = \infty$), U_p is equal to u_τ, and as a^+ decreases, the ratio U_p/u_τ decreases. The value of U_p is greater than 90% of u_τ for all flows except those with $a^+ < 85$.

Approximate temporal spectra may be derived from spatial spectra, and vice-versa, by use of the idea that "frozen" flow fields are convected downstream with a velocity U_c. In the present investigation, values of U_c have been determined for a number of simulated flows such that the temporal spectra estimated from spatial spectra are the closest possible match to the temporal spectra calculated from time-series data. The estimated and calculated temporal spectra are in good agreement at all frequencies in all of the flows considered, despite the treatment of U_c as independent of frequency. The values of U_c obtained vary from $0.608/V_\infty$ ($11.1u_\tau$) to $0.839/V_\infty$ ($13.0u_\tau$). These convection velocities suggest that in flows with small δ^+ or large δ/a, the dominant contribution to the wall-pressure is made by pressure-sources in the buffer region of the boundary layer.

The RMS wall-pressure p' on cylinders, when normalised by the wall-shear-stress τ_w, is strongly dependent on the length-scale L_p. The empirical formula $p'/\tau_w = 1.61 \log[L_p^+] - 2.04$ is a good fit to the available cylinder data and also to the plane-channel results of Moser et al. [1999] and the flat-plate measurements of Farabee and Casarella [1991]. The present formula differs from that obtained by Farabee and Casarella [1991] based on planar results, but it is not clear which of the two formulae is the more reliable (over the range $100 \lesssim L_p^+ \lesssim 3000$) due to the considerable scatter in the available data. The scatter is probably caused by systematic differences between experiments (and calculations), including differences in streamwise pressure-gradients, sensor resolution and sensor mounting techniques (pin-hole versus flush). Additional measurements and calculations to isolate or eliminate the effects of these systematic differences would be a worthy subject for future work.